日本原子力研究開発機構

JAEA-Tokai Tandem Annual Report 2013

April 1, 2013 – March 31, 2014

Department of Research Reactor and Tandem Accelerator

Nuclear Science Research Institute
Sector of Nuclear Science Research

JAEA-Review

日本原子力研究開発機構

JAEA-Tokai Tandem Annual Report 2013
April 1, 2013 – March 31, 2014

Department of Research Reactor and Tandem Accelerator

Nuclear Science Research Institute

Sector of Nuclear Science Research

Japan Atomic Energy Agency

Tokai-mura, Naka-gun, Ibaraki-ken

The Japan Atomic Energy Agency (JAEA)-Tokai tandem accelerator complex has been used in various research fields such as nuclear science and material science by researchers not only of JAEA but also from universities, research institutes and industrial companies. This annual report covers developments of accelerators and research activities carried out using the tandem accelerator and superconducting booster from April 1, 2013 to March 31, 2014. Thirty-one summary reports were categorized into seven research/development fields:
 (1) accelerator operation
 (2) nuclear structure
 (3) nuclear reaction
 (4) nuclear chemistry
 (5) nuclear theory
 (6) atomic physics and solid state physics
 (7) radiation effects in materials.
This report also lists publications, meetings, personnel, committee members, cooperative researches and common use programs.

Editors: Akihiko OSA, Katsuhisa NISHIO, Kazuaki TSUKADA, Norito ISHIKAWA,
Yosuke TOH, Hiroyuki KOURA, Nariaki OHKUBO and Makoto MATSUDA

原子力機構東海タンデム加速器 2013 年度年次報告

日本原子力研究開発機構
原子力科学研究部門
原子力科学研究所
研究炉加速器管理部

　日本原子力研究開発機構（原子力機構）東海タンデム加速器施設は、原子核科学や物質科学などの様々な分野において、原子力機構を始めとして、大学や公立研究機関、民間企業に利用されている。本年次報告書は、タンデム加速器およびブースター加速器を利用し、2013 年 4 月 1 日から 2014 年 3 月 31 日までの期間に実施された研究活動の英文要約をまとめたものである。総数 31 件の要約を下記の 7 部門に分類した。
（1）加速器の運転状況
（2）原子核構造
（3）原子核反応
（4）核化学
（5）原子核理論
（6）原子物理及び固体物理
（7）材料の照射効果
また、発表論文と会議での口頭発表、タンデム加速器に関与した職員、タンデム加速器専門部会委員、大学等との共同研究課題、及び施設共用課題のリストを掲載した。

Foreword

This report covers research and development activities with the tandem accelerator and its superconducting booster at JAEA Tokai, for the period of FY 2013 (April 1, 2013 to March 31, 2014). The tandem accelerator was operated over a total of 152 days and delivered 19 different ion beams to experiments in the fields of nuclear physics, nuclear chemistry, atomic physics, solid state physics and radiation effects in materials. Thirty-three research programs were carried out in collaboration with a total of about 100 researchers from universities and research institutes.

The following are the highlights in FY 2013:

In the field of nuclear structure: Coulomb excitation experiment of ^{130}Xe was performed to deduce B(E2) values and quadrupole moments. The first excited 2+ state in ^{252}Fm was determined by the α decay of ^{256}No. It suggests that ^{252}Fm has the character of the double deformed-shell closure. The fluorescence from the W atoms was observed by the on-line gas cell laser spectroscopy.

In the field of nuclear reactions: Multi-nucleon transfer induced fission was used to measure the fission fragment mass distributions and their dependence on the excitation energy of compound nucleus. In the reaction of ^{18}O + ^{232}Th, it was shown that data for more than 14 actinide nuclei were obtained in a single measurement, including new data of ^{234}Th and $^{234, 235, 236}$Pa. Also, development for the measurement of prompt neutrons has started.

In the field of nuclear chemistry: Medical use radioisotope ^{211}At which is a promising α-emitter for cancer therapy were produced using a new ^{211}Rn-^{211}At generator technique, and the radiolabeling reactions of astatinated phenylalanine were also investigated. The first Compton camera imaging picture with gamma rays from ^{95m}Tc isotope which is produced via the ^{nat}Mo(p, n)^{95m}Tc reaction were successfully reported. Fundamental researches on the chemistry of heavy- and trans-actinides were also performed, and the further progress will be expected and give us to open up a new research field related to the heavy element chemistry.

In the field of nuclear theory: Shell-model calculations for neutron-rich calcium and scandium isotopes are carried out for qualifying the strength of the N=34 shell gap, and a reasonable shell gap is obtained with the GCPF1Br interaction. Although this is a modest shell gap being close to the N=32 gap, it is much larger than the sub-shell gaps of the nickel region that are less than 1 MeV. Furthermore, a systematic fission barrier calculation in the superheavy nuclear mass region is carried out with the KTUY nuclear mass-model calculation, and we find an existence of 'peninsula' of stability of nuclei along 228 of the number of neutron with between 114 and 126 of the number of protons.

In the field of atomic physics and solid-state physics: A new method to improve sensitivity to lithium diffusion coefficients is proposed. Since lithium diffusion coefficients could not be measured by the previous method below 200℃, in the present study measurement of the lithium diffusion coefficients in Li_2O-V_2O_5-SiO_2 (LVSO) thin film was performed at low temperature (e.g. 100℃). The detection limit for the diffusion coefficients was improved by about two orders of magnitude in comparison to that achieved with the previous method.

In the field of radiation effects in materials: CeO_2 was irradiated with Au ions in the energy range of 200-340 MeV at oblique incidence. Observation of as-irradiated samples by transmission electron microscope (TEM) has shown that many of the hillocks are found to be spherical. It is the first time that the crystal structure of the hillocks created for CeO_2 is revealed. It is found that the crystal orientation and structure of the hillocks coincide with those of the matrix of CeO_2.

Yoji MURAYAMA, Director, Department of Research Reactor and Tandem Accelerator

Contents

目　　　次

CHAPTER 1

Accelerator Operation

1.1   Operation and usage of tandem accelerator and booster

This is a blank page.

1.1　Operation and usage of tandem accelerator and booster

A. Osa[1], S. Hanashima[1], S. Abe[1], T. Ishii[1], N. Ishizaki[1], H. Tayama[1], M. Matsuda[1],
T. Nakanoya[1], H. Kabumoto[1], M. Nakamura[1], K. Kutsukake[1], Y. Otokawa[1] and T. Asozu[1]

The tandem accelerator was operated for experiments from April 1, 2013 to May 26, from June 17 to July 15, from October 7 to January 15, 2014, and from March 3 to March 31. The experiments at May 27 and 28, 2013 were terminated by the accident of J-PARC Hadron Experimental Facility. The total operation time of the tandem accelerator for FY2013 (from April 1, 2013 to March 31, 2014) was 152 days and 19 different beams were delivered for experiments. The experimental proposal and the usage of the beam times for FY2013 are summarized in Table 1 and Table 2, respectively.

Table 1. Experimental proposals.

Research proposals accepted by the program advisory committee:	
In-house staff proposals	2
Collaboration proposals	7
Shared use proposal	9
Number of experiments proposed	33
Total number of scientists participating in research	
from outside	100
in-house	50
Number of institutions presented	34

Table 2. Usage of beam-times in different research fields.

Research field	Beam time (days)	(%)
Nuclear physics	47	30.9
Nuclear chemistry	40	26.3
Atomic and materials sciences	55	36.2
Accelerator development	10	6.6
total	152	100

Distributions of the terminal voltages and ion species for experiments are shown in Fig.1 and Fig.2, respectively. Half of the beams were extracted from three negative ion sources, SNICS-2. The proton beam and multiply charged ion beams of carbon, nitrogen, oxygen and rare gases were ionized and extracted from in-terminal ECR ion source. In addition, we succeeded at extracting of Nickel beam by using nickerocene seed.

---

[1]　Japan Atomic Energy Agency (JAEA)
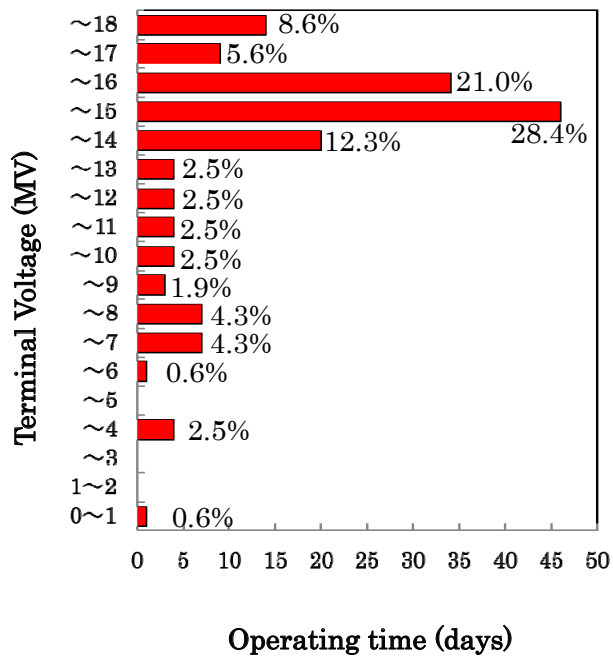
Fig.1 Distribution of terminal voltages.
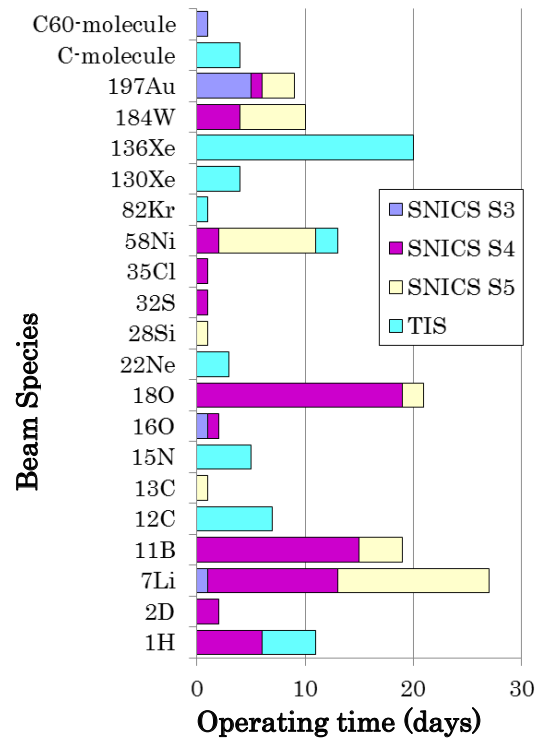
Fig.2 Distribution of beam species accelerated for experiments.

CHAPTER 2

Nuclear Structure

This is a blank page.

2.1 Coulomb excitation experiment of ^{130}Xe

M. Koizumi[1], Y. Toh[1], A. Kimura[1], K. Furutaka[1], H. Harada[1], F. Kitatani[1], S. Nakamura[1]
and M. Sugawara[2]

Stable Xe isotopes gradually change in their properties from a γ-unstable character (A ~ 124) to a vibrational one (A = 134) [1]. This change is considered as a shape phase transition from O(6) to U(5), in terms of the dynamic symmetry of the IBM. Theoretical calculations suggested that the E(5) critical point of the shape phase transition could appear at around A = 130 in Xe isotopes [2,3]. Information on electromagnetic properties of those nuclei, such as B(E2) values and quadrupole moments, is required to understand this change of nuclear properties. As for ^{130}Xe, which is considered to be a γ-unstable nuclei, no B(E2) of the ground and 2_2^+ band has been measured except for B(E2: $2_1^+ \to 0_1^+$). Quadrupole moments of low-lying states of ^{130}Xe have not been measured yet.

Coulomb excitation is a useful method for measuring B(E2)s and quadrupole moments in low-lying ground states of nuclei [4,5]. Our systematic study of stable nuclei with A ~ 70 revealed nuclear properties and their changes [6-13]. To extend our systematic study to another mass region, we have started Coulomb excitation experiments of $^{126-136}$Xe isotopes.

To measure quadrupole moments of ^{130}Xe, we applied a technique of inverse kinematics. The energy of ^{130}Xe beam was 370 MeV, and the beam current was approximately 0.3 pnA. Carbon foil target with a thickness of 514 mg/cm^2 was used. The beam energy is below the Coulomb barrier. The experimental apparatus consisted of a γ-ray detector array, GEMINI-II [14,15], and a position sensitive particle detector array, LUNA [16]. The scattering angles of the recoiled carbon particles were measured by LUNA, while those of the incident particles were small enough not to hit the particle detectors. Totally, 2.3×10^7 particle-γ coincidence events were collected.

Data of recoil angles were used for Doppler-shift correction of observed γ-ray energies. Figure 1 shows a Doppler-corrected γ-ray spectrum. ^{130}Xe was excited up to the 4_1^+ state. De-excitation γ rays of $2_1^+ \to 0_1^+$ (536.1 keV), $2_2^+ \to 2_1^+$ (586.0 keV), and $4_1^+ \to 2_1^+$ (668.5 keV) transitions were observed. The Coulomb excitation probabilities change with the scattering angle. Analysis of the observed γ–ray yields for each scattering angle is in progress with a χ^2 minimum search code, GOSIA, to deduce the matrix elements of the relevant electromagnetic transitions.

---

[1] Japan Atomic Energy Agency (JAEA)
[2] Chiba Institute of Technology
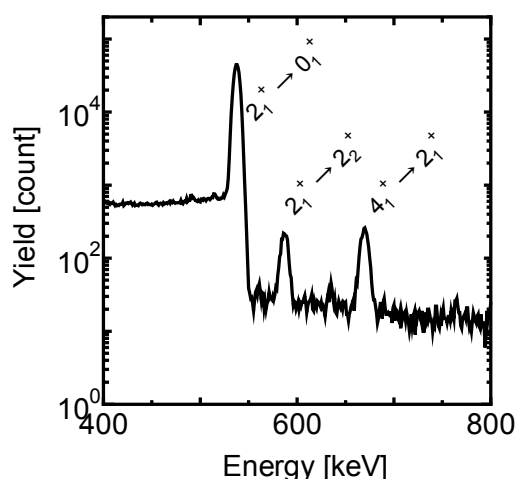
Fig. 1   A Doppler-corrected spectrum obtained with a Ge detector. Three de-excitation transitions were observed.

References

[1] R.F. Casten and P.V. Brentano, Phys. Lett., 152 (1985) 22.

[2] D.L. Zhang and Y.X. Liu, Chin. Phys. Lett., 20 (2003) 1028-1030.

[3] R. Fossin, Dennis Bonatsos and G.A. Lalazissis, Phys. Rev. C, 73 (2006) 044310.

[4] K. Alder and A. Winther, Coulomb Excitation (Academic, New York, 1966).

[5] K. Alder and A. Winther, Electromagnetic Excitation (North Holland, Amsterdam, 1975).

[6] Y. Toh et al., J. Phys. G, 27 (2001) 1475-1480.

[7] Y. Toh et al., Eur. Phys. J. A, 9 (2000) 353-356.

[8] A. Osa et al., Phys. Lett. B, 546 (2002) 48-54.

[9] M. Zielinska et al., Nucl. Phys. A, 712 (2002) 3-13.

[10] M. Koizumi et al., Eur. Phys. J. A, 18 (2003) 87-92.

[11] M. Sugawara et al., Eur. Phys. J. A, 16 (2003) 409-414.

[12] M. Koizumi et al., Nucl. Phys. A, 736 (2003) 46-58.

[13] T. Hayakawa et al., Phys. Rev. C, 67 (2003) 064310.

[14] K. Furuno et al., Nucl. Instrum. Methods Phys. Res. A, 421 (1999) 211; M. Oshima et al., J. Radioanal. Nucl. Chem., 278 (2008) 257-262.

[15] M.Oshima et al., J. Radioanal. Nucl. Chem., 278 (2008) 257-262.

[16] Y. Toh et al., Rev. Sci. Inst., 73 (2002) 47-50.

2.2 Measurement of the first excited 2^+ state in ^{252}Fm

M. Asai[1], K. Tsukada[1], Y. Kasamatsu[2], Y. Ishii[1], A. Toyoshima[1], T. K. Sato[1], Y. Nagame[1],
I. Nishinaka[1], H. Haba[3] and T. Ishii[1]

Energy of the first excited 2^+ state $E(2^+)$ in even-even nuclei is a good probe to explore nuclear shell structure and deformation in the frontier of nuclear chart. In the heaviest frontier of the nuclear chart, experimental data of $E(2^+)$ are very limited because of difficulties in measuring excited states in such nuclei; the heaviest nucleus whose $E(2^+)$ has been determined experimentally is ^{256}Rf ($Z = 104$) [1]. For No ($Z = 102$) and Fm ($Z = 100$) isotopes, $E(2^+)$s have been measured only in ^{252,254}No and ^{250,254,256}Fm. Figure 1 shows experimental $E(2^+)$s of even-even actinide nuclei reported previously [1,2]. The $E(2^+)$s rapidly decrease with increasing neutron number from the $N = 126$ closed shell to $N = 142$, and attains the minima at between $N = 142$ and 152. Then, it seems to start rising from $N = 152$. The inverse of $E(2^+)$ is proportional to the moment of inertia, which correlates to the degree of nuclear deformation. Nearly constant and low $E(2^+)$s of 40–50 keV between $N = 142$ and 152 indicate that the deformations are well developed in these nuclei. In addition, the moments of inertia also correlate to the pairing energy gap. Around this actinide region, it is well known that the large neutron deformed shell gap exists at $N = 152$. At the deformed shell gap, the pairing energy gap becomes small, which makes the moment of inertia large and makes $E(2^+)$ low [3]. This effect is seen in Cm isotopes [4], but is not clear in Cf, Fm, and No isotopes. In No isotopes, $E(2^+)$ significantly drops from $N = 150$ to $N = 152$, but there is no experimental data in $N >$ 152. In Fm isotopes, experimental data exist at $N = 150$, 154, and 156, but not at $N = 152$. $E(2^+)$ should also depend on the existence of the proton deformed shell gap. The macroscopic-microscopic model calculations predict that the large proton deformed shell gap exists at $Z = 100$ [5,6]. Thus, it is of great interest to measure the $E(2^+)$ in ^{252}Fm, which is expected to show the character of the double deformed-shell closure.

Excited states in ^{256}Rf, ^{252,254}No, ^{250}Fm have been observed through in-beam γ-ray spectroscopy with a recoil-decay tagging technique [1]. These nuclei were produced in cold fusion reactions using a Pb or Hg target and a ^{48}Ca or ^{50}Ti projectile. Excited states in ^{254,256}Fm have been observed through the β⁻ decay of ^{254,256}Es. However, these techniques cannot be applied to ^{252}Fm, because ordinary cold fusion
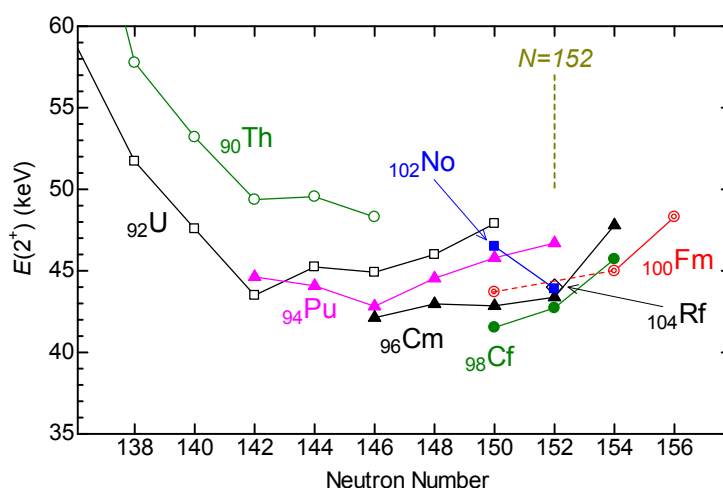
Fig. 1 Energy of the first excited 2^+ states $E(2^+)$ in even-even actinide nuclei reported previously [1,2].

reactions with stable target and projectile combinations cannot produce ^{252}Fm, and ^{252}Es has only 0.01% β^- decay branch. On the other hand, the α decay of ^{256}No can populate excited states in ^{252}Fm. Although the α decay of such an even-even nucleus directly feeds the ground state of its daughter nucleus with high intensity, a small fraction of α transitions should feed the first excited 2^+ state. By measuring the α-energy difference between the transitions to the ground state and to the first excited 2^+ state precisely, we can determine the $E(2^+)$ of ^{252}Fm. The α decay of ^{256}No was reported previously [7], where the $E(2^+)$ of ^{252}Fm was determined to be 47 ± 5 keV. However, the ± 5 keV uncertainty is too large to discuss the systematics of $E(2^+)$ in this region. In the present experiment, we have determined the $E(2^+)$ of ^{252}Fm more precisely through high-resolution α fine-structure spectroscopy.

The nucleus ^{256}No was produced in the ^{248}Cm(^{12}C,4n)^{256}No reaction. The beam energy was 77 MeV on target. Reaction products recoiling out of the target were thermalized in He gas, and transported with a He/KCl aerosol jet through a 25-m long capillary to a rotating-wheel α detection system [8]. The transported products were deposited on a thin foil on the rotating wheel, which periodically moves the deposited sources to two consecutive detector stations each of which was equipped with a Si detector placed at the source-to-detector distance equivalent to the α-detection efficiency of 12%. Figure 2 shows a measured α-energy spectrum. The α transitions to the ground state and to the first excited 2^+ state were clearly observed with an α-energy resolution of 11 keV (FWHM), from which we have derived the

α-energy difference of 41.5 ± 1.3 keV. Taking account of the recoil energy correction, we have determined the $E(2^+)$ of ^{252}Fm to be 42.1 ± 1.3 keV. This result revealed that the $E(2^+)$ of ^{252}Fm is lower than those of other $N = 152$ isotones (^{250}Cf, ^{254}No, and ^{256}Rf) as well as other Fm isotopes, indicating the character of the double deformed-shell closure.
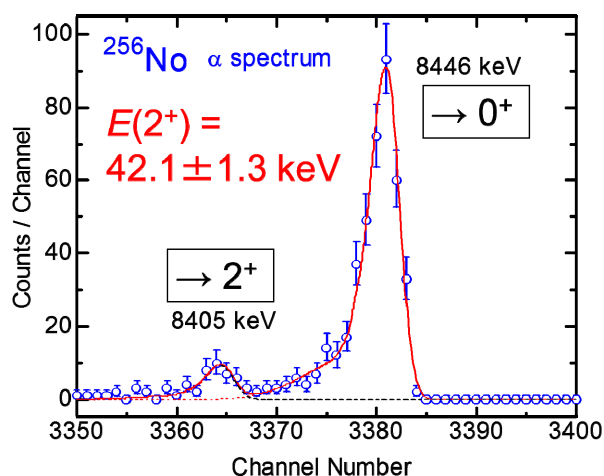
Fig. 2 α-energy spectrum of ^{256}No observed in the present work.

References

[1] P. T. Greenlees, J. Rubert, J. Piot, B. J. P. Gall et al., Phys. Rev. Lett., 109 (2012) 012501.

[2] T. Ishii, H. Makii, M. Asai, H. Koura et al., Phys. Rev. C, 76 (2007) 011303(R).

[3] A. Sobiczewski, I. Muntain, and Z. Patyk, Phys. Rev. C, 63 (2001) 034306.

[4] T. Ishii et al., J. Phys. Soc. Jpn., 75 (2006) 043201.

[5] Z. Patyk and A. Sobiczewski, Nucl. Phys., A533 (1991) 132.

[6] P. Möller, J. R. Nix, and K.-L. Kratz, At. Data Nucl. Data Tables, 66 (1997) 131.

[7] D. C. Hoffman et al., Phys. Rev. C, 41 (1990) 631.

[8] M. Asai et al., Phys. Rev. C, 83 (2011) 014315.

2.3   Development of an on-line gas cell for laser spectroscopy of refractory elements

H. Iimura[1], F. Kitatani[1], M. Koizumi[1] and M. Miyabe[1]

Laser spectroscopy is widely used for precise measurements of the isotope shits in atomic spectra. From these isotope shits, changes of the nuclear charge radii between isotopes can be deduced. For some elements the isotope shifts have been measured not only for stable isotopes but also for unstable ones. However, there has been no measurement for unstable isotopes of W, Re and Os, because these elements are so refractory that they are difficult to be atomized for precise laser spectroscopy. One of the solutions to overcome this difficulty is to catch the reaction product atoms in gas for successive laser spectroscopy. In order to do laser spectroscopy of unstable isotopes of these elements, we have been developing an on-line gas cell, which is similar to the one in SUNY [1]. In this report, present status of the development is given.

The schematic diagram of the on-line gas cell is shown in Fig. 1. The gas cell has a cylindrical shape with 253 mm in diameter and 216 mm in height. The Ni foil of 2.5 μm in thickness separates the vacuum of the gas cell from that of the accelerator beam line. The reaction products being recoiled out from the target are neutralized and thermalized in rare gas, where they stay for about a second before diffusing to the wall of the gas cell and sticking there. While the reaction products stay in the gas, they are irradiated by laser beam from a tunable ring dye laser pumped by a CW solid-state laser. An optics system consisting of a mirror and two lenses was used to collect the laser-induced fluorescence on to the photocathode of a photomultiplier tube. Signal from the photomultiplier tube was counted during the laser frequency scanning. Because the laser system is located at the same room as the on-line gas cell, it cannot be accessible while the accelerator beam is on. Thus, the laser was controlled from other room via Ethernet.
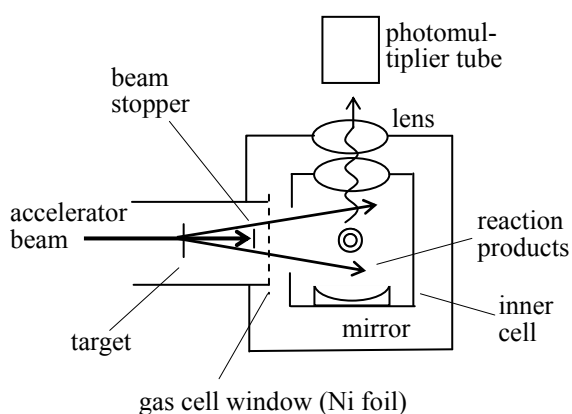
Fig.1 Schematic diagram of the on-line gas cell. Laser beam penetrates the position shown by a double circle.
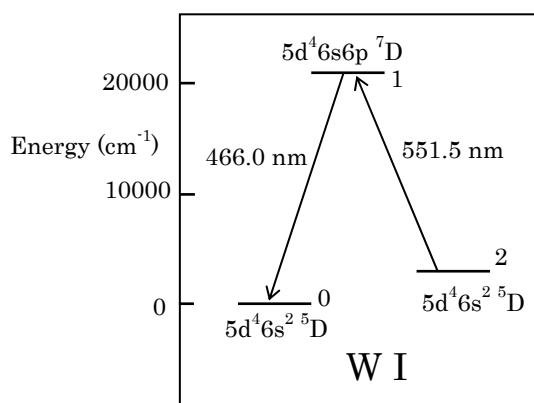
Fig.2 Partial energy levels of W atom

[1] Japan Atomic Energy Agency (JAEA)

In a test experiment the ion beam of stable ^{184}W of about 1 pnA was injected into the gas cell directly without setting a target and a beam stopper. In order to simulate the unstable W isotopes being produced by the ^{16}O(^{A}Dy,xn) reaction, the energy of the ^{184}W ion beam was set at 100 MeV, which, after the Ni foil, becomes about the same energy as the recoiled unstable W isotopes. The gas cell was filled with high purity argon gas with the pressure of 19 hPa, in which the range of W ion is estimated to be the distance between the Ni foil window and the center of the gas cell. As the ion beam is injected into the gas cell, the collisions between the ions and the gas atoms generate strong light, causing large background in observing the laser-induced fluorescence. In order to reduce this background, the DC ion beam from the tandem accelerator was chopped by using a deflector set upstream to the gas cell. The beam turned on and off with repetition rate of 10 Hz, and the signal from the detector was counted in the period when the beam is off. By using the chopped beam the background was reduced to about 1/50 compared to the DC beam.

We tried to observe the laser-induced fluorescence by using the transitions shown in Fig. 2. The W atoms were excited from the metastable state at 3325 cm^{-1} to a higher state by the laser of the wavelength of 551.5 nm, and the fluorescence from this upper state to the ground state with the wavelength of 466.0 nm was observed. A stack of optical filters was used to reduce the background from the scatter of the laser. Owing to these filters and the chopped ion beam, the background count became endurable level of about 4000 counts/sec. However, an apparent resonance peak of the fluorescence has yet been observed. One of the possible reasons is that there is not enough population at the metastable state. Thus, we are now preparing to excite the W atom from its ground state for which large population is expected. Because it is not easy to generate the 466.0-nm laser beam with the ring dye laser, we have set up an external cavity diode laser and recently achieved this wavelength. We are planning to confirm the resonance peak of fluorescence in stable W isotopes by using this laser.

Reference
[1] A. Berger et al., Nucl. Instrum. Methods Phys. Res., A311 (1992) 224-329.

CHAPTER 3

Nuclear Reaction

This is a blank page.

3.1   Development of the JAEA Recoil Mass Separator for the study of proton-rich nuclei around [100]Sn

K. Nishio[1], R. Grzywacz[2,3], K. Rykaczewski[3], A. Andreyev[4], F.P. Heßerger[5], C. Barton[5], M. Bentley[5], N. Brewer[3], C.J. Gross[3], K. Hirose[1], H. Ikezoe[1], D. Jenkins[4], B. Kindler[5], K. Kolos[3], B. Lommel[5], H. Makii[1], I. Nishinaka[1], R. Orlandi[1], R. Léguillon[1], S. Go[2], J. Smallcombe[1], V. Truesdale[4] and R. Wadsworth[4]

The strong interest in the structure of nuclei located in the close vicinity of the nucleus [100]Sn is due to the fact that this nucleus is the heaviest possible doubly-magic nucleus with equal neutron and proton number (N=Z=50). The unique property of the N=Z nuclei is that protons and neutrons occupy the same shell-model orbitals. This fact may reveal a presence of new type of pairing in nuclei – the proton-neutron (p-n) pairing, which could be different from the well-known pairing between like nucleons (n-n and p-p). Recent experiments on nuclei near [100]Sn at the facilities around the world resulted in a very impressive set of publications in journals like Nature and Phys. Rev. Letters. The results provided first glimpses of new phenomena occurring due to pairing effects in nuclear matter. One of them, postulated already in 1965, is the possible existence of the so-called superallowed α decays [1]. In this case, it was expected that the preformation probability of α particle in a parent nucleus should be strongly enhanced due to additional correlations between protons and neutrons occupying the same orbitals. Resulting enhanced α-probability was indeed observed in [100]Sn region in the recent study of [109]Xe→[105]Te→[101]Sn decay chain by the international group [2, 3] working at Oak Ridge National Laboratory. Other recent studies of excited states of lighter mass [92]Pd (Z=N=46) provided a compelling signature of the n-p paired phase below [100]Sn [4]. Superallowed spin-flip Gamow-Teller β decay expected to occur in [100]Sn [5], due to the enhanced probability of the proton-to-neutron conversion, was observed [6] and found to be the fastest β decay seen so far. Proton and α decay studies near [100]Sn were also investigated in the context of astrophysical nucleosynthesis within rapid proton capture process (rp-process) [7]. The particular topography of nuclear binding energies and resulting decay modes for nuclei above [100]Sn could lead to the rp-process termination cycle [8,9].

In view of the importance of proton-rich A~100 nuclei, we started a program of nuclear spectroscopy studies in this region of the Chart of Nuclei by using the JAEA-Recoil Mass Separator. A variety of nuclei and phenomena can be studied by using heavy-ion induced reactions at the JAEA tandem accelerator. In a test experiment using nearly symmetric fusion reactions, we found a good mass separation of the transported fusion-evaporation residues, and very low background condition was obtained.

---

[1] Japan Atomic Energy Agency (JAEA)
[2] University of Tennessee
[3] Oak Ridge National Laboratory
[4] University of York
[5] GSI Helmholtzzentrum

References

[1] R. D. Macfarlane and A. Siivola, Phys. Rev. Lett., 14, 114 (1965).

[2] S.N. Liddick et al, Phys. Rev. Lett. 97,082501 (2006).

[3] I. Darby et al., Phys. Rev. Lett. 105, 162502 (2010).

[4] B. Cederwall et al., Nature, 469, 68 (2011).

[5] B.A. Brown and K. Rykaczewski, Phys. Rev. C50, R2270 (1994).

[6] C.B. Hinke et al., Nature, 486, p. 341 (2012).

[7] C. Mazzocchi et al., Phys. Rev. Lett., 98, 212501 (2007).

[8] H. Schatz et al., Phys. Rev. Lett., 86, 3471 (2001).

[9] V. V. Elomaa et al., Phys. Rev. Lett. 102 , 252501 (2009).

3.2 Measurement of fission fragment mass distributions of compound nuclei populated by multi-nucleon transfer reaction in ^{18}O + ^{232}Th

K. Nishio[1], R. Léguillon[1], K. Hirose[1], H. Makii[1], I. Nishinaka[1], O. Riccardo[1], T. Ishii[1], K. Tsukada[1],

M. Asai[1], S. Chiba[2], T. Ohtsuki[3], S. Araki[4], Y. Watanabe[4], R. Tatsuzawa[5], N. Tamura[6] and S. Goto[6]

Mass distributions of fission fragments for neutron induced fissions of actinide nuclei are the important nuclear data for atomic energy applications. In nuclear reactors with highly burned nuclear fuels and next generation fast breeder reactors, it is necessary to consider fission of minor actinides with relatively short half-lives. Delayed neutron yields are also one of the important data, because it will influence the reactor response. The delayed neutron yield is sensitive to the fission fragment mass and charge distributions. In this experimental program, we are promoting the measurement of the fission fragment mass distributions for short-lived actinide nuclei, whose data for neutron-induced fissions are practically impossible to take. We use multi-nucleon transfer reactions to populate the excited compound nuclei using an ^{18}O beam and an available actinide target. We can also produce fission data for neutron-rich nuclei, which cannot be accessed by fusion reaction.

Fission properties of excited compound nuclei populated in the multi-nucleon transfer reaction ^{18}O + ^{232}Th were measured. The experiment was carried out at the JAEA tandem accelerator. Energy of the ^{18}O beam was 157.0 MeV. Projectile-like nucleus produced in multi-nucleon transfer reaction was identified using silicon ΔE-E detectors, and its energy was measured to assign the excitation energy of the compound nucleus. Two fission fragments were detected by position-sensitive multiwire-proportional counters (MWPCs). Time difference between the two MWPCs was recorded. Fission fragment masses were determined with the kinematic consideration by refereeing the velocity and the direction of recoiled fissioning nuclei which were determined by detecting the projectile-like nucleus.

Example of the preliminary fission data is shown in Fig. 1, where fission events of ^{233}Th* and ^{234}Th* are plotted on the plane of fragment mass and excitation energy of the fissioning nucleus. Similar data for other Th, Pa, and U isotopes will be obtained.
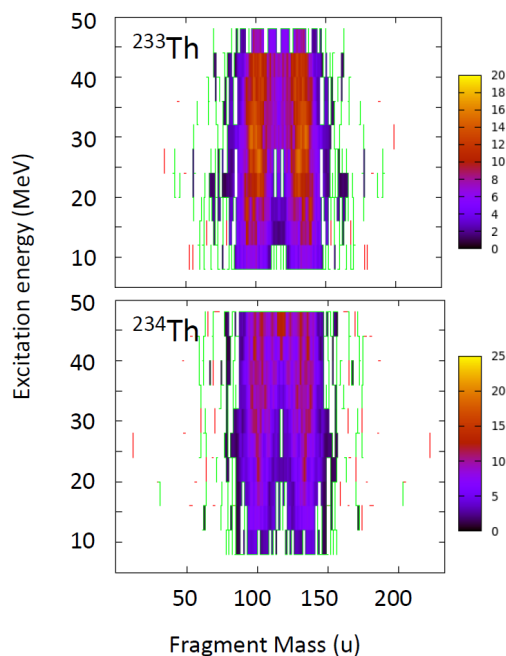
Fig 1. Fission events plotted on the plane of fragment mass and excitation energy of compound nucleus. Data for ^{233,234}Th* are shown.

[1] Japan Atomic Energy Agency (JAEA)
[2] Tokyo Institute of Technology
[3] Kyoto University
[4] Kyushu University
[5] Tokyo City University
[6] Niigata University

3.3 Measurements of a branching ratio of ^{22}Ne(α,γ)^{26}Mg/^{22}Ne(α,n)^{25}Mg reactions

S. Ota[1], H. Makii[1], T. Ishii[1], C. Angell[1], S. Chiba[2], I. Nishinaka[1], K. Nishio[1] and S. Mitsuoka[1]

In the He-burning phase of massive stars, the ^{22}Ne(α,n)^{25}Mg reaction is considered to be a main neutron source driving the synthesis of nuclides in the A=60-90 mass range during the *s* process [1]. A variety of attempts to experimentally determine the rate for this reaction at the Gamow window corresponding to *s* process temperatures (T = 0.2-0.3 GK) have been made either through direct ^{22}Ne(α,n)^{25}Mg measurements [e.g., 3-6] or indirect measurements by such as ^{22}Ne(^{6}Li,d)^{26}Mg reactions [3, 4]. However, direct measurements have been hindered by the small cross section due to the Coulomb barrier and the resonances at E_α < 830 keV have not been identified with this method. The indirect measurements have identified many low-energy resonances, but unambiguous determination of the resonance parameters such as J^π, Γ, Γ_γ, Γ_n and Γ_α in ^{26}Mg produced by α + ^{22}Ne has remained a longstanding problem especially for resonances near the Gamow peak. Of these uncertainties, the ratio of Γ_n and Γ_γ to determine the branching ratio of n and γ emission channels plays an important role in obtaining the neutron yield for the *s* process. The ^{22}Ne(α,γ)^{26}Mg reaction (Q=10.615 MeV), which competes with the ^{22}Ne(α,n)^{25}Mg reaction (open above the excitation energy of ^{26}Mg, E_x=11.093 MeV), may be of considerable strength and could significantly suppress neutron production during He burning (E_x=10.9-11.5 MeV). To address this problem, we studied the ^{6}Li(^{22}Ne,^{26}Mg)d α-transfer reaction in this work. Because both the α and ^{22}Ne have ground states with J^π=0$^+$, the α-transfer reaction preferentially populates natural parity states in ^{26}Mg. This helps to enable studies of the astrophysically relevant natural parity states in ^{26}Mg. Furthermore, the inverse kinematics approach enables us to determine Γ_n / Γ_γ by direct measurements of the ratio of ^{25}Mg and ^{26}Mg.

Si ΔE-E detectors are used for particle identification for both the recoils and ejectiles. For the detection of Mg ions (downstream of the target), we used 20 μm thick surface-barrier detectors backed by 300 μm thick PIN diode detectors. For the detection of deuterons (upstream of the target), we used 75 μm thick ion-implanted detector backed by 300 μm thick PIN diode detectors. Total energy resolution for determining deuteron energies in the experiment was 200-300 keV. We performed an experiment using a 110 MeV ^{22}Ne beam from the JAEA-Tokai 20 MV Tandem accelerator. A ^{6}Li-enriched (99%) lithium fluoride (LiF) target with a thickness of 25 μg/cm^2 was prepared on a graphite backing foil (20 μg/cm^2) so that the energy loss of the ^{22}Ne beam and deuterons in those materials will be negligibly small. The beam bombarded the target at an intensity of 10 pnA for 50 hours. For both of the upstream and the downstream detectors, four Si ΔE-E telescopes were used, placed at θ_{CM} = 40° ($\theta_{LAB,deuteron}$ = -108.0°, $\theta_{LAB,Mg}$ = 4.6°). The angles were chosen as a compromise between enhancing the reaction yield and reducing the contribution from elastic scattering of the ^{22}Ne beam. To limit the scattering angle spread of deuterons, we placed slits with an aperture of ϕ=1.5 mm in front of the downstream detectors and used a tightly focused beam spot (ϕ=1 mm). The energies of deuterons were measured to determine excitation energies of ^{26}Mg and the background events such as indirect reaction were

---

minimized to be negligibly small in the data by requiring the coincidence detection of Mg ions and deuterons, which was achieved due to the clear particle identification of Mg from other elements such as Ne [5].

Fig. 1 (a) shows the deuteron spectrum obtained by the experiment. Those deuterons were measured in coincidence with the Mg ions in the forward-angle telescopes. Details of the coincidence detection can be found in [5]. Unfortunately, no clear resonance structure could be confirmed compared to the spectrum obtained in [3] which was measured at almost the same CM angle ($\theta_{CM} \sim 29°$), or to the spectrum simulated based on our experimental condition such as statistics and energy resolution of telescopes (Fig. 1 (b)). This is primarily because of the insufficient energy resolution. Although the best resolution of our detectors give 60-80 keV [5], our new measurement system with a new chamber and vacuum pumping system limited the resolution > 200 keV. Incomplete alignment of the detector system with regard to the beam also might cause the widespread spectrum compared to the simulation. Despite this difficulty, we could still determine whether the expected statistics could be obtained. Although each resonance peak was not identified, we compared the integrated yields from the region corresponding to E_x=10.5-12.1 MeV (i.e., 8.4-9.7 MeV in deuteron energy) to the yield calculated from the cross sections obtained by the normal kinematics experiment [3]. Our results gave 30-45% of the calculated yield. This may be because of incomplete alignment of the detector system. Currently, we study causes of electromagnetic noises that caused the poor energy resolution and discuss our experimental results for a further study.
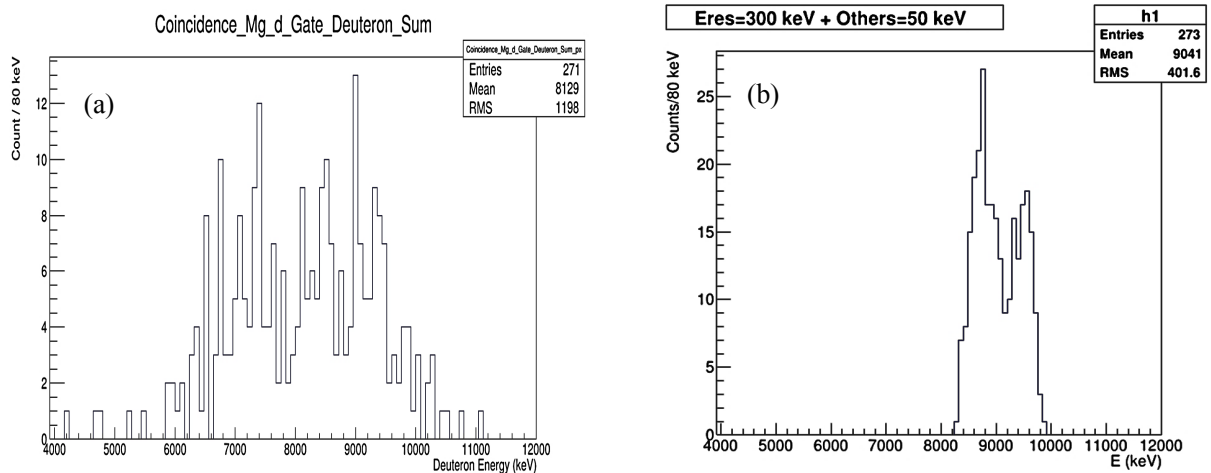
Fig. 1　(a) Deuteron spectrum obtained by coincidence detection with Mg in the preliminary test (θ_{CM} = 40°). (b) A simulated spectrum based on our experimental condition (i.e., assuming 300 keV resolution + 50 keV contribution from angle uncertainties). Yields for individual resonance followed. Note lower and higher energy states than E_x=10.5-12.1 MeV (8.4-9.7 MeV in deuteron energy) were not considered due to the lack of previous data.

References

[1] F. Kappeler, Prog. Part. Nucl. Phys. 43, 419 (1999).

[2] O. Straniero et al., Astrophys. J. Lett. 440, L85 (1995).

[3] U. Giesen et al. , J. D. King, Nucl. Phys. A 561 (1993).

[4] C. Ugalde et al., Phys. Rev. C 76, 025802 (2007).

[5] S. Ota et al., Proceedings of Science (NIC XII) 221 (2012).

3.4   Benchmark experiment of the surrogate ratio method
to determine neutron capture cross-sections

S. Yan[1], Z. Li[1], Y. Wang[1], J. Su[1], Y. Li[1], K. Nishio[2] H. Makii[2], K. Hirose[2] and R. Orlandi[2]

The origin of elements heavier than iron is believed to be of slow and rapid neutron capture processes, and a large number of neutron-capture [(n, γ)] reactions of unstable nuclei are intensely involved [1]. However, the (n, γ) cross-sections are quite hard to be measured directly because of difficulties in manufacture of radioactive samples. The difficulties can be overcome with surrogate ratio method (SRM) [2], which is a variation of the surrogate method [3]. The SRM can yield neutron cross-sections with reasonable accuracies if (1) the weak Weisscopf-Ewing condition defined in Ref. [4] is satisfied, (2) the maximum spin populated by the surrogate reactions is not too large (less than 10 $\hbar$), and (3) the spin and parity distributions in two compound nuclei produced by two surrogate reactions used in the SRM are equivalent. Here condition (1) has been verified by a statistical model calculation [4]. On the other hand, the conditions (2) and (3) were just assumed in Ref. [4]. In the present study, an (^{18}O, ^{16}O) two-neutron transfer reaction is employed to check the conditions (2) and (3) for the determination of (n,γ) cross-sections.

The experiment was carried out at JAEA-Tokai tandem accelerator facility. ^{90}Zr and ^{92}Zr targets (isotopic enrichment of ^{90}Zr and ^{92}Zr are 99.4% and 94.6%, respectively) were bombarded by a 117 MeV ^{18}O beam. Outgoing particles were detected by the Si ΔE-E detector system, which is comprised of Si ΔE detectors in a bowl shape and a Micron S1 type E Si detector, and γ-rays emitted from residual nuclei were measured by two LaBr$_3$(Ce) scintillators with a diameter of 101.6 mm and a length of 127 mm. Figure 1 shows a typical ΔE-E spectrum measured by the Si ΔE-E detector system. The particles are clearly separated according to the mass number. The decay branching ratio of the (n,γ) process can be determined from the ratio of the number of γ-rays in coincidence with ^{16}O particles. The data analysis to determine the decay branching ratio is now in progress.
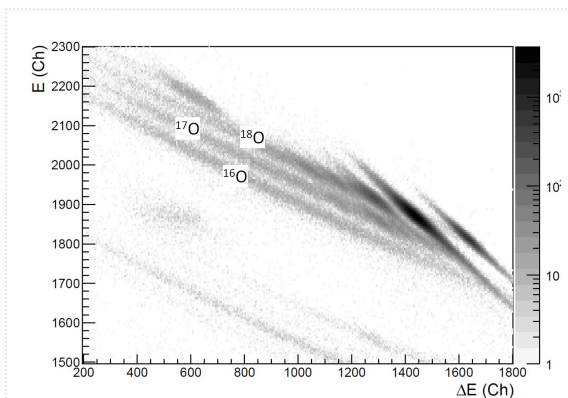
Fig. 1 ΔE-E spectrum for outgoing particles in the reaction of 117 MeV ^{18}O beam and ^{90}Zr target.

References

[1] F. Käppeler et al., Rev. Mod. Phys. 83 (2011) 157-193.
[2] S. R. Lesher et al., Phys. Rev. C 79 (2009) 044609-1-7.
[3] J.E. Escher et al., Rev. Mod. Phys. 84 (2012) 353-397.
[4] S. Chiba and O. Iwamoto Phys. Rev. C 81 (2010) 044604-1-6.

---

[1] China Institute of Atomic Energy (CIAE)
[2] Japan Atomic Energy Agency (JAEA)

3.5　Fragment mass distribution measurement in ^{10}B+^{192,193,196}Au reactions

K. Hirose[1], J.Smallcombe[2], A.N. Andreyev[1,2], K. Nishio[1], I. Nishinaka[1], H. Makii[1],
R. Orlandi[1], T. Ohtsuki[3] and I. Tsekhanovich [4]

A fission fragment mass distribution (FFMD) is one of the important properties of the nuclear fission resulting from the motion of a compound system on a potential energy surface given as a sum of the liquid drop potential and the shell-correction energy. In general, FFMDs for heavier nuclei than, say Ac, have two independent modes, symmetric and asymmetric fissions. It is known that the average mass of the heavy fragments in the asymmetric fission is $A_H\sim140$u at the low excitation energies, which is attributed to the magic numbers of $Z=50$ and $N=82$ or a deformed neutron shell of $N\sim88$[1].

Recently, Andreyev *et al*. have measured FFMD of the post-β-decay daughter nucleus ^{180}Hg[2]. It was expected that this nucleus would lead to two ^{90}Zr fragments since it has magic $N=50$ and semi-magic $Z=40$ which is also shown by the potential energy surface[3](Fig.1). However the fission of ^{180}Hg showed the asymmetric mass split (Fig.2). This new type of asymmetric fission shows the importance of the dynamical understanding, *i.e.,* how the system moves on the potential surface. A theoretical model in which the time evolution of the fissioning system is treated as Brownian shape motion on five-dimensional potential energy surface shows an approximate agreement with the asymmetric fission of ^{180}Hg[4]. This model also predicts asymmetric fissions for many nuclei with $Z<82$. The purpose of this study is to see the predictability of this model by measuring FFMDs in the fusion-fission reactions.The experiment has been performed at JAEA-tandem accelerator facility. For the Au isotopes produced in ^{10}B+W, FFMDs are also predicted as asymmetric fission.

About 100-um thick ^{182,184,186}W targets sputtered on carbon foils(50ug thickness) were irradiated with ^{10}B beam. As shown in Fig.3, two fission fragments(FFs) after the fusion reaction were detected in coincidence using two multi-wire proportional counters(MWPCs). FFMDs were deduced from the time
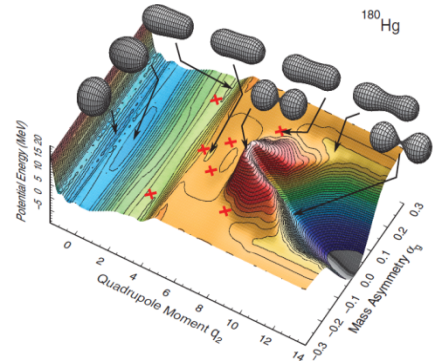
Fig.1 The potential energy surface for ^{180}Hg[3].
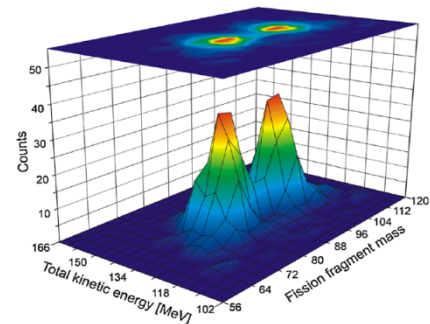
Fig.2 FFMD vs Total kinetic energy obtained for ^{180}Hg[2].
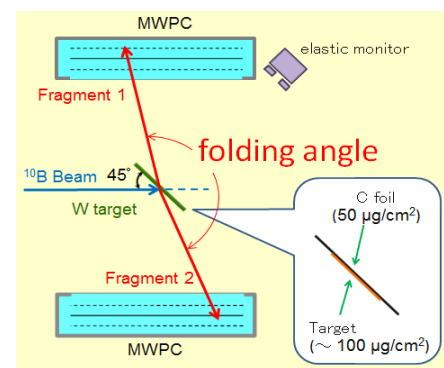
Fig.3 The experimental setup.

---

[1] Japan Atomic Energy Agency (JAEA)
[2] University of York, UK
[3] Kyoto University
[4] University of Bordeaux, France

difference between two FFs and the directions of each FF.

Figure 4 shows the folding angle distributions between two FFs in the ^{10}B+^{182}W reactions at the incident beam energies of 47.0, 55.5, 61.5 and 71.8MeV, respectively. The red dashed lines are the calculated folding angle assuming the fusion-fission reaction using the total kinetic energy from the Viola's systematics[5]. The agreement with the measured distribution means that the fissioning nucleus is ^{192}Au. The folding angle distributions obtained using ^{184,186}W targets are also agree with the fusion-fission assumption.

The obtained FFMDs of ^{192,194,196}Au are shown in Fig.5 where the excitation energies of the compound nuclei are written in right-upper in each panel. It was found that all of the measured FFMD show the symmetric fission in the excitation energy range from 41 to 69MeV.
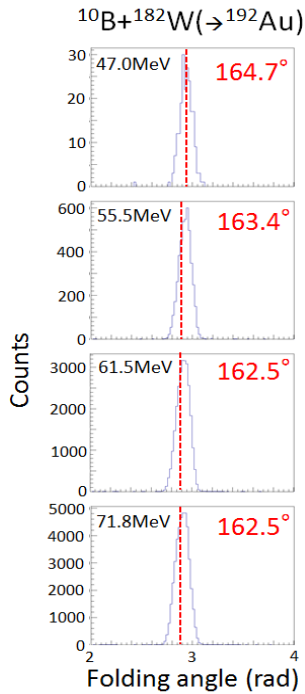
Fig.4 Folding angle distributions between two FFs observed in ^{10}B+^{182}W.
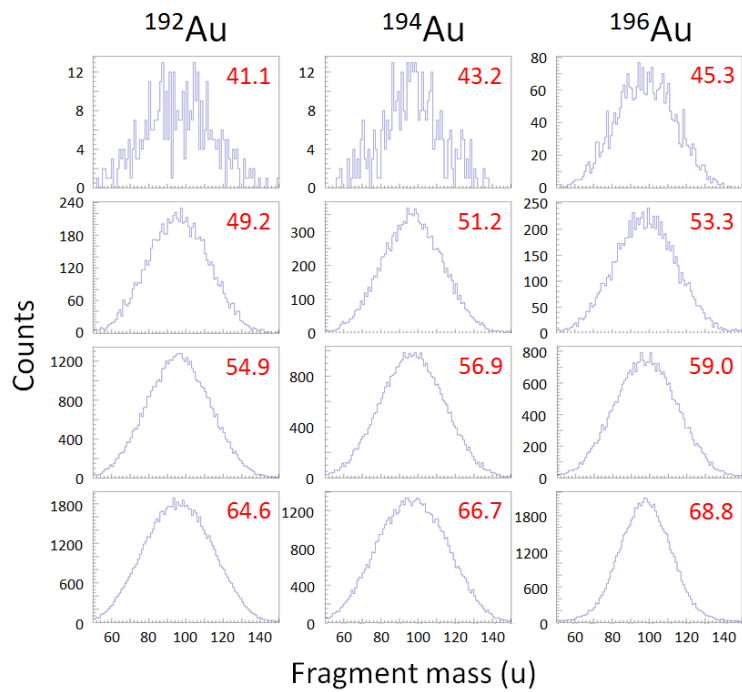
Fig.5 Obtained FFMDs for ^{192,194,196}Au at the excitation energies labeled in each panel.

References

[1] C. Wagemans, editor. *The Nuclear Fission Process*. CRC. Press, (1991).

[2] A.N. Andreyev et al., Phys. Rev. Lett. 105 , 252502 (2010).

[3] T. Ichikawa et. al., Phys. Rev. C86, 024610 (2012)

[4] P. Möller, J. Randrup and A. Sierk, Phys. Rev. C85, 024306 (2012)

[5] V.E. Viola et al., Phys. Rev. C31, 1550 (1985)

3.6 Production of fission isomers by heavy-ion transfer reactions in the sub-barrier energy region

T. Ishii[1], H. Makii[1], K. Nishio[1], I. Nishinaka[1], M. Asai[1] and A. Makishima[2]

We have tried to produce fission isomers using the heavy-ion transfer reactions in the sub-barrier energy region. In this energy region, a projectile collides with a deformed nucleus at the tip of a long axis because of its lower Coulomb barrier energy. Because fission isomers have super deformed shapes, the heavy-ion collision in line with a long axis of the target nucleus may enhance the production of fission isomers.

We have searched a ^{242m}Pu fission isomer, with $T_{1/2} = 3.5$ ns, produced by the ^{238}U(^{18}O, ^{14}C) reaction with the incident energies of 77.8, 82.1, 87.5, and 94.0 MeV. The thickness of the uranium target was 80 μg/cm^2, electrodeposited on a Ni foil. The schematic view of experimental setup is shown in Fig. 1. Two sets of Si ΔE-E detectors were set at 168 ± 7 degrees; the Si ΔE detectors are 20 μm in thickness and 20 mm in diameter. Two sets of multi wired proportional counters (MWPCs) were set at 90 ± 30 degrees. The beam size at the target position was collimated within 3 mm in diameter. The target was covered with a cylindrical shield with a 6 mm inner diameter and 7 mm in length. The cylindrical shield stops fission fragments emitted at the target position. Only fission fragments from a fission isomer, which flies into the forward direction with a velocity of β~0.01, are detected by MWPCs. We have checked that projectile-like fragments can be measured by the Si ΔE-E detectors (Fig. 2) and that fission fragments can be measured by MWPCs using a uranium target without the cylindrical shield. However, no fission events from fission isomers were observed.
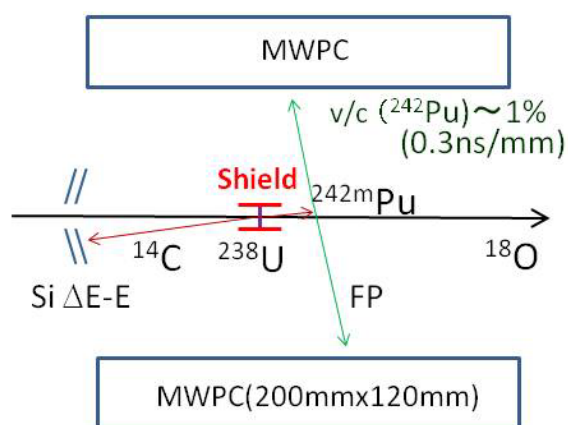
Fig. 1 Schematic view of experimental setup for search of fission isomers produced in the heavy-ion transfer reaction in the sub-barrier energy region.
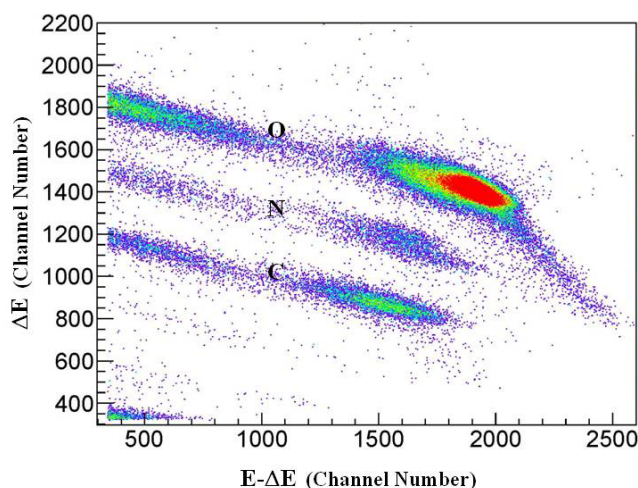
Fig. 2 E-ΔE plot of scattered particles measured by a Si ΔE-E detector placed backwards in the reaction of a 87.5-MeV ^{18}O beam with a ^{238}U target.

---

[1] Japan Atomic Energy Agency (JAEA)
[2] National Defense Medical College

This is a blank page.

CHAPTER 4

Nuclear Chemistry

This is a blank page.

4.1 Synthesis and comparison of astatinated and iodinated amino acid derivatives for the preparation of astatinated peptide

H. Suzuki[1], K. Hashimoto[1], I. Nishinaka[1], Sh. Watanabe[1], I. Sasaki[1] and N. S. Ishioka[1]

Alpha emitting radionuclides have been of interest for several decades as candidates for radiotherapy due to their high cytotoxicity against living cells. ^{211}At (half-life: 7.21 h) is one of the most attractive alpha emitters because its half-life is long enough to accumulate in target tissues and its α-particle energy (5870 keV and 7450 keV from ^{211}Po) is appropriate for therapy [1]. Biologically active peptides have been employed as a targeting molecule for the delivery of radionuclides to target cells in Peptide Receptor Radionuclide Therapy (PRRT) [2,3]. The goal of this study is to prepare an astatinated biologically active peptide for PRRT. Electrophilic destannylation has been exhibited to rapidly substitute astatine for a stannyl group with high yield and under mild conditions [4]. Therefore, astatine labeled peptides will be easily prepared in the presence of peptides containing a stannylated amino acid residue. We have demonstrated synthesis of an astatinated phenylalanine from the stannylated precursor via electrophilic destannylation as a feasible technique. In this study, more detailed studies were carried out to optimize radiolabeling conditions of electrophilic destannylation. We prepared astatinated phenylalanine under various radiolabeling conditions. Radioiodine has been applied for a variety of peptides. Since the chemical properties of astatine are similar to iodine, the closest homologue of astatine, reported iodinated peptides might be able to apply for astatinated peptides [5]. In this study, the radiolabeling reactions of astatinated phenylalanine were compared with iodinated phenylalanine.

Astatine was produced by irradiating a ^{nat}Pb target (1.2 mg/cm^2 thickness) with ^{7}Li beam (45 MeV, 138 nA current) via the ^{nat}Pb(^{7}Li, xn)At reaction. Iodine was also produced similarly via the ^{nat}Sn(^{7}Li, xn)I reaction. At and I isotopes were isolated from the irradiated target using dry distillation as previously described [6]. N-Boc-p-tributylstannylphenylalanine methyl ester was synthesized by procedures reported previously [7]. N-Boc-p-radiohalogenatedphenylalanine methyl esters were obtained by procedures as follows; to a solution containing 10 μL of 0.1, 1 or 10 mg/mL of the stannylated phenylalanine in ethanol was added 90 μL of 1% acetic acid/ethanol containing At or I. Then, 10 μL of 10 mg/mL of chloramine-T (CAT) in ethanol was added (Scheme 1). The mixture was stirred at room temperature for 5 min. The reaction was stopped by adding 10 μL of 10 mg/mL of sodium metabisulfite in H$_2$O. The same experiments without either acetic acid or CAT, or without both acetic acid and CAT were also carried out. The desired compound was confirmed by thin layer chromatography (TLC). A 5 μL of a portion of the reactant was spotted 2 cm from the bottom of a silica gel TLC plate. The plates were developed by dichloromethane/methanol solution (20/1, v/v). After drying, the plates were exposed to the imaging plate for 24 hours, and whereby the distribution of radioactivity on the plates was visualized by the Bioimaging Analyzer System (BAS). The labeling yield was calculated from the measured radioactivity of each spot obtained by the BAS.

---

[1] Japan Atomic Energy Agency (JAEA)

Radiochemical yields of astatination depended on the volume of the stannylated phenylalanine (Table 1). While radiochemical yields of iodination reached a plateau level at 1 mg/mL of precursor, astatination required higher concentration of precursors to obtain sufficient radiochemical yield. The reactions without CAT and acetic acid decreased radiochemical yields of astatination, which suggested both reagents played important roles to facilitate astatination. Although the radiochemical yield of astatination was lower than that of iodination, astatinated phenylalanine was successfully synthesized in 73% radiochemical yield in the presence of 10 mg/mL of the precursor. On the base of studies described herein, we are planning to synthesize an astatinated peptide via electrophilic destannylation.
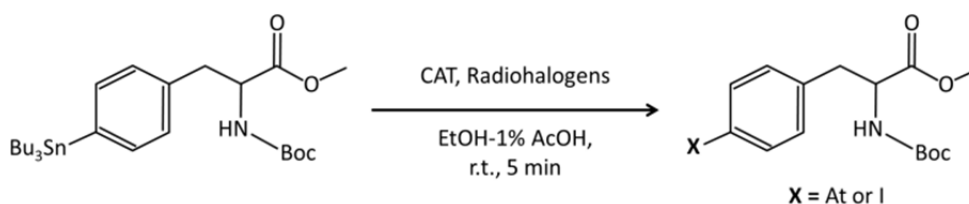
Scheme 1. Reaction scheme of radiohalogenated phenylalanine.

Table 1. Radiochemical yields of each conditions (+ means addition and -means no addition).

Phenylalanine derivative (mg/mL)	CAT (oxidant)	Acetic acid	Radiochemical yield of At (%)	Radiochemical yield of I (%)
0.1	+	+	23.8±4.1	64.6±6.9
1	+	+	64.4±6.3	78.4±9.5
10	+	+	73.1±6.8	78.4±9.9
10	-	+	43.4±8.3	76.3±12.1
10	+	-	51.7±6.8	71.1±22.2
10	-	-	9.3±5.3	49.3±24.1

References

[1] D. S. Wilbur, Curr. Radiopharm., 1 (2008) 144-176.

[2] V. Ambrosini et al., J. Nucl. Med., 52 (2011) 42S-55S.

[3] M. M. Graham and Y. Menda, J. Nucl. Med., 52 (2011) 56S-63S.

[4] M. J. Adam, and D. S. Wilbur, Chem. Soc. Rev., 34 (2005) 153-163.

[5] G. Vaidyanathan et al., Bioconjugate Chem., 17 (2006) 195-203

[6] I. Nishinaka et al., JAEA-Review 2013-002 (2013) 33-34.

[7] I. Sasaki et al., Peptide Sci., 2012 (2013) 157-160.

4.2 Measurement of [7]Li-induced reaction cross sections of [209]Bi for development of a [211]Rn-[211]At generator

E. Maeda[1], A. Yokoyama[2], T. Taniguchi[1], K. Washiyama[3] and I. Nishinaka[4]

One of the radioisotope applications attracting much attention in recent years is "Radionuclide therapy", which is the treatment of cancer by administering tumor specific carrier molecules labeled with radionuclide to the human body. Highly energetic α-particles are expected to suppress tumor cell growth efficiently without damaging to surrounding tissues because of their short path lengths in tissues (<100 μm). Among α radionuclides, [211]At has drawn attention as a promising α-emitter due to its half-life of 7.2 h and due to its chemical property as a halogen like ^{131}I which has already been applied to radionuclide therapy. However, its half-life makes it difficult to use at hospitals away from the isotope production facility. We therefore focused on the [211]Rn-[211]At generator technology to use [211]At in distant place by milking a disintegration product from [211]Rn as a parent nuclide. In the transient equilibrium of [211]Rn-[211]At both activities decay with the parent's half life of 14.7 h. The generator technology enables us to transport [211]At over approximately twice the distances. In the [7]Li+[209]Bi reaction the production cross sections of [211]Rn via $5n$ evaporation channel, [209]Bi([7]Li, $5n$)[211]Rn, have been measured [1,2]. There is, however, no report on reliable production cross sections of [210]Rn and [210]At via $6n$ and $p+5n$ evaporation channels, [209]Bi([7]Li, $6n$)[210]Rn and [209]Bi ([7]Li, $p5n$) [210]At, respectively. Both nuclides [210]Rn and [210]At are precursors to [210]Po, a noteworthy radiotoxic nuclide due to its accumulation in human bone and its alpha radioactivity of 138 days in half-life. Therefore it is very important to acquire these excitation functions for the application to the radionuclide therapy. We have performed measurements on the excitation functions of [211]Rn, [210]Rn and [210]At in the [209]Bi+[7]Li reaction to establish the [211]Rn-[211]At generator technology.

Targets of [209]Bi were prepared by vacuum deposition on aluminum foil of high purity (99.999%). Stacks of several [209]Bi targets were irradiated with 60 MeV [7]Li beam with a current of 50-70 pnA from the JAEA-Tokai tandem accelerator. We obtained the production cross-sections for [211]Rn, [210]Rn and [210]At by the non-destructive gamma measurement with a HPGe detector. The cross section for [210]Rn decaying into [206]Po was obtained from the yield of [206]Po. The independent yield of [210]At was obtained by discriminating the contribution from its precursor [210]Rn.

In Fig.1 are shown the observed [7]Li+[209]Bi excitation functions with reported data [1] and cross sections predicted by the statistical model calculation (HIVAP code) coupled with the CCDEF code [3]. The cross sections for [211]Rn in the present study tend to be slightly higher than those in the report [1], where the production of [211]Rn might be underestimated because of its loss during the chemical procedures including

---

dry distillation from an irradiated target. In contrast, in the measurements of the present study, loss of the product is not likely to happen because of the non-destructive measurement. Independent cross sections of ^{210}Rn and ^{210}At in the present study largely deviate from the sum of cross sections of ^{210}Rn and ^{210}At in Ref. [1]. The reason of this large deviation is not clear but the cross section of ^{206}Po produced through α-decay of ^{210}Rn with a probability of 96% reliably provides that of ^{210}Rn in the present study. We obtained both the independent cross sections of ^{210}Rn and ^{210}At for the first time.

Observed cross sections of ^{211}Rn and ^{210}Rn produced via ^{209}Bi(^{7}Li, $5n$)^{211}Rn and ^{209}Bi(^{7}Li, $6n$)^{210}Rn, respectively, tend to be less than theoretical values, although the discrepancy between the values becomes smaller as the incident energy increases. On the other hand, observed values of ^{210}At obviously exceed the theoretical values for ^{209}Bi (^{7}Li, $p5n$) ^{210}At. A weakly bound ^{7}Li nucleus is easily decomposed to ^{4}He and ^{3}H nuclei [2]. Such break-up reaction possibly leads to an incomplete fusion-evaporation reaction similar to ^{209}Bi(^{4}He, $3n$)^{210}At. It should be noted that the statistical model calculation [3] doesn't involve incomplete fusion following break-up. Thus, the contribution of break-up will result in the discrepancy of the calculations from experimental data. In the production of ^{210}At, the result suggests that the break-up reaction of ^{7}Li on ^{209}Bi plays a crucial role. However, it does not significantly affect the production of the radiotoxic nuclide ^{210}Po since its cross sections are much smaller than those of ^{211}Rn.
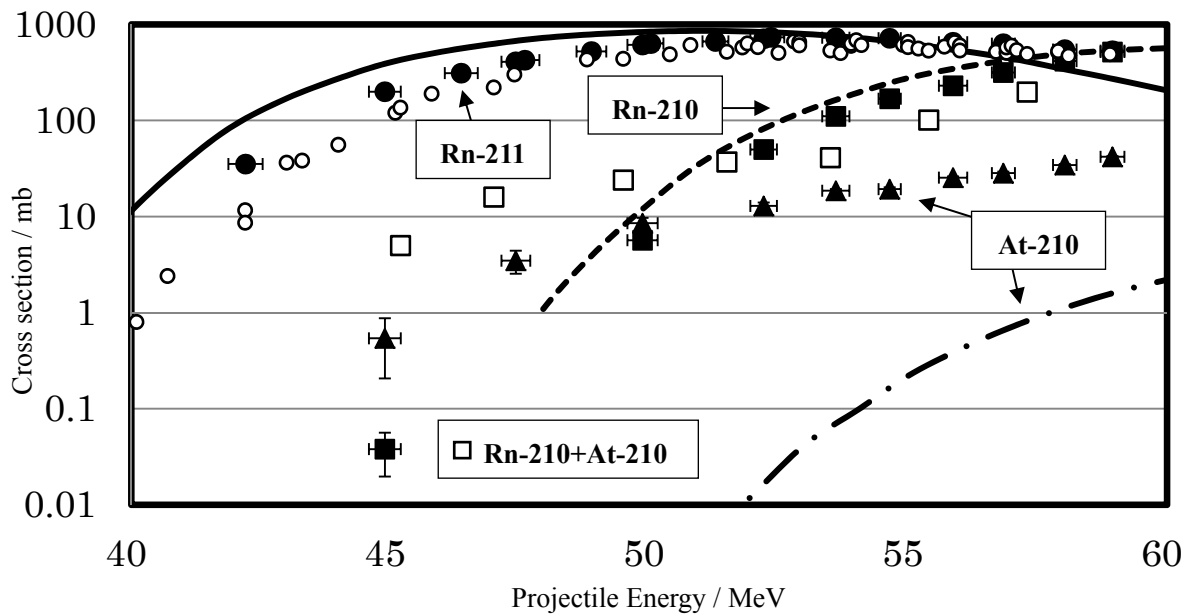
Fig.1 Excitation functions for ^{211}Rn, ^{210}Rn, and ^{210}At in the ^{7}Li+^{209}Bi reaction. Solid marks are the cross section measured in the present study, open marks those measured by Meyer et al. for ^{211}Rn and the sum of ^{210}Rn and ^{210}At [1], and lines those calculated by the statistical model calculation [3].

References

[1] G.-J. Meyer and R.M. Lambrecht, Int. J. Appl. Radiat. Isot., 31 (1979) 351-355.

[2] M. Dasqupta et al., Phys. Rev. C, 70 (2004) 024606-1-20.

[3] K. Nishio et al., Phys. Rev. C, 62 (2000) 014602-1-12.

4.3   Production of ^{95m}Tc for compton camera imaging

Y. Hatsukawa[1], K. Hashimoto[1], K. Tsukada[1], T.K. Sato[1], M. Asai[1], A. Toyoshima[1], Y. Nagai[1],
T. Tanimori[2], S. Sonoda[2], S. Kabuki[3], H. Saji[4] and H. Kimura[4]

In this study, ^{95m}Tc isotope was produced via the ^{nat}Mo(p, n)^{95m}Tc reaction at the Tandem accelerator. ^{95m}Tc produced in the MoO_3 target was separated and purified by the method according to previous study [1]. Irradiated proton beam currents were monitored with Faraday cup connected to a current integrator, and averaged beam currents were 1.2 μA. After a few weeks cooling time, about 500 kBq of ^{95m}Tc were extracted from the irradiated MoO_3 target after a chemical separation procedure.

A Compton camera imaging of gamma ray form ^{95m}Tc was taken by the ETCC (electron tracking Compton camera) which is developed by the Prof. Tanimori's group at Kyoto University [2-7].   The ETCC consists of two detector parts. A gamma ray is scattered in the first detector which is a micro-time projection chamber (μ-TPC) [8,9]. The μ-TPC can catch the 3D recoil electron track [14]. The scattered gamma ray is caught by the second detector which composed of pixel scintillator arrays. The ETCC can construct the gamma-ray direction event by event, using information from the electron track and absorption point of the scattered gamma ray. In this imaging study, an intensity of ^{95m}Tc is 170 kBq contained in ϕ10mm plastic vial was used as a radiation source which was placed at 10cm away from top of camera head.

Using the ETCC at Kyoto University, we have succeeded in imaging the ^{95m}Tc for 204 keV, and the tentative imaging result is shown in Fig. 1. The energy window of the ETCC is 170 – 230 keV, and number of accepted gamma ray events is 311 events. Also this image was reconstructed by an iterative reconstruction technique which is maximum likelihood expectation maximization (MLEM) method using list-mode data [10]. The obtained image taken by the ETCC is distributed about ϕ30mm diameter. A higher position sensitivity image can be reconstructed by more careful data analysis event by event. And become more high energy, spatial resolution of the ETCC will be better because of Compton scattering phenomena. This is the first Compton camera imaging picture with gamma rays from ^{95m}Tc isotope.

From results of this study, we show the possibility of new diagnostic tests using the Compton camera imaging with ^{95m}Tc-labelled compounds instead of the SPECT imaging with ^{99m}Tc.   In the future, ^{96}Tc is more suitable for actual diagnostic test for human body than ^{95m}Tc because of their half-lives.

―――――――――――――――――

[1]Japan Atomic Energy Agency (JAEA),

[2]Department of Physics, Kyoto University,

[3]School of Medicine, Tokai University,

[4]Faculty of Pharmaceutical Sciences, Kyoto University
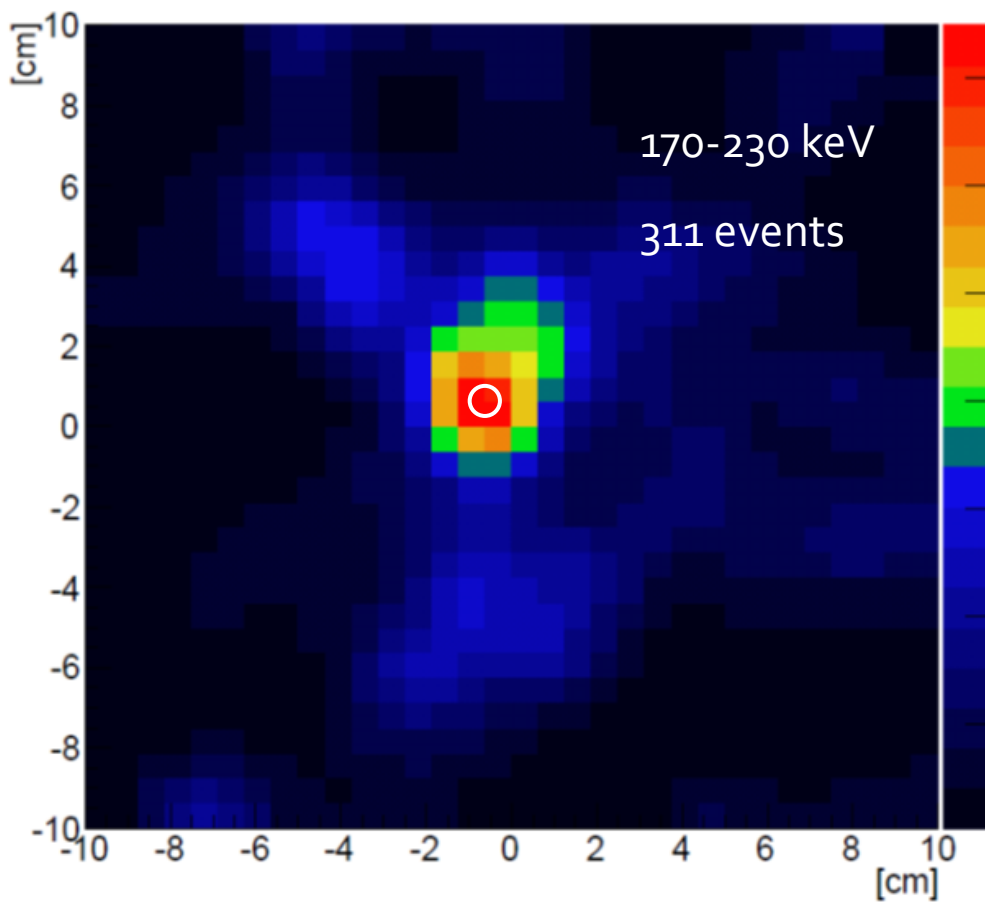
Fig.1 Compton camera imaging obtained from ^{95m}Tc contained in a 10 mm diameter vial. Energy window is 170 -230 keV. From accepted 311 gamma ray events, this image was reconstructed by an interactive reconstruction technique. White circle shows size of 10 mm diameter vial. Most of events were found within 30 mm diameter.

References

[1] M.Izumo, et al., Appl. Radiat., Isot. 42 (1991) 287-301.

[2] T. Tanimori, et al., New Astron. Rev. 48 (2004) 236-241.

[3] R. Orito, et al., Nucl. Instrum. Methods Phys. Res., A513 (2003) 408-412.

[4] A. Takada, et al., Nucl. Instrum. Methods Phys. Res., A546 (2005) 258-262.

[5] S. Kabuki, et al., Nucl. Instrum. Methods Phys. Res., A580 (2007) 1031-1035.

[6] S. Kabuki et al., Nucl. Instrum. Methods Phys. Res., A623(2010) 606-607.

[7] T. Nagayoshi, et al., Nucl. Instrum. Methods Phys. Res., A546(2005) 457-465.

[8] A. Ochi, et al., Nucl. Instrum. Methods Phys. Res., A471(2001) 264-267.

[9] H. Kubo, et al., Nucl. Instrum. Methods Phys. Res., A513(2003) 94-98.

[10] S.J. Wilderman, et al., IEEE Trans. Nucl. Sci. NS-45 (1998) 957.

4.4　Medical Radioisotope Production with Accelerator Neutrons by Deuterons

K. Tsukada[1], N. Sato[1], M. Asai[1], T.K. Sato[1] and Y. Nagai[1]

We are proposing a new system for the generation of medical radioisotopes with accelerator neutrons by deuterons [1], especially the production of ^{99}Mo ($T_{1/2}$ = 66 h), ^{90}Y ($T_{1/2}$ = 64 h), ^{67}Cu ($T_{1/2}$ = 61.8 h), and ^{64}Cu ($T_{1/2}$ = 12.7 h). The most common diagnostic radioisotope, ^{99m}Tc ($T_{1/2}$ = 6 h), has been obtained from ^{99}Mo ($T_{1/2}$ = 66 h) which has been produced mostly by the fission reaction of highly enriched ^{235}U in research reactors around the world. A recent shortage of ^{99}Mo worldwide triggered discussions on the supply of ^{99}Mo, and a number of ^{99}Mo and ^{99m}Tc production methods with reactors and accelerators have been investigated. The positron emitting radioisotope ^{64}Cu and β⁻-ray emitting radioisotope ^{67}Cu are promising radionuclides suitable for labeling many radiopharmaceuticals for PET imaging and for treating small distant metastases in radioimmunotherapy, respectively. Their generally adopted production routes are ^{64}Ni(p,n)^{64}Cu and ^{68}Zn($p,2p$)^{67}Cu, respectively. However the use of ^{67}Cu for clinical researches has been limited due to the difficulty in obtaining sufficient quantities. ^{90}Y-ibritumomab tiuxetan (Zevarin®), a radiopharmaceutical agent, a pure β⁻-ray emitter with a maximum energy of 2.28 MeV, has been used for cancer therapy. ^{90}Y is obtained from ^{90}Sr ($T_{1/2}$ = 28.8 y), which is produced by the fission reaction of ^{235}U. In our study, we investigated a potential of accelerator neutrons to produce ^{99}Mo, ^{64}Cu, ^{67}Cu and ^{90}Y [2,3,4], and we were successfully produced the isotopes which irradiated by accelerator neutrons obtained by the ^{nat}C(d,n) using 40 MeV deuterons provided from TIARA cyclotron. In this study, we investigated to obtain an excitation function of the productions by the ^{90}Zr(n,x) reaction.
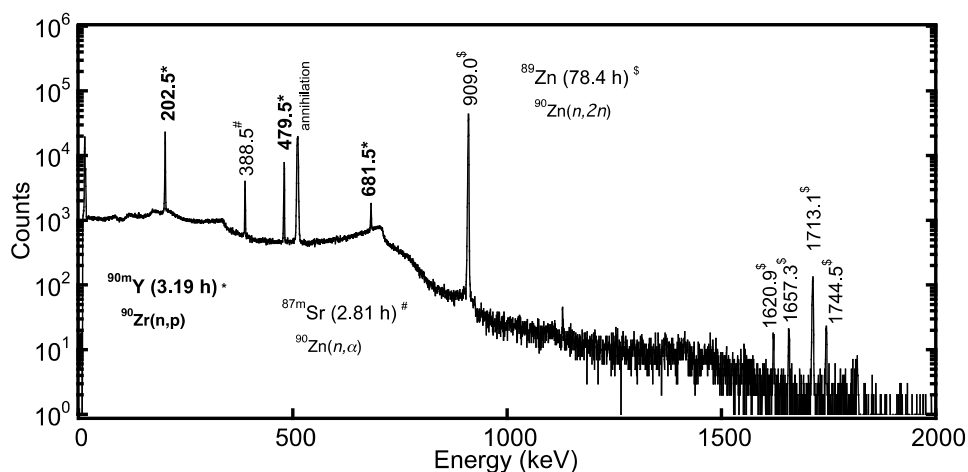
Fig. 1　A γ-ray spectrum of the ^{90}ZrO$_2$ sample irradiated with neutrons, which were obtained by the ^{nat}C(d,n) using 30 MeV deuterons. It was taken 5 hours after the end of irradiation.

Enriched ^{90}Zr oxide samples with a radius of 10 mm and a weight of about 200 mg were irradiated with neutrons, which were obtained by the ^{nat}C (d,n) using 12 - 30 MeV deuterons provided from the JAEA

---

[1]　Japan Atomic Energy Agency (JAEA)

tandem accelerator. These samples were placed at 9 mm between the ^{nat}C target and the sample position in the air. After a bombardment we measured a γ-ray spectrum of the reaction products produced by the ^{90}Zr(n,x) reaction with a HPGe detector. In Fig. 1, we show a γ-ray spectrum from the decay of ^{90m}Y (at 203, 408, and 682 keV) which was produced with ^{90}Y via the ^{90}Zr(n,p) reaction, ^{89}Zr (909 keV) and ^{87m}Sr (389 keV). The activity of the pure β⁻-ray emitter ^{90}Y is estimated from the observed activity of ^{90m}Y by a literature value [5]. The excitation functions of ^{90m}Y, ^{89}Zr and estimated ^{90}Y were shown in Fig.2. Since the activity of ^{90}Y was found to be comparable to that of impurity nuclide ^{89}Zr (T$_{1/2}$ =78.4 h), ^{90}Y will be separated from ^{89}Zr by using an ion-exchange separation method and purified. The present results demonstrate that the medical radioisotopes, ^{90}Y, can be produced by using fast neutrons from the ^{nat}C (d,n) reaction.
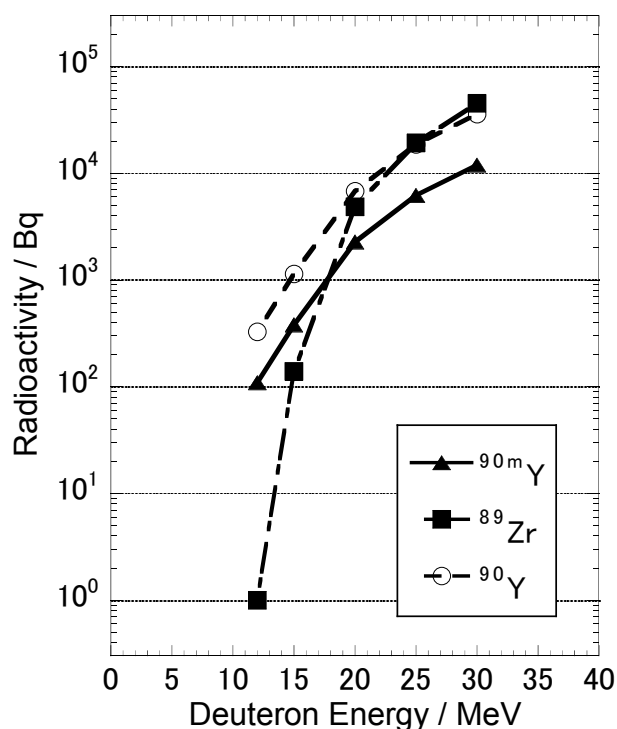
Fig. 2   Observed excitation functions of the productions, ^{90m}Y, ^{89}Zr, and ^{90}Y, by the ^{90}Zr(n,x) reaction .

References

[1] Y. Nagai et al., J. Phys. Soc. Jpn. 82 (2013) 064201.

[2] Y. Nagai and Y. Hatsukawa, J. Phys. Soc. Jpn. 78 (2009) 033201.

[3] T. Kin et al., J. Phys. Soc. Jpn. 82 (2013) 034201.

[4] Y. Nagai et al., J. Phys. Soc. Jpn. 78 (2009) 113201.

[5] S. M. Qaim et al., Phys. Rev. C42 (1990) 363.

4.5 Batch reduction and extraction experiments of Mo and W for a future reduction experiment of seaborgium (Sg)

A. Toyoshima[1], S. Miyashita[2], K. Ooe[3], M. Asai[1], M. F. Attallah[4], N. Goto[3], N. S. Gupta[4], H. Haba[5],

M. Huang[1,5], M. Kaneko[2], J. Kanaya[5], Y. Kaneya[1,6], Y. Kasamatsu[7], Y. Kitatsuji[1], Y. Kitayama[6], K. Koga[2],

Y. Komori[5,7], T. Koyama[3], J. V. Kratz[9], H. V. Lerum[4], Y. Oshimi[3], V. Pershina[10], D. Sato[3], T. K. Sato[1],

Y. Shigekawa[7], A. Shinohara[7], A. Tanaka[3], K. Tsukada[1], S. Tsuto[3], A. Vascon[1], T. Yokokita[7], A. Yokoyama[8],

J. P. Omtvedt[4], Y. Nagame[1] and M. Schädel[1,10]

Seaborgium (Sg) is expected to be redox-active similar to its lighter group-6 homologs, Mo and W. Theoretical calculation shows that seaborgium (Sg) can be reduced from the most stable hexavalent state Sg(VI) to, e.g., the tetravalent one [1]. In such reduction reactions, electrons occupy the vacant valence 6d orbital of the Sg(VI) ion. The redox potential of the Sg(IV)/Sg(VI) couple, therefore, provides information on the stability of the 6d orbital which is influenced by increasingly strong relativistic effects.

Because of low production rates of ^{265a,b}Sg (a and b show two different states) in the ^{248}Cm(^{22}Ne, $5n$) reaction and their short half-lives ($T_{1/2}$) of 8.5 s and 14.4 s [2], only single atoms of Sg are present during an experiment. This means that standard electrochemical techniques are not applicable to a reduction study of Sg. Our idea is to observe the reduction of single Sg ions by differences in the solvent extraction behavior between non-reduced Sg(VI) and reduced Sg(IV) species after electrolytic reduction;non-reduced Sg(IV) species are extracted into an organic phase while reduced Sg(VI) remain in an aqueous phase and vice versa. In the present study, we examined the extraction and reduction behavior of carrier-free Mo and W radioisotopes to search for extraction conditions under which chemical species in two different oxidation states are separated.

The radioisotopes ^{93m}Mo ($T_{1/2}$ = 6.9 h) and ^{176}W ($T_{1/2}$ = 2.5 h) were produced in the ^{89}Y(^{7}Li, $3n$)^{93m}Mo and ^{175}Lu(^{7}Li, $6n$)^{176}W reactions, respectively, at the JAEA tandem accelerator. Reaction products transported by a He/KCl gas-jet method at a gas flow rate of 1.5 L/min were deposited on a small plastic piece for 3 min. These were then dissolved with 220 μL of aqueous solution and were introduced into a sample injector. The injected products were then fed into a flow electrolytic column (FEC) [3] at a flow rate of 1.0 mL/min for 1 min. The applied potential was between -1.4 and 0.4 V vs. a Ag/AgCl reference electrode in 1.0 M

LiCl. After the effluent from the column electrode was collected in a plastic vial, 700 μL of the solution was pipetted to another plastic tube to which the same volume of 0.2 M TOA dissolved in toluene had been added. After shaking using a Vortex mixer for 1 min, the mixed sample was centrifuged for 30 s. From both phases, 500 μL aliquots were transferred into two vials. These two samples were then subjected to γ-ray spectrometry with a Ge detector. The distribution ratio (D) was determined as $D = (A_{org} / V_{org}) / (A_{aq} / V_{aq})$ where A_{org} and A_{aq} are the radioactivities in organic and aqueous phases, respectively, and V_{org} and V_{aq} are the volumes of organic and aqueous phases, respectively. We also measured the eluted total amounts of Mo and W from the FEC to determine their chemical yields. The effluent from the FEC at a flow rate of 1.0 mL/min was collected a plastic vial in for 1 min. This sample was measured by γ-ray spectrometry with a Ge detector.

As an example, extraction behaviors of ^{93m}Mo and ^{176}W from 0.1 M H_2SO_4/0.1 M $HClO_4$ into 0.2 M TOA are shown in Fig. 1 as a function of the applied potential of the FEC. The D value of ^{93m}Mo largely decreases for potentials lower than -0.2 V, indicating a successful reduction and separation of Mo. On the other hand, the D values of ^{176}W do not show any clear variation. This means that W was not reduced under the examined conditions. Figure 2 shows the eluted amounts of ^{93m}Mo and ^{176}W from a FEC in 0.1 M H_2SO_4/0.1 M $HClO_4$. The eluted amount of ^{93m}Mo suddenly drops at -0.4 V, while that of ^{176}W gradually decreases with a decrease of the potential. This suggests that Mo (strongly) and W (weakly) are electrodeposited as metals or oxides on a carbon fiber electrode at the corresponding potentials. This unexpected deposition constitutes a serious problem for our future on-line reduction experiments of Sg, yielding very low chemical yields. In the near future, therefore, we will further examine the deposition and extraction behavior of Mo and W using different aqueous solutions such as pure H_2SO_4 and higher acid concentrations to avoid deposition on the electrode.
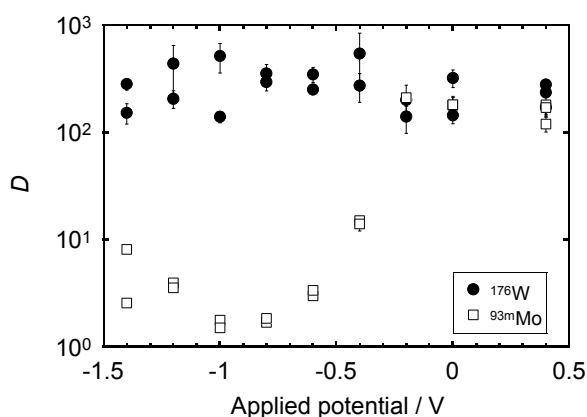
Fig. 1 Distribution ratios (D) of Mo and W in the extraction from 0.1 M H_2SO_4/$HClO_4$ as a function of applied potential of a FEC.
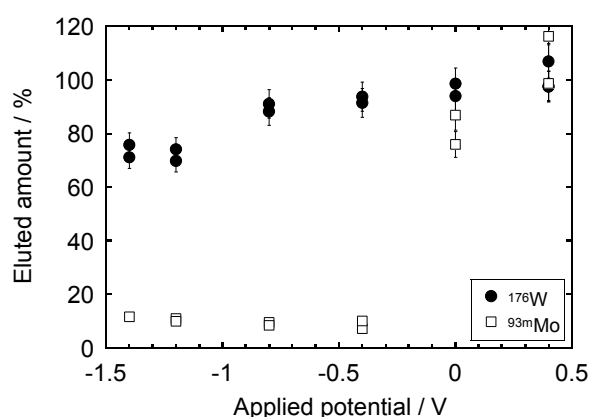
Fig. 2 Eluted amounts of Mo and W from a flow electrolytic column (FEC) as a function of applied potential.

References

[1] V. Pershina et al., J. Phys. Chem. A103 (1999) 8463-8470.

[2] H. Haba et al., Phy. Rev. C85 (2012) 024611-1-11.

[3] A. Toyoshima et al., Radiochim. Acta 96 (2008) 323-326.

4.6 Measurement of overall efficiencies of short-lived lanthanide isotopes with surface ionization ion-source coupled to CdI$_2$ gas-jet transport system

T. K. Sato[1], M. Asai[1], N. Sato[1], Y. Kaneya[1,2], K. Tsukada[1], A. Toyoshima[1], K. Ooe[3], S. Miyashita[4], A. Osa[1], M. Schädel[1], Y. Nagame[1], S. Ichikawa[1,5], T. Stora[6] and J. V. Kratz[7]

The first ionization potential (IP), one of the fundamental physical and chemical properties of an element, of heavy actinides with $Z \geq 100$ has not been determined experimentally. The reason for this is because elements with $Z > 100$, which have short half-lives and which are synthesized at accelerators in heavy-ion reactions with low production rates, are only available in non-weighable quantities down to the one-atom-at-a-time scale. These conditions call for a novel experimental approach different from a well established method like resonance ionization mass spectrometry (RIMS) [1]. In order to determine IP values of the heaviest actinides which have not been investigated so far, we have developed a surface ionization type ion-source for an innovative IP measurement method based on a surface ionization process [2, 3]. We report here on the absolute efficiency of various short-lived lanthanide isotopes with the ion-source coupled to the He/CdI$_2$ gas-jet system.

As shown in Fig.1, the experimental setup consists of an aerosol generator, a target recoil chamber, a gas-jet system with a switch to direct the products either to a surface ionization ion-source installed in the JAEA-ISOL system, or to an aerosol particle collector for a direct catch of the transported activity. Nuclear reaction products produced in the bombardment of a target by an ion beam delivered from the JAEA tandem accelerator are recoiling from the target and are stopped in He gas which is loaded with CdI$_2$ aerosol particles. All products attached to aerosol particles are swept out of the recoil chamber with the He gas flow and are transported to the ion-source. Then,
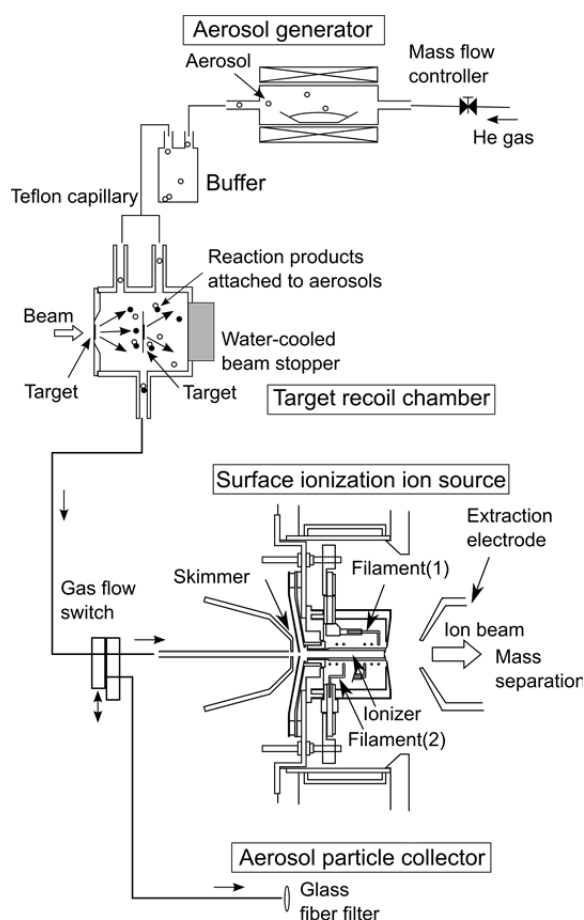
Fig.1 Schematic diagram of experimental setup.

---

[1] Japan Atomic Energy Agency (JAEA)
[2] Ibaraki University
[3] Niigata University
[4] Hiroshima University
[5] RIKEN
[6] CERN
[7] University of Mainz

the nuclear reaction products are ionized on the surface by a surface ionization process and are extracted by an extraction electrode. An ionizer of the ion-source was made from tantalum (Ta) with the inner wall lined with a 50 µm thick rhenium (Re) foil; the ionization process takes place on the Re metal surface. Ionized products are accelerated with 30 kV, mass-separated with a mass resolution of M/ΔM ~ 900, and implanted into an aluminized Mylar tape of a tape transport system installed at the exit of the ISOL set-up. The collected ions were measured by γ-ray spectroscopy with a HP-Ge detector. The absolute efficiency of the entire system is defined as the ratio of the amount of mass-separated isotope to that produced in the target recoil chamber. For efficiency measurements of short-lived isotopes produced in nuclear reactions, various lanthanide isotopes and one rubidium isotope were used as shown in Table 1. Lanthanide isotopes were produced with ^{11}B beams in reactions with mixed targets of ^{136}Ce/^{141}Pr/^{159}Tb and ^{142}Nd/^{148}Sm/^{159}Tb and a ^{162}Dy target, while ^{80}Rb was synthesized in reactions of ^{nat}Ge with ^{11}B. Production yields of each isotope were evaluated from the amount of the isotope observed at the aerosol particle collector based on the absolute efficiency with the He/CdI$_2$ transportation at a He flow rate of 1.8 L min^{-1} and a temperature of 290°C of the CdI$_2$ material, 27 ± 10 %.

All efficiencies are summarized in Table 1. Statistical errors in the γ-ray measurement and systematic errors from the gas-jet transport and the HP-Ge detectors are included in overall errors in the value of efficiency. The present system has been already applied to ionization experiments of short-lived lawrencium (Lr, Z=103) isotope, ^{256}Lr produced in a ^{249}Cf + ^{11}B reaction [2].

Table 1.   Overall efficiencies of various lanthanide isotopes and ^{80}Rb with the present surface ionization ion-source coupled with the He/CdI$_2$ transport system.

Isotope	$T_{1/2}$	Efficiency/%
^{80}Rb	34 s	26 ± 5
$^{142/143}$Eu	1.223/2.59 min	16 ± 3
$^{168m/g}$Lu	6.7/5.5 min	5 ± 1
^{154}Ho	3.10 min	6 ± 1
^{143}Sm	66 s	15 ± 3
^{140m}Pm	5.95 min	12 ± 2
^{148}Tb	2.20 min	3 ± 1
^{165}Yb	9.9 min	4 ± 1

References

[1] N. Erdmann et al., J. Alloys. Comp. 271-273 (1998) 837.
[2] T. K. Sato et al., Rev. Sci. Instrum., 84 (2013) 023304.

CHAPTER 5

Nuclear Theory

This is a blank page.

5.1 New magic number *N*=34 from the energy levels of neutron-rich Ca and Sc isotopes

Y. Utsuno[1], M. Honma[2], T. Otsuka[3], T. Togashi[3], N. Shimizu[3] and T. Mizusaki[4]

The modification of nuclear magic numbers is one of the most attractive subjects in the physics of exotic nuclei. In light nuclei, the conventional magic numbers *N*=8, 20, 28 are known to disappear in neutron-rich regions (for a review, see [1] for instance), whereas a new magic number *N*=16 appears [2,3]. The appearance of the *N*=16 magic number is attributed to sharp decrease of the neutron $d_{3/2}$ orbit as a function of the proton number [4], suggesting considerable evolution of the shell structure in going from normal to exotic nuclei. The mechanism of shell evolution is of great interest in this field. The origin of the appearance of the *N*=16 magic number has been proposed to be strong spin-isospin dependence of the effective interaction [5] for more than a decade, and it has also been predicted that this mechanism gives rise to a new *N*=34 magic number in Ca isotopes. Since then, the *N*=34 magic number has been investigated by a number of experiments, but its existence has been questioned because no signs of this magic number were found for the neighboring isotopes of ^{54}Ca. Finally, a direct measurement of the first excited state in ^{54}Ca has been performed very recently, giving a clear evidence for the existence of the *N*=34 magic number [6].

In this study, we have carried out shell-model calculations for neutron-rich Ca and Sc isotopes, aiming at quantifying the strength of the *N*=34 shell gap and at demonstrating a consistent description of those energy levels. In Figs. 1 and 2, we compare the energy levels among three different shell-model interactions, GXPF1A [7], GXPF1B [8] and GXPF1Br [6], with different *N*=32 and 34 shell gaps. The GXPF1Br interaction is modified from the GXPF1B interaction by fine-tuning the *N*=34 shell gap so as to give a good 2^+_1 energy level in ^{54}Ca. Figures 1 and 2 indicates that not only this energy level but also many other states are improved by this single adjustment, including the $9/2^+_1$ state in ^{51}Ca, the $5/2^+_1$ state in ^{53}Ca, and the 1^+_1 in ^{54}Sc. Those states have a large neutron $f_{5/2}$ component according to shell-model calculations, and thus being very sensitive to the *N*=34 shell gap which is separated between the $p_{1/2}$ and $f_{5/2}$ orbits. As a result, it turns out that the GXPF1Br interaction is a reasonable shell-model interaction for describing this region. The strength of the *N*=34 shell gap is extracted to be about 2.5 MeV from the GXPF1Br interaction. Although this is a modest shell gap being close to the *N*=32 gap, it is much larger than the sub-shell gaps of the Ni region that are less than 1 MeV. Moreover, the order of the neutron $f_{5/2}$ and $p_{1/2}$ orbits changes in going from Ni and Ca. This sharp change in neutron shell structure is considered to be due to cooperation of the tensor and central forces [9], both of which favor the $f_{5/2}$ orbit rather than the $p_{1/2}$ orbit while protons occupy the $f_{7/2}$ orbit. Hence, the *N*=34 magicity suddenly disappears once the valence protons occupy the $f_{7/2}$ orbit, as observed in Sc and Ti isotopes.

---

[1] Japan Atomic Energy Agency (JAEA)
[2] University of Aizu
[3] University of Tokyo
[4] Senshu University
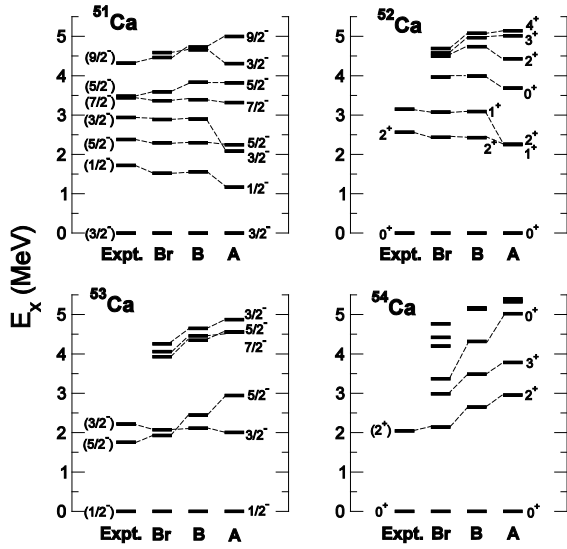
Fig. 1 Energy levels in Ca isotopes for *N*=31-34 compared among experiment (Expt.) and shell-model calculations with the GXPF1A (A), GXPF1B (B), and GXPF1Br (Br) interactions.
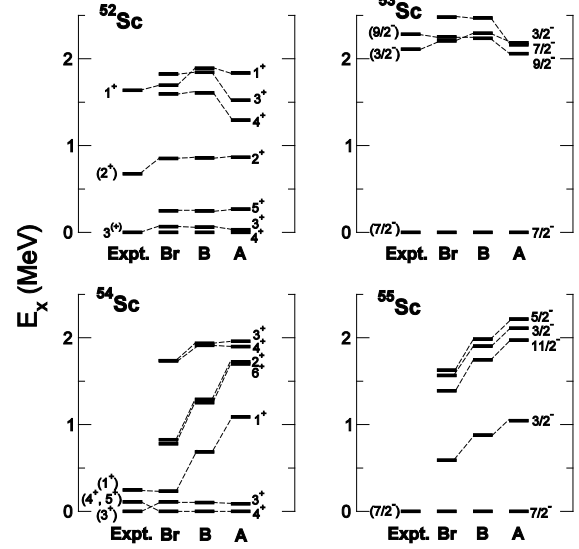
Fig. 2 Same as Fig. 1, but for Sc isotopes.

References

[1] O. Sorlin and M.-G. Porquet, Prog. Part. Nucl. Phys., 61 (2008) 602-673.

[2] A. Ozawa et al., Phys. Rev. Lett., 84 (2000) 5493-5495.

[3] R.V.F. Janssens, Nature, 459 (2009) 1069-1070.

[4] Y. Utsuno et al., Phys. Rev. C, 60 (1999) 054315-1-8.

[5] T. Otsuka et al., Phys. Rev. Lett., 87 (2001) 082502-1-4.

[6] D. Steppenbeck et al., Nature, 502 (2013) 207-210.

[7] M. Honma et al., Eur. Phys. J. A, 25 (2005) 499-502.

[8] M. Honma et al., RIKEN Accelerator Progress Report, 41 (2008) 32-32.

[9] T. Otsuka et al., Phys. Rev. Lett., 104 (2010) 012501-1-4.

5.2   Fission barrier height by the spherical-basis method

H. Koura[1]

A new method of estimating fission barrier heights is presented in which potential energy surfaces are calculated by using the spherical-basis method.   This method is based on an idea of configuration mixing of various spherical states for deformed nuclei, and gave a ground-state nuclear-mass calculation our group presented [1,2]. Under this assumption, the nuclear shell energy with deformations can be expressed as a weighted sum of spherical shell energies, and the weights are obtained from geometric shapes.

Figure 1 shows calculated fission barrier heights for symmetric shapes in the heavy and superheavy nuclear mass region ranging from 76 to 148 of proton number, Z, and from 120 to 270 of neutron number, N. Known nuclei are indicated by small black squares. In this figure, some isolated 'islands' in regions of neutron-deficient heavy and superheavy mass can be seen. The island in the lighter-mass region is found along $N = 126$ with $Z \approx 114$ and 126. This island is caused by a result of the strong shell closure of $N = 126$ and Z=114 and 126, and the barrier heights of these nuclei are over 8 MeV. However, long-lived nuclei in this region are unexpected because this region is far outside the proton drip line as shown this figure. Because of existence of the N=126 shell closure, the fission barriers of the neutron-deficient nuclei near $N \approx 126$ are enhanced, compared to the macroscopic estimation, and some nuclei such as Uranium (Z=92) and Plutonium (Z=94) isotopes would be expected to have rather longer half-lives.
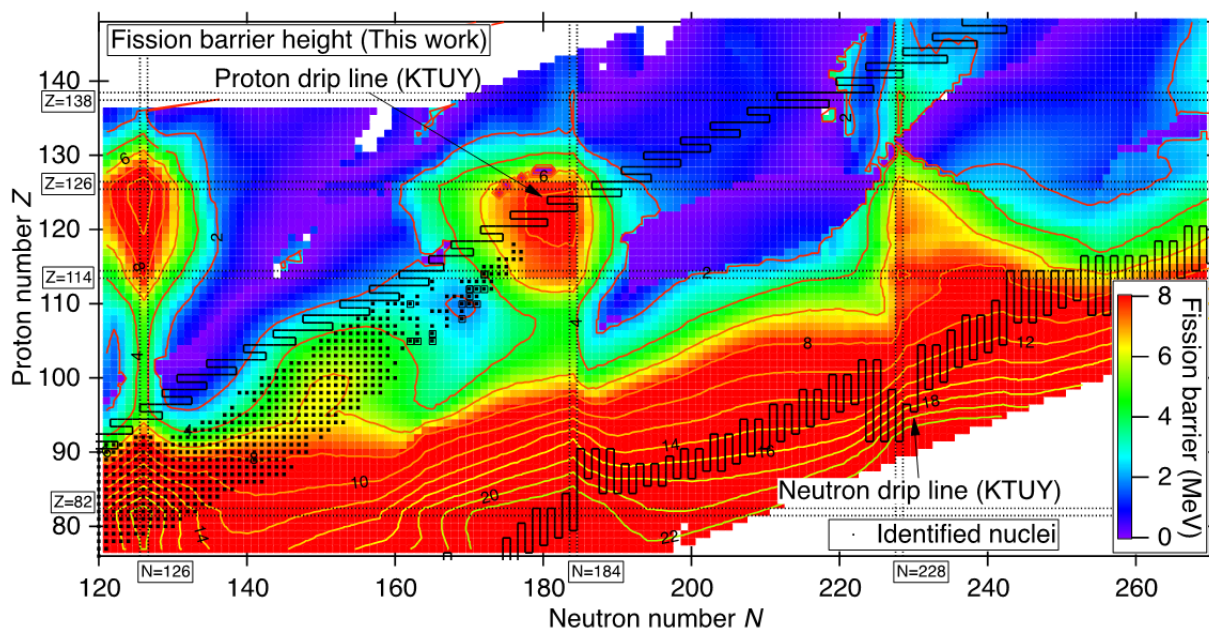
Fig. 1 Fission-barrier height in the heavy and superheavy mass region. Proton and neutron drip lines from the KTUY mass formula [2] are shown as solid lines. Known nuclides are also shown, as small black squares. Nuclei for which fission events were measured to occur at a rate of 10% or more are shown as open squares. These are in the region $Z \approx 110$ and $N \approx 168$, as shown in the figure.

[1] Japan Atomic Energy Agency (JAEA)

The island along $N = 184$ with Z between approximately 114 and 126 is expected to be an island of stability in the superheavy mass region. Calculated barrier heights are over 8 MeV. The adopted nuclear potential in this work results in doubly magic spherical single-particle levels for ^{298}Fl ($Z = 114$) and ^{310}[126] [3]. The predicted proton shell gap of 114 for ^{298}Fl and that of 126 for ^{310}[126] are comparable (actually the gap of 126 is slightly larger than that of 114), and this property results in the creation of an island.

In the much heavier region, a peninsula appeared along $N = 228$ with Z between 114 and 126. This enhanced region is due to the strong shell gap of $N = 228$, and the reason why a well-defined island is not formed is that the nucleus ^{354}[126] is not a doubly magic nucleus in this nuclear potential (see Ref. [3]). The barrier height of this nucleus is obtained as 6.59 MeV, comparable with those of the known actinides. Furthermore, this nucleus is estimated to be β-stable [19]. Therefore, we can expect that this nucleus has a comparatively long half-life.
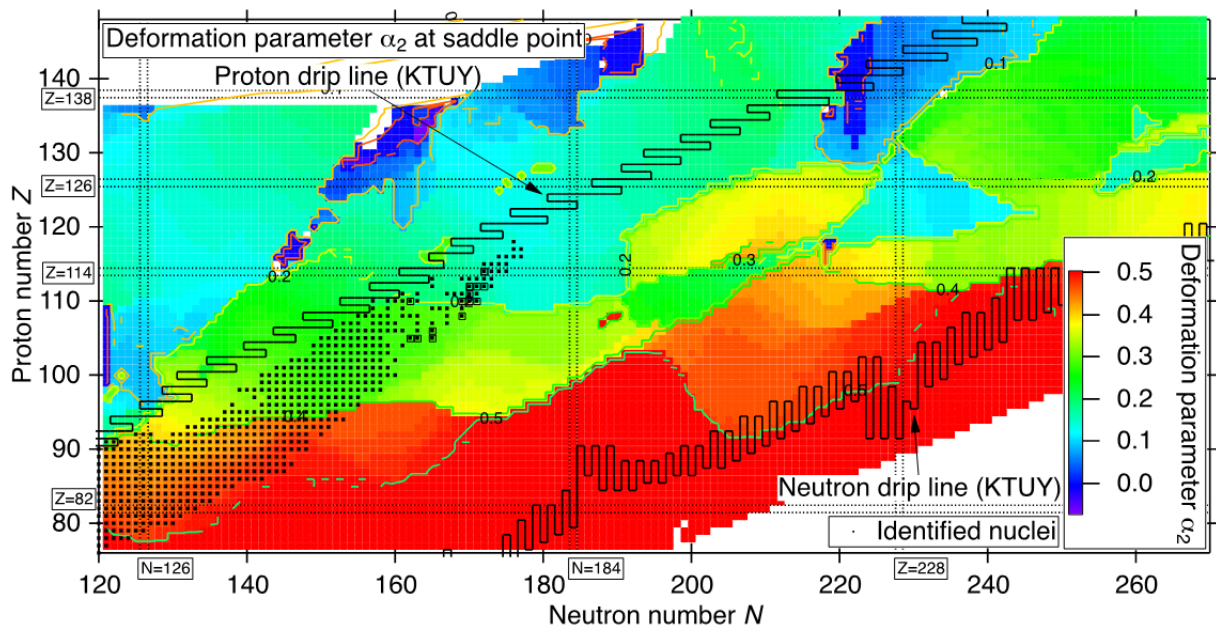
Fig. 2 α_2 deformation parameter at the fission saddle point.

Figure 2 shows the deformation parameter α_2 at the saddle point. In the known actinide region ($90 < Z <103$ and $120 < N < 160$), a distinct border of $\alpha_2 \approx 0.4$ lies along $Z \approx 90\text{-}92$. For higher Z nuclei in the known actinide region, α_2 deformations of the saddle point are approximately 0.2–0.3.

References

[1] H. Koura et al., Nucl. Phys. A 676, (2000) 47 -76.

[2] H. Koura et al., Progr. Theor. Phys. 113, (2005) 305-325.

[3] H. Koura and S. Chiba, J. Phys. Soc. Jpn. 82, (2013) 014201-1-5.

CHAPTER 6

Atomic Physics and Solid State Physics

This is a blank page.

6.1   Development for nanoscale lithium diffusion tracing method in Li ion battery material using [8]Li radioactive tracer

H. Ishiyama[1], S. C. Jeong[1], Y. X. Watanabe[1], Y. Hirayama[1], N. Imai[1], H. Miyatake[1], A. Osa[2], Y. Otokawa[2], M. Matsuda[2], H. Makii[2], T. K. Sato[2], A. Nakao[3], Y. H. Kim[4], M. Mukai[5] and S. Kimura[5]

The diffusion of lithium in materials used in secondary Li-ion batteries is a key factor that determines the rate at which a battery can be charged and discharged. We have developed an in-situ lithium diffusion tracing method using a short-lived radioactive ion beam of [8]Li and successfully applied it to measure diffusion coefficients in Li ionic conductor (e.g. [1]). This method is sensitive to the diffusion over the micrometer scale and the lower limit of the diffusion coefficients (D) obtained by this method is on the order of 10^{-10} cm^2/s [2]. On the other hand, the diffusion coefficient of Li in LiCoO$_2$, which is used as positive electrode material in most Li secondary batteries, has been measured using various methods indirectly. However, the values were scatter over values from 10^{-8} to 5×10^{-14} cm^2/s [3-5]. It is desirable to directly measure the diffusion coefficients using the improved method which has the nanoscale sensitivity for the lithium diffusion. We have proposed a new method by detecting α particles emitted from decayed [8]Li at a small angle relative to a sample surface that is irradiated with a low-energy (the order of keV) [8]Li beam, by which the detection limit can be improved to order of 10^{-12} cm^2/s, corresponding to several 10 nm/s diffusion. The detailed concept of our proposed method for nanoscale diffusion measurements is given in ref [6].

In order to experimentally present such high sensitivity by our new method, we have started an experimental program at the tandem facility of JAEA. A low-energy (8 keV) [8]Li beam has been provided by an isotope separator on-line (ISOL) at the tandem facility. In this case, the implantation depth can be set to several tens of nm from a sample surface. The implantation depth profile after several seconds will show a significant amount of broadening as compared with the as-implanted depth profile even for nanoscale level diffusion. As the sample, we selected a 400-nm-thick Li$_2$O-V$_2$O$_5$-SiO$_2$ (LVSO) thin film. The diffusion coefficient of an LVSO sample could not be measured below 200℃ by the previous method [2].
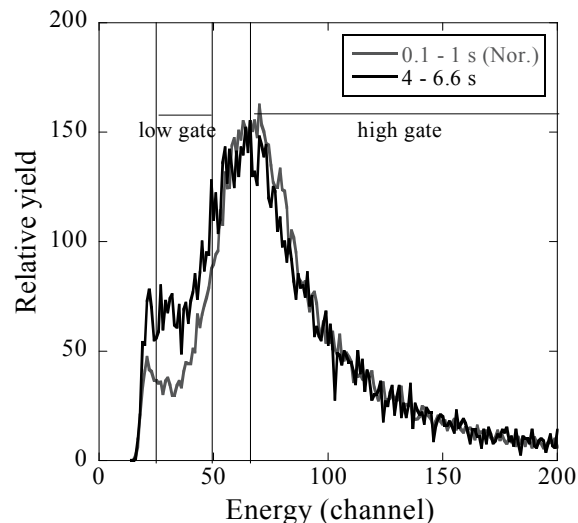
Fig. 1 Measured time-dependent energy spectra of α particles using LVSO at 130℃.

---

[1] High Energy Accelerator Research Organization (KEK)
[2] Japan Atomic Energy Agency (JAEA)
[3] RIKEN
[4]Seoul National University
[5]University of Tsukuba

Therefore, we have tried to measure the lithium diffusion coefficients at first in the thin LVSO film at the temperatures lower than 200℃. Three Si detectors were set at $\theta = 10°$ to the sample surface with the solid angle of 2×10^{-4}. The path length of the detected α particles in the sample increases by a factor of d/sin θ with respect to the depth (d) from the sample surface, thereby leading to a larger change in the measured energy spectrum for the α particles than that measured along the implantation direction. The ^{8}Li beam was periodically implanted into the sample (1.6 s for beam on and 5 s for beam off) with the intensity of about 10^5 pps.

Figure 1 shows energy spectra of α particles measured for different time durations, i.e. from 0.1 to 1 s and from 4 to 6.6 s, respectively, for LVSO thin film at 130℃. As can be seen in Fig. 2, the later energy spectrum shows an obvious shift to lower energies with an increase of time, which comes from the ^{8}Li diffusion into deeper side of the sample as discussed in ref [6].

In order to trace such temporal evolutions, we investigated the time evolution of α particle yields within appropriate energy regions, namely low gate and high gate, as shown in Fig. 1. Figure 2 shows time-dependent yields of energy-gated α particles for LVSO sample at 100℃. In order to remove the trivial time dependence of the half-life time of ^{8}Li, the yields, represented by 'Ratio' as a function of time, were normalized by those obtained measured

Fig. 2 Time-dependent yields of energy-gated α particles for LVSO film at 100℃, normalized with those for Pt sample .The results, best simulated with a diffusion coefficient of 0.92×10^{-11} cm^2/s are also shown.

using Pt foil, on which no diffusion effect was observed. As a result of the comparison of the simulation [6] as shown in Fig. 2, the diffusion coefficient was obtained as 9.2×10^{-12} cm^2/s at 100℃, demonstrating that the present method has a sensitivity to lithium diffusion coefficients down to orders of 10^{-12} cm^2/s. The detection limit for the diffusion coefficients was improved, by about two orders of magnitude, in comparison to that achieved with our previous method. For further investigations, measurements of lithium diffusion coefficients in various electrode materials of Li secondary batteries are under progress.

References
[1] S. C. Jeong, et al., Solid State Ionics 180 (2009) 626-630.
[2] S. C. Jeong, et al., AIP Conf. Proc. 1120 (2009) 197-200.
[3] H. Xia, et al., J. Power Sources 159 (2006) 1422-1427.
[4] K. Nakamura, et al., Solid State Ionics 135 (2000) 143-147.
[5] J. Sugiyama, et al., J. Phys. Soc. Jpn. 82 (2013) SA023(11 pages).
[6] H. Ishiyama, et al., Jpn. J. Appl. Phys. 52 (2013) 010205(3 pages).

6.2   Charge state distribution of tungsten ions after penetration of C-foil targets (II)

M. Imai[1], M. Sataka[2], M. Matsuda[2], S. Okayasu[2],

K. Kawatsura[3], K. Takahiro[4], K. Komaki[5], K. Nishio[2] and H. Shibata[1]

When (even single) fast heavy-ion in MeV/u energy range irradiates a solid target, a unique characteristic-features, which cannot be brought about by any other means like photon or electron impacts, take effects by accumulation of several consecutive elastic and inelastic collision processes between projectile ion and target atoms. It is known for fast heavy-ion irradiation that the electronic stopping power, caused by the inelastic processes, is larger than the atomic (elastic) stopping power by more than three orders of magnitude. As a total range of fast heavy ions is longer than 10 μm, such electronic excitation effects span from the solid surface into inside the material and those features play effective roles in material modification. Each inelastic collision process is strongly affected by energy, charge state, electronic state and so on of the projectile ions, whereas our previous measurements [1-3] using sulfur and carbon projectile ions have made it clear that the difference between collision frequency, *i.e.*, collision cross sections for K- and L-shell electron processes exert an effect on charge and electronic state evolution. Fast tungsten ions are often used for material modification. Since they still wear quite number of electrons during solid penetration, charge and electronic state evolution of the projectile and secondary ion production and transport are important aspects to understand the basics of the material modification. The present measurement is a part of our joint research project of "Basic processes of fast heavy-ion irradiation into solid and material property modification" and is devoted to the study of charge state distribution of 1.0 MeV/u W^{q+} ($q = 15-30$) projectile ions before and after the equilibrium through C-foil penetration.

As has been presented in the previous annual reports [4-11], we have measured the exit charge state distributions for penetrations of $S^{6+} - S^{16+}$ ions through C-foil targets of $0.9 - 200$ μg/cm^2 in thickness and performed calculations by an ETACHA code [12, 13] to succeed in reproducing the experimental results, although ETACHA has been designed for higher energy region (>10 MeV/u) [1-3]. In this report, results of our new measurements for tungsten projectiles are presented.

The experiments were performed at the LIR1–3 beam line of the 20UR Tandem Accelerator Facility. A beam of 1.0 MeV/u (184 MeV) $^{184}W^{13+}$ or $^{184}W^{15+}$ ions was provided from the Tandem Accelerator within an energy accuracy of 0.1%, which was sufficient to separate the W isotopes, and post-stripper C-foil of about 20 μg/cm^2 was used to produce higher charge states up to 30+. The W^{q+} ion beam was directed into self-supported carbon foils of $4.6 - 20$ μg/cm^2 in thickness. The charge states after foil penetration were measured using the heavy ion magnetic spectrometer ENMA and a position-sensitive gas chamber detector. The vacuum condition inside the collision chamber and the spectrometer were maintained below 10^{-4} and 10^{-6} Pa, respectively, to practically eliminate background charge-exchange collisions with residual gas, which was confirmed by measurements with no foils.

---

[1] Kyoto University
[2] Japan Atomic Energy Agency (JAEA)
[3] Kansai Gaidai University
[4] Kyoto Institute of Technology
[5] RIKEN

Measured charge state distributions for 1.0 MeV/u W^{15+} and W^{30+} ion incidence after penetration through 4.6, 9.9, and 20 $\mu g/cm^2$ C-foil targets are plotted in Fig. 1. The charge state distributions for W^{30+} incidence through 9.9 and 20 $\mu g/cm^2$ targets fully coincide showing that the charge-equilibrium has been established. The equilibrium mean charge state $\overline{q} = \sum_q qF(q)$ and distribution width $d = \left[\sum_q \left(q - \overline{q} \right)^2 F(q) \right]^{1/2}$, where $F(q)$ denotes the fraction for charge state q, are 31.4 and 2.30~2.31, respectively, whereas the only available data from literature [14] predicts smaller mean charge state. Mean charge states of the measured charge state distribution increase to the equilibrium value as the target thickness grows for both W^{15+} and W^{30+} incidence, but the distribution for W^{15+} incidence at 9.9 $\mu g/cm^2$ does not establish equilibrium, whose distribution width decreases to 2.28 as the target thickness grows from 4.6 $\mu g/cm^2$.
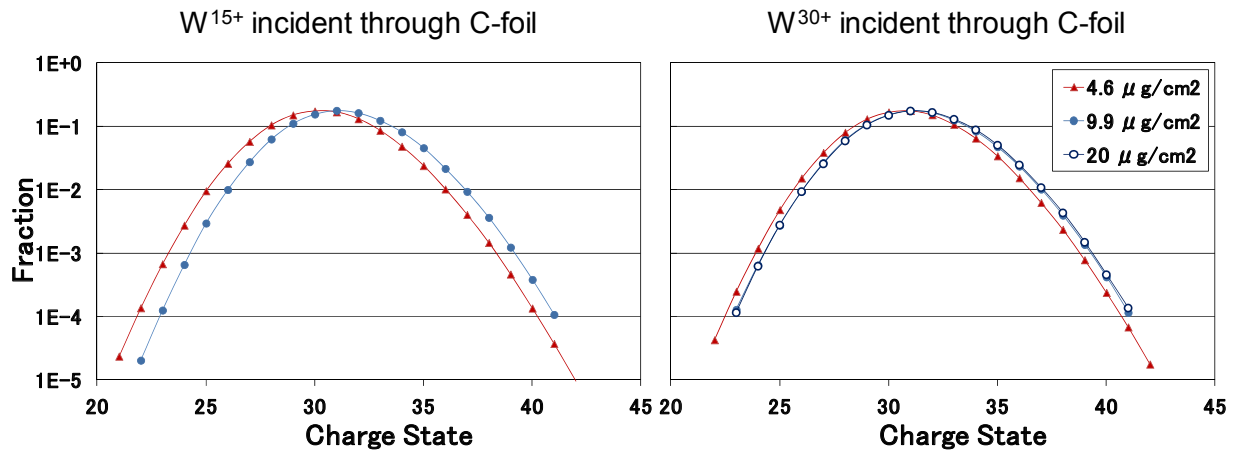
Fig. 1   Charge state distribution for 1.0 MeV/u W^{15+} and W^{30+} ion incidence after penetration through 4.6, 9.9 and 20 $\mu g/cm^2$ C-foils.

References

[1] M. Imai et al., Nucl. Instrum. Methods Phys. Res., B230 (2005) 63-67.

[2] M. Imai et al., Nucl. Instrum. Methods Phys. Res., B256 (2007) 11-15.

[3] M. Imai et al., Nucl. Instrum. Methods Phys. Res., B267 (2009) 2675-2679.

[4] M. Imai et al., JAEA-Review 2007-046 (2008) 87-88.

[5] M. Imai et al., JAEA-Review 2008-054 (2008) 89-90.

[6] M. Imai et al., JAEA-Review 2009-036 (2009) 91-92.

[7] M. Imai et al., JAEA-Review 2010-056 (2010) 89-90.

[8] M. Imai et al., JAEA-Review 2011-040 (2011) 67-68.

[9] M. Imai et al., JAEA-Review 2013-002 (2013) 49-50.

[10] M. Imai et al., JAEA-Review 2013-057 (2013) 45-46.

[11] M. Imai, JAEA-Review 2009-006 (2009) 168-180.

[12] J. P. Rozet et al., J. Phys. B22 (1989) 33-48.

[13] J. P. Rozet et al., Nucl. Instrum. Methods Phys. Res., B107 (1996) 67-70.

[14] K. Shima et al., At. Data Nucl. Data Tables 51 (1992) 173-241.

6.3   Coster Kronig electrons from excited C^{q+} ions produced in the transmission through thin carbon foils

S. Tomita[1], R. Kinoshita[1], Y. Shiina[1], K. Sasa[1], M. Sataka[1], M. Matsuda[2], M. Imai[3] and K. Kawatsura[4]

Strong reduction of secondary electron yield for fast cluster injection is one of interesting subject to study, because of strong violation of the relation, $Y_e = L\,S_e$, where Y_e is secondary electron yield, S_e is electronic stopping power, and the parameter L is material parameter [1, 2]. We think that the behavior of scattered electron produced by projectile ion inside material must be crucial to understand the special cluster effect. Zero degree electron spectroscopy is one of the well-known techniques to investigate the behavior of the electrons inside material produced by the transmission of swift ions. Especially, we focus on the Coster Kronig electrons which correspond to the number of excited states formed by capturing electrons at emergence from target material. Since the radius of excited electron become comparable with the inter atomic distance between constituent atoms of the cluster after passage of thin carbon foil, thus, the cluster effect on the formation of such excited states is interesting to measure. We plan to make comparison of the yields of Coster Kronig electrons between atomic and molecular injection case. In this report, we present the spectrum of Coster Kronig electrons from C^{q+} ions.

Experiments were conducted at the tandem accelerator of the Japan Atomic Energy Agency, Tokai. C^+ ions were produced by ECR ion source from benzene gas. The ion source was located on the high voltage terminal of the tandem accelerator. The ions were extracted by potential difference of 10 kV and injected to the normal acceleration beam line by a 90° magnet. The mass selected ions, using a 180° magnet on the high voltage terminal, were injected to the acceleration tubes. The kinetic energy of C^+ ion used for current experiment was 3.5 MeV. The accelerated ions were mass selected again by a 90° bending magnet and transported to the experimental chamber. The experimental apparatus used for the present experiment is described elsewhere in detail [3]. The ions were injected on the target of a thin carbon foil purchased from Arizona Carbon Foil Co. Inc.. The nominal thickness was 4.8 μg/cm². On the downstream of the target, 45° tandem parallel-plate spectrometer was placed at zero degrees with respect to the direction of projectile ion beam. The resolution of the spectrometer is 3.2% without the deceleration of the electrons before entrance of second analyzer.

The obtained energy spectrum for 3.5 MeV C^+ is shown in Fig.1. The electron energy refers to the projectile rest frame. Electrons emitted in forward and backward are shown together. In both spectra, the

---

[1]University of Tsukuba
[2] Japan Atomic Energy Agency (JAEA)
[3] Kyoto University
[4] Kansai Gaidai University

peak positions correspond well to each other. The discrepancy at low energies is due to field ionization which takes place at the entrance of electrostatic analyzer. The transition energies can be estimated with value of quantum defect using

$$E_{nl} = \Delta E - Q^2 Ry \Big/ (n - \eta)^2 \qquad (1)$$

where n is the principal quantum number, Q the charge number of the atomic core seen by the Rydberg electron, η, the quantum defect calculated by Theodosiou et al. [4] and Ry the Rydberg energy. The energy difference ΔE between 2s and 2p states was taken from NIST [5]. The peaks, which correspond to the Coster Kronig transition from $1s^2 2pnl$ to $1s^2 2s\varepsilon l$, are clearly observed for $n = 5, 6, 7$. The assignment of peaks around 1 and 2 eV is not clear so far, these might be contribution from $1s^2 2s2pnl$ states. The comparison with C_2^+ at the same velocity will be performed in the following experiments.
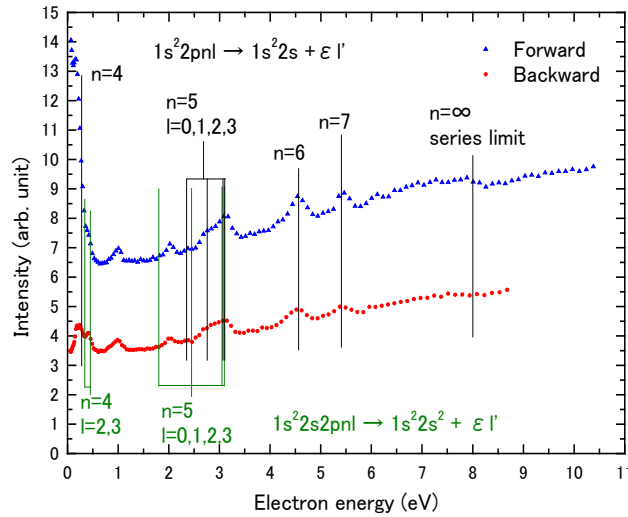
Fig. 1 Energy spectrum of zero degree electrons induced by the irradiation of 3.5 MeV C$^+$ ions through 4.8 μg/cm^2 carbon foil. The electron energy refers to the projectile rest frame. Electron emitted in forward (blue) and backward (red) are shown together. The vertical lines indicate the estimates obtained with Eq. 1 (see text).

References

[1] S. Tomita *et al.*, Phys. Rev., A 73 (2006) 060901
[2] S. Tomita *et al.*, Phys. Rev. A 82 (2010) 044901
[3] K. Kawatsura *et al.*, Nucl. Instrum. Methods Phys. Res., B 53 (1991) 421.
[4] C. E. Theodosiou, M. Inokuti, and S. T. Manson, At. Data Nucl. Data Table 35 (1986) 473.
[5] NIST Atomic Spectra Database, *http://www.nist.gov/pml/data/asd.cfm*

CHAPTER 7

Radiation Effects in Materials

This is a blank page.

7.1 Nanosphere formation of CeO$_2$ irradiated with high-energy heavy ions

N. Ishikawa[1], N. Okubo[1], T. Sonoda[2], T. Sawabe[2] and M. Sasase[3]

When an oxide is irradiated with ions with high-energy heavy ions, modified columnar area called ion-tracks are often created. Inside the ion-track, the crystalline structure is modified or the density is different from the matrix. Because of these features, ion-tracks can be visualized by a transmission electron microscope (TEM).

It is already known that in CeO$_2$ irradiated with high-energy heavy ions ion-tracks are formed. According to the previous literatures[1,2], the ion-track in ion-irradiated CeO$_2$ is not amorphized and its crystal structure is maintained but somehow modified from the original lattice structure. There have been many studies that suggest oxygen is deficient inside the ion-track[3,4]. Recently, it has been found by the high-resolution TEM study that the signal intensity of the Ce cation column is reduced[5]. It is important to know how and where Ce and O atoms are displaced, because it is closely related to the ion-track formation mechanism. One of the methods to elucidate the mechanism is to investigate the surface swelling, because it is probably related to the cooling process of the transiently excited hot atoms inside the ion-tracks. Unfortunately, there is no literature concerning the surface morphology as long as ion-irradiated CeO$_2$ is concerned. In this paper, we report for the first time that in ion-irradiated CeO$_2$ nanospheres are formed at the surface of CeO$_2$ sample.

The samples for TEM were picked up from sintered polycrystalline CeO$_2$ and thinned by focused ion beam (FIB) method. They were irradiated with 200 MeV Au at room temperature. One of the samples is irradiated from the direction normal to the sample surface. Figure 1 shows the bright field images of ion-irradiated CeO$_2$ which was irradiated from the direction normal to sample surface and was tilted in the microscope. The ion-tracks can be imaged with off-focus condition, while they cannot be imaged clearly by bright field image mode with focused condition. The image of ion-tracks becoming black or white depends on whether the observation condition is over-focus or under-focus. At both ends of the ion-tracks, circular contrasts are observed. Their size is larger than the width of the ion-tracks.

In order to clarify whether the circular contrasts are actually spherical objects, another sample was irradiated from inclined direction (45 degree) relative to the sample surface. Figure 2 shows the objects observed at the crack faces of ion-irradiated CeO$_2$ are mostly spherical. Ion-tracks are also observed, and nanospheres are found at the end of the ion-tracks. They are observed at both crack faces indicating that nanospheres are created not only at the irradiated front face but also at the rear face where ions exit. Nanosphere formation has never been taken into consideration when, for example, molecular dynamics simulation of ion-track formation process has been performed. Formation of nanospheres may be an

---

[1] Japan Atomic Energy Agency (JAEA)
[2] Central Research Institute of Electric Power Industries (CRIEPI)
[3] The Wakasa Wan Energy Research Center (WERC)

important clue to elucidate the thermal history of the local region near ion-tracks.
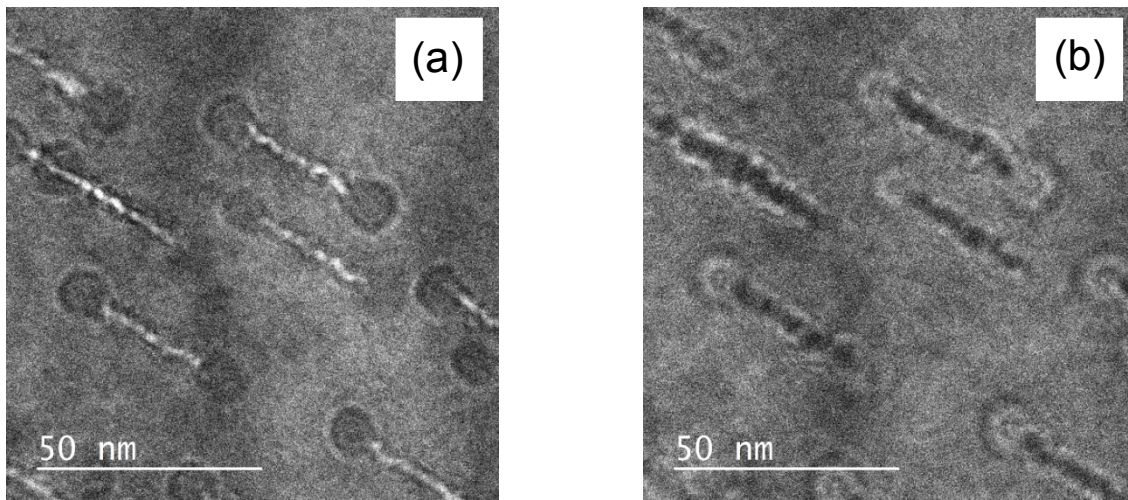
Fig. 1 Bright field image of ion-tracks for CeO$_2$ irradiated with 200 MeV Au. The sample is tilted in the microscope. (a) The image is taken in under-focus condition.(b) The image is taken in over-focus condition.
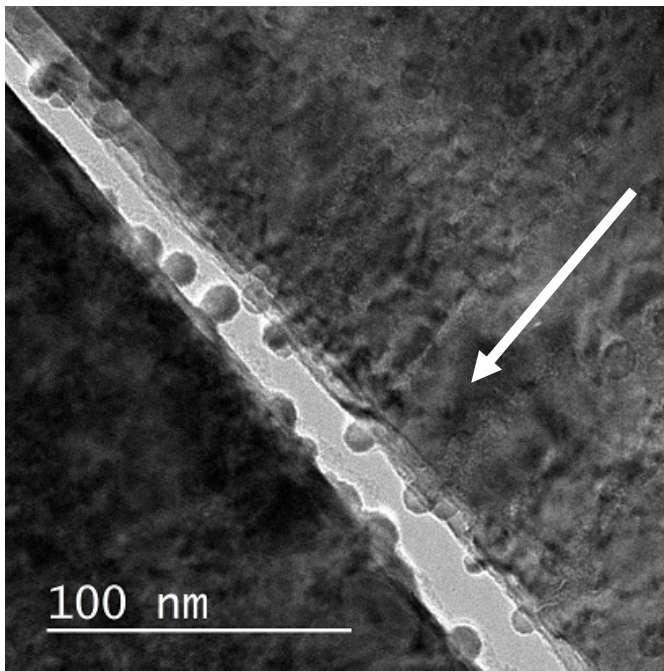
Fig. 2 Bright field image of nanospheres created at the crack faces of irradiated CeO$_2$. The sample was irradiated from the inclined direction of 45 degrees. The white arrow indicates the direction parallel to the observed ion-tracks.

References

[1] T. Sonoda et al., Nucl. Instrum. Methods Phys. Res., B 250 (2006) 254- 258.

[2] K. Yasuda et al., Nucl. Instrum. Methods Phys. Res., B 314 (2013) 185-190.

[3] K. Ohhara et al., Nucl. Instrum. Methods Phys. Res., B267 (2009) 973-975.

[4] H. Ohno et al., Nucl. Instrum. Methods Phys. Res., B 266 (2008) 3013-3017.

[5] S. Takaki et al., Nucl. Instrum. Methods Phys. Res., B 326 (2014) 140‑144.

7.2 Ion track structure in CeO$_2$ irradiated with swift heavy ions

S. Takaki[1], K. Yasuda[1], S. Matsumura[1], N. Ishikawa[2] and M. Matsuda[2]

Irradiation by fission products (FPs) induces most crucial radiation damage in nuclear fuel and transmutation target materials. High-density electronic excitation caused by FPs is known to form continuous ion tracks in oxide ceramics. High-resolution scanning transmission electron microscopy (STEM) observation of ion tracks formed in CeO$_2$ under 200 MeV Xe ion irradiation has indicated that the atomic density at the core region of ion tracks is decreased, and that the oxygen sublattice at the core damage region of ion tracks is significantly disordered [1]. This report aims to clarify the effect of electronic stopping power, S_e, on the structure of ion tracks in CeO$_2$. Swift heavy ions were irradiated to CeO$_2$ with energies ranging from 70 to 340 MeV and transmission electron microscopy (TEM) was applied to the irradiated specimens.

Polycrystalline CeO$_2$ specimens were fabricated by sintering in air and those specimens were irradiated with swift heavy ions to energies ranging from 70 to 340 MeV at an ambient temperature at the Tandem accelerator facility in JAEA-Tokai. The electronic stopping power (S_e) of 70 MeV Xe, 100 MeV Kr, 200 MeV Xe and 340 MeV Au ions at surface region of CeO$_2$ specimen was calculated by SRIM code to be 17, 19, 27 and 39 keV/nm, respectively. Irradiated specimens were prepared to be thin-foils by using Ar-ion milling for plan-view observations. Microstructure observations were performed with bright-field (BF) and weak-beam dark-field (WBDF) TEM imaging technique at accelerating voltage 200 kV.

Figure 1 shows BF plane-view images in CeO$_2$ irradiated with 100 MeV Kr ions to a fluence of 1×10^{14} ions/cm^2, taken with different focus conditions, which illustrates damage regions of ion tracks. Distinct white dot-contrast with about 2 nm in diameter is observed with an under-focus condition (Fig. 1(d)), whereas those regions were observed as black dot-contrast with over-focus conditions (Fig. 1(b), (c)). Such reverse of contrast dependent on the focus conditions indicates that the damage regions are observed as Fresnel-contrast. The cause of Fresnel contrast is attributed to the decrease in the atomic density at the core damage region [1]. The areal density of this Fresnel-contrast was evaluated to be 1×10^{12} / cm^2, which is about 2.5 times larger than the areal density of ion tracks in CeO$_2$ irradiated with 210 MeV Xe ions to the same fluence of 1×10^{14} ions/cm^2 [2]. The higher saturated areal density of 100 MeV Kr ions at high fluence suggests that the influence region induced by an incident ion is smaller than the one caused by 210 MeV Xe ions.

Figure 2(a) shows an inclined view of WBDF image in CeO$_2$ irradiated with 100 MeV Kr ions to a fluence of 1×10^{14} ions/cm^2, which illustrates ion tracks as a continuous bar contrast along the path of penetrating ions. Effective thickness excitation contour of the matrix is also seen in Fig. 2 (a). Fig. 2 (b) is the magnified image of the indicated region in Fig. 2 (a). These contrast of ion tracks in Fig. 2 (b) is observed

---

[1] Kyushu University
[2] Japan Atomic Energy Agency (JAEA)

rather vaguely compared to the ones observed in CeO$_2$ irradiated with 200 MeV Xe ions [1]. This result as well as the different saturation density between 100 MeV Kr and 200 MeV Xe ions suggest that the structure of the core damage region of ion tracks is different between these irradiation conditions.

a. just focus   b. +0.5 μm   c. +2.0 μm   d. -0.5 μm
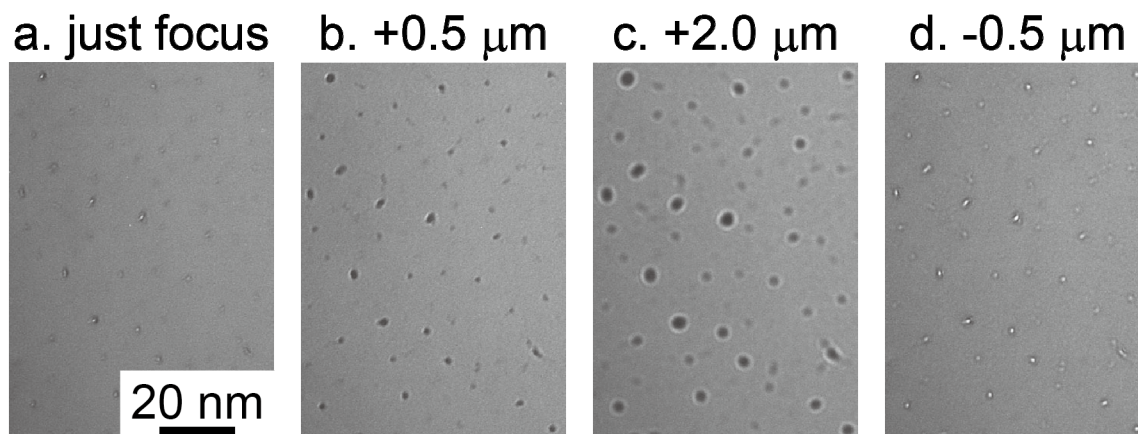
Figure 1 BF plan-view images obtained from core damage region ion tracks in CeO$_2$ irradiated with 100 MeV Kr ions to a fluence of 1×10^{14} ions/cm^2, taken in different focus conditions.
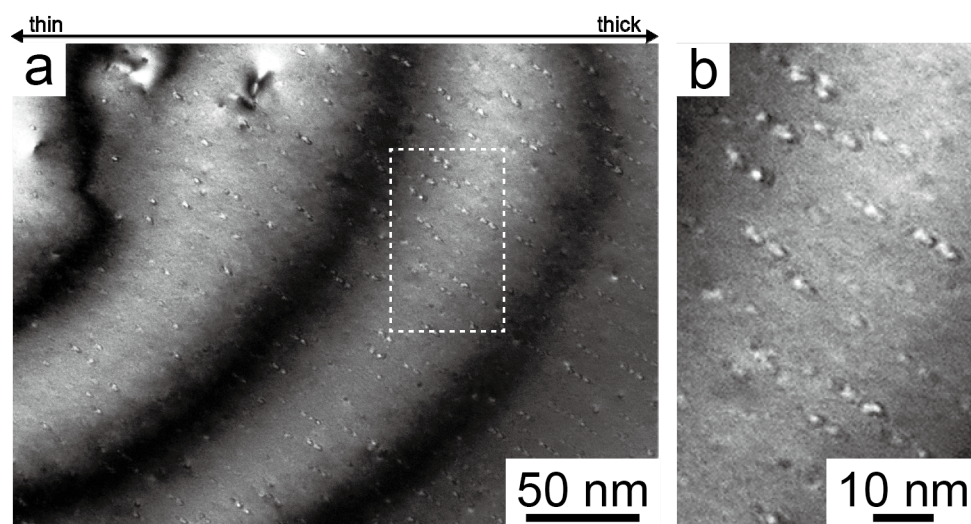
Figure 2 Weak-beam (g,5g), g = 111 dark-field image of CeO$_2$ irradiated with 100 MeV Xe ions to a fluence of 1×10^{14} ions/cm^2 (a). A magnified image of an area surrounded by a dashed line in Fig. 3(a) is shown in (b).

References

[1] S.Takaki et al., Nucl. Instrum. Methods Phys. Res., B 326 (2014) 140.

[2] K.Yasuda et al., Nucl. Instrum. Methods Phys. Res., B 314 (2013) 185.

7.3   Shape and property control of metal nanoparticles
by swift heavy ion irradiation

H. Amekura[1], N. Okubo[2] and N. Ishikawa[2]

When spherical nanoparticles (NPs) embedded in silica glass (SiO$_2$) are irradiated with swift heavy ions (SHI), elongation of the NPs, i.e., the deformation from spheres to rods along the ion beam direction, is induced [1]. This phenomenon has been confirmed in various metal NPs, including Au, Ag, Pt, Co, Zn, etc., as well as an ordered alloy of FePt, and a solid solution of Au$_{1-x}$Ag$_x$. However, the elongation of non-metallic NPs has been limited to Ge NPs.   In this study, we evaluated the effects of SHI irradiation to ZnO NPs, i.e., another species of non-metallic NPs. Shape elongation of NPs was detected by optical linear dichroism (OLD) spectroscopy and cross-sectional transmission microscopy (XTEM). However, the elongated NPs coexisted with non-elongated larger ZnO NPs. Electron energy loss spectroscopy with scanning TEM (STEM-EELS) revealed that the elongated NPs consisted of Zn metal rather than ZnO. The SHI irradiation induced the reduction of ZnO NPs to Zn NPs, and following elongation of the reduced Zn NPs.

ZnO NPs were prepared by Zn ion implantation, followed by thermal oxidation [2]. A silica glass was implanted with Zn ions of 60 keV to a fluence of 1.0×10^{17} ions/cm^2. The implanted samples were thermally oxidized at 700°C for 1 h in flowing oxygen gas. This process induced the formation of the two-layer structure of ZnO NPs, i.e., larger NPs on the surface and smaller NPs embedded in SiO$_2$ [2]. The surface ZnO NPs were covered with a SiO$_2$ layer of 300 nm thick by chemical vapor deposition (CVD) at 350°C. The samples with embedded ZnO NPs were irradiated with 200MeV Xe^{14+} ions by using the Tandem accelerator at the Japan Atomic Energy Agency's Tokai Research and Development Center (JAEA, Tokai). The SHI fluence ranged from 1.0×10^{11} to 5.0×10^{13} ions/cm^2. The samples were irradiated with an incident angle of 45° from the surface normal.

Figure 1(a) and (b) show XTEM images from a sample irradiated to 5.0×10^{13} ions/cm^2. The larger NPs with dome-like shapes located at the upper center of Fig. 1(a) were originally the surface ZnO NPs. The original substrate surface before CVD is clearly visible as a black horizontal line around the center of Fig. 1(a). Elongated NPs were observed approximately 50 nm deeper than the original substrate surface, where smaller embedded ZnO NPs once existed before the irradiation. The major axes of the elongated NPs pointed in the same direction, i.e., in the incident direction of the SHI beam at 45° from the surface normal. A high-resolution TEM image of an elongated NP is shown in Fig. 1(b). The observed lattice fringes of a period of 0.495 nm could not be ascribed to any ZnO diffractions but to Zn (001) diffraction.

To judge more clearly whether the elongated NPs consisted of ZnO or of Zn, we performed a composition

---

[1] National Institute for Materials Science (NIMS)
[2] Japan Atomic Energy Agency (JAEA)

analysis using STEM-EELS. Figure 2(a) is a high-angle annular dark-field (HAADF) image of the area around an elongated NP indicated by "1". Figure 2(b) shows the element compositions (Zn, Si, and O) detected by STEM-EELS along the line shown in Fig. 2(a). The Zn peaks appearing at positions $x \sim 14$ and 48 nm correspond to a nearly spherical NP and the elongated one, respectively. From the concentration profiles of Zn, Si, and O shown in Fig. 2(b), the profile of a metallic Zn element was determined (Fig. 2(c)), under the assumption of stoichiometric ZnO and SiO_2. The result showed that the elongated NP at $x \sim 48$ nm and the nearly spherical NP at ~14 nm consisted of Zn metal and ZnO, respectively.

Certain portions of ZnO NPs were reduced to metallic Zn NPs by SHI irradiation. Further irradiation induced elongation of the reduced NPs which were larger than the threshold size.
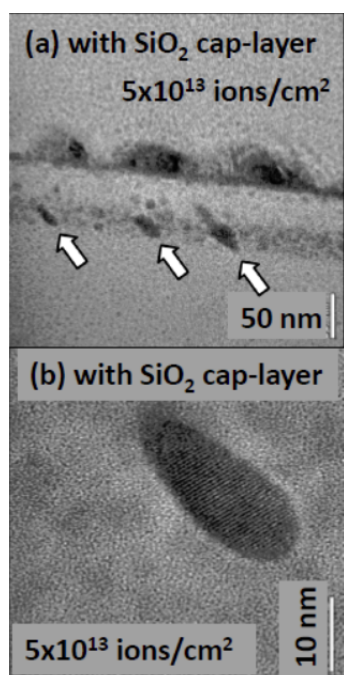
Fig. 1. Bright-field XTEM images of ZnO NPs embedded in SiO_2 irradiated with 200 MeV Xe^{14+} ions to 5.0×10^{13} ions/cm^2. In (a), NPs elongated with the irradiation are shown by arrows. Image (b) shows a magnified image of an elongated NP.
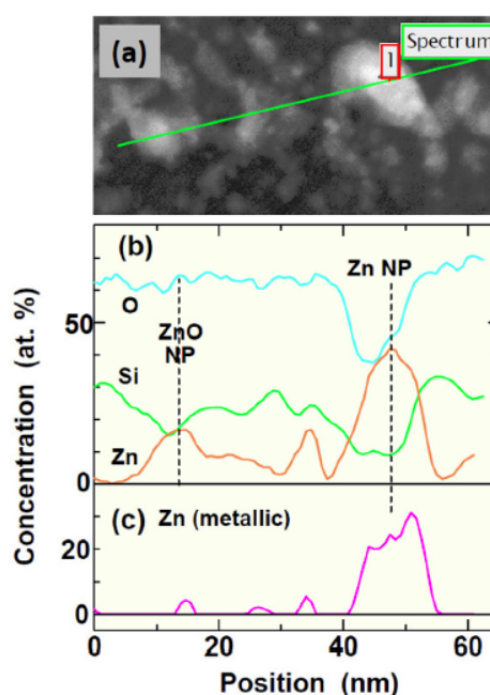
Fig. 2. (a) HAADF image of an elongated NP (indicated by "1") observed in a sample irradiated with 200 MeV Xe^{14+} ions to 5.0×10^{13} ions/cm^2. (b) Elemental distributions of Zn, Si, and O along the line shown in (a) across the NP, as detected by STEM-EELS. (c) Distribution of metallic Zn, as determined under the assumption of stoichiometric ZnO and SiO_2.

References

[1] C. D'Orléans et al., Phys. Rev. B 67 (2003) 220101.

[2] H. Amekura and N. Kishimoto, in "Lecture Notes in Nanoscale Science and Technology" Vol. 5, edited by Z. Wang (Springer, New York, 2009) 1−75.

7.4   Ion irradiation effects on WN films

N. Matsunami[1], T. Teramoto[1], S. Okayasu[2], M. Sataka[2] and H. Kakiuchida[3]

The authors have investigated electronic excitation effects on the electrical resistivity, optical absorption and atomic structure of oxides [1] and nitrides such as Cu_3N [2]. There are a few studies of electronic excitation effects on nitrides. We have studied modifications of WN by high-energy ions for better understanding of the effects on nitrides.

WN films were prepared by using a RF-magnetron sputter deposition method on C-plane-cut-Al_2O_3-substrates at 425 ºC with W target (99.95 % purity) and N_2 gas. Substrate temperature was optimized so that the X-ray diffraction (XRD) intensity takes its maximum. The composition and film thickness were evaluated by means of Rutherford backscattering spectroscopy (RBS) of 1.8 MeV He^+ ions with tables of stopping powers [3]. It appears that unwanted oxygen is incorporated in films and the composition of WN_xO_y films is obtained to be x=1.1±0.1 and y=0.4±0.1. Presence of oxygen in films was confirmed by energy dispersive X-ray (EDX) measurements. XRD with Cu-K_α shows a strong peak at the diffraction angle of 2θ≈37 º and a weak peak at 2θ≈79 º (Fig. 1) and these peaks are assigned as hexagonal WN, referring to JCPDS card data [4]. No peaks were observed other than WN and Al_2O_3. The lattice parameters of (a- and c-axes) of as deposited films are smaller by 3 % and 0.5 % than the values in [4]. It is speculated that smaller lattice parameter is partly due to oxygen inclusion. The peak at 2θ≈37 º, (100) diffraction, is concerned hereafter. For RBS, we employ the W density of N_W=5.2x10^{22} cm^{-3}, evaluated from the lattice parameters determined by XRD (0.2435 nm (a-axis) and 0.2815 nm (c-axis)), the composition being taken to be $WNO_{0.4}$. Thickness of films used in the present study is ~ 50 nm. The resistivity was measured by four-terminal method and the resistivity of unirradiated film increases with decreasing the temperature from 25 to -250 ºC like semiconductor. Ion irradiation was performed at room temperature.

For 100 MeV Xe ion impact on WN_xO_y film, it is found that at the ion fluence of 0.3x10^{12} cm^{-2}, the XRD intensity decreases to a half of that before the ion irradiation and to 1/50 at 3.7x10^{13} cm^{-2} (Fig. 1, upper XRD pattern). It also appears that the a-axis lattice parameter increases with increasing the ion fluence, reaching the maximum lattice expansion of 1.4 % at 0.7x10^{12} cm^{-2} and turns to lattice compaction by 0.5 % for further irradiation (fluence > 2x10^{12} cm^{-2}). For lower fluence (<10^{12} cm^{-2}), lattice expansion is partly due to lattice relaxation by ion irradiation. Influence of the atomic structure modification on the electrical resistivity will be discussed later. A tiny diffraction peak at 2θ≈64.5 º (Fig. 1, upper XRD) is not due to W neither WO_3, not identified at present. The optical absorbance monotonically decreases with the optical wavelength (200 to 2500 nm), indicating that the bandgap does not exist in the region of 0.4 − 6 eV. No appreciable change was observed in the optical absorption by ion irradiation and neither observed in change of the composition under ion irradiation.

---

[1] Graduate School of Engineering, Nagoya University

[2] Japan Atomic Energy Agency (JAEA)

[3] National Institute of Advanced Industrial Science and Technology (AIST)

The electrical resistance of unirradiated WN_xO_y film is 12 kΩ (0.031 Ωcm), and it is found that the resistance decreases by ion irradiation as shown in Fig. 2, also that the resistivity is nearly independent of the film thickness, indicating insignificant contribution of surface effects. The resistance steeply decreases by more than an order of magnitude for the ion fluence ~ 10^{12} cm^{-2} (as described above, the lattice turns to compaction at this fluence) and gradually decreases for further ion irradiation. The lowest resistance achieved in this study is 150Ω (3.8x10^{-4} Ωcm). Similarly, an order of magnitude reduction of the resistivity was observed for 100 keV N ion irradiation at ~ 10^{16} cm^{-2}. These results indicate that the electronic excitation plays an important role in the resistivity modification of WN_xO_y film, since the fluence necessary for the resistivity modification for 100 MeV Xe ion is smaller by three order of magnitude than for 100 keV N ion irradiation, and the electronic stopping power is larger by the same amount for 100 MeV Xe ion, while the nuclear stopping power is comparable for both ions (Table 1). The resistivity reduction (a factor of 80) is much smaller than the case of Cu_3N (eight order of magnitude) [2].

Table 1 Projected range (R_p), electronic (S_e) and nuclear (S_n) stopping powers near surface of $WNO_{0.4}$ for 100 MeV ^{136}Xe and 100 keV N ions in calculated using TRIM1997 [3].

Ions	$R_p(\mu m)$	$S_e(keV/nm)$	$S_n(keV/nm)$
100 MeV Xe	4.8	38.9	0.45
100 keV N	0.065	0.59	0.16
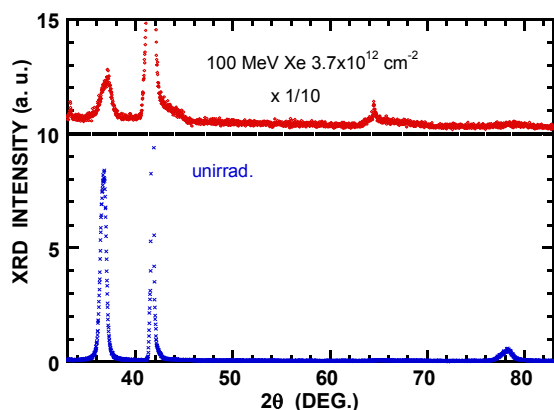
Fig. 1 XRD patterns of WN_xO_y as deposited film (lower pattern) and after 100 MeV Xe ion irradiation at 5.3x10^{12} cm^{-2} (upper pattern). Peaks at 2θ≈37 ° and ≈78 ° are diffraction of (100) and (102) of hexagonal WN, and 41.7 ° c-Al_2O_3 (006).
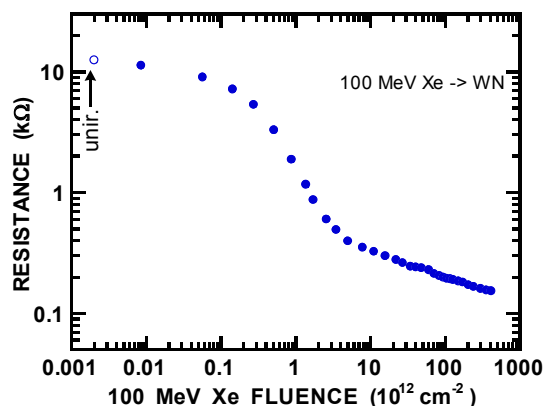
Fig. 2 Resistance of a WN_xO_y film vs fluence of 100 MeV Xe ions (●).

References

[1] N. Matsunami et al., Nucl. Instrum. Methods Phys. Res., B314(2013)55.

[2] N. Matsunami et al., Nucl. Instrum. Methods Phys Res., B267(2009)2653.

[3] J. F. Ziegler, J. P. Biersack, U. Littmark, The Stopping and Range of Ions in Solids, Pergamon Press, 1985.

[4] JCPDS card number 251256.

7.5　High energy ion induced electrical degradation of thin SiC

N. Okubo[1], T. Nozawa[1], K. Ozawa[1] and N. Ishikawa[1]

In this report, to understand the effects of high energy primary knock-on atom (PKA) introduced by high-energy fusion neutron irradiation, the electrical conductivity change by high energy ion irradiation is evaluated. Radiation induced electrical degradation (RIED) of SiC was measured in the enough thin specimens after high energy heavy ion irradiation. Functional ceramics including Al_2O_3 and SiC are attractive materials for a fusion demonstration power reactor (DEMO). Toward DEMO applications, changes of the electrical conductivity of the ceramics under irradiation must be serious problems, as well as other possible detrimental effects on the microstructure of the ceramic materials due to displacement damage, since these properties are affected by irradiation, depending on temperature and dose rate. Electrical resistivity measurements have been conducted using some irradiation sources such as a fusion neutron source (FNS) and a research reactor (JRR-3) [1, 2]. Measurements with fission neutron irradiation have been also conducted [3–5]. However, the damage levels and the PKA energy available for FNS and JRR-3 are limited and insufficient for the DEMO design. In this report, to understand the effects of high energy PKAs introduced by high-energy fusion neutron irradiation, the electrical conductivity change by high energy ion irradiation is evaluated.

The specimen configuration and the electric circuit for electrical conductivity measurement were applied from Ref. [2] to high energy ion irradiation. Irradiation of 160 MeV Xe ions was conducted at the central part of thin specimen. The projectile range of the ions was about 10 μm. To suppress the effect of leak current at the specimen surface sensitive to surface electron migration and carbon contamination during irradiation, the specimen with a guard ring is often applied to measure the electrical conductivity of ceramics. Irradiation area was selected by specimen mask to cover only the center electrode and monitored by both currents of center and guard ring. The thickness of the specimen was 50 μm in this period (2013). The thickness might be lower limit because of bonding the Au wire and also handling without break. Irradiation with high-energy Xe ions has been already verified to produce surface amorphous layer, which was caused by accumulation of ion tracks around surface region in single crystal Al_2O_3 by intense electron excitation [6]; therefore, 160 MeV Xe ions were used even for SiC. Preliminary irradiation results showed that I-V characteristics were not ohmic correlation and included defect recovering for as received thin specimens with Pt/Ti electrodes. Then, thermal annealing at 800℃ for 30 min was conducted under 1.0×10^{-3} Pa before irradiation to remove defects in the sputtered films of Pt and Ti.

Figure 1 shows correlation between the measured currents and the applied voltages (current-voltage characteristics) for sintered α-SiC before and after irradiation at ambient temperature. The ion dose rate and total dose was about 4×10^9 ions/cm²s and 7×10^{13} ions/cm², respectively. The electrical conductivity was calculated for ohmic voltage region about 1 V. The conductivity was 4.86×10^{-3} S/m for before irradiation

---

[1]　Japan Atomic Energy Agency(JAEA)

and degraded to be 2.84×10^{-3} S/m after the irradiation. In previous reports, we showed the I-V correlation after irradiation for thick specimens of 200 μm. There was almost no degradation unlikely in this case even for high dose irradiation of 2×10^{14} ions/cm^2. It suggests that the thickness of 50 μm is better for estimation of RIED, because the order of thickness is comparable with the ion projectile range ～10 μm, under which depth the layer is modified by high PKA energy.

The next step is to measure the electrical conductivity under the irradiation by using the enough thinned specimen. Then, the electrical conductivity affected by high-energy PKA is expected to be obtained by in-situ measurement during irradiation. Irradiation with ion energies ranging one to ten times as high as that of the maximum PKA energy produced by fusion neutron irradiation will be conducted focusing on the significance of irradiation-induced microstructural change by intense electron excitation of the materials. The surface morphology and microstructural evaluation of irradiated specimen will be conducted.
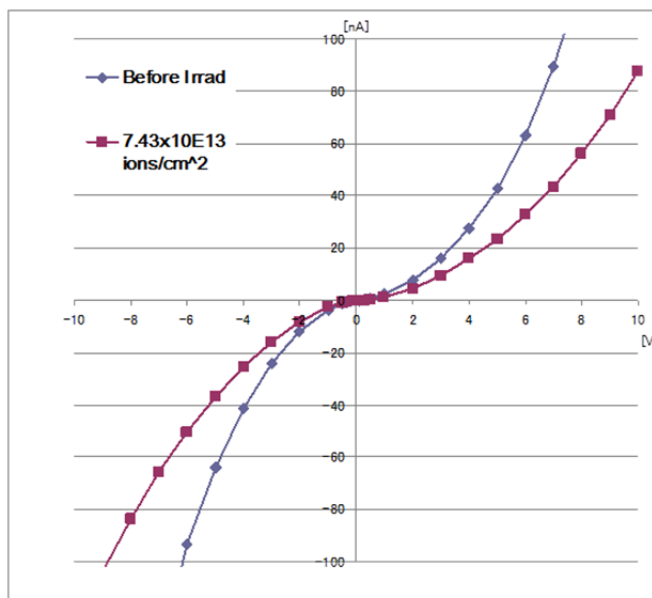
Fig. 1 Correlation between the measured current and the applied voltage for α-SiC before, and after ion irradiation at ambient temperature.

References

[1] K. Noda et al., Fusion Eng. Des. 29 (1995) 448.

[2] T. Tanifuji et al., J. Nucl. Mater. 253 (1998) 156.

[3] T. Shikama et al., Ceramics in Nuclear and Alternative Energy Applications, The American Ceramics Society, (2006) 145-156.

[4] T. Shikama, B. Tsuchiya, E.R. Hodgson, J. Nucl. Mater. 367-370 (2007) 995.

[5] B. Tsuchiya et al., J. Nucl. Mater. 367-370 (2007) 1073.

[6] N. Okubo, N. Ishikawa and S. Jitsukawa, Nucl. Instum. Methos Phys. Res., B314 (2013) 208-210.

7.6   Flux pinning properties for $B \parallel c$-axis and $B \parallel ab$-plane in high-T_c superconductors with splayed columnar defects

T. Sueyoshi[1], Y. Furuki[1], T. Kai[1], T. Fujiyoshi[1] and N. Ishikawa[2]

In high-T_c superconductors, one-dimensional (1D) pinning centers (PCs), which are line-like defects such as dislocations and columnar defects (CDs), are most effective to immobilize flux lines even at a high temperature and a high magnetic field. One feature of the 1D PCs is to exhibit the preferential direction for the flux pinning. To take advantage of this feature, the introduction of the 1D PCs in multiple directions is thought of as a simple way to make the crtical current density J_c fairly isotropic over a wide range of magnetic field orientations. As for flux pinning by direction-dispersed (splayed) 1D PCs, it was theoretically predicted that the flux pinning can be further improved at the mid direction of the dispersion (usually at the c-axis direction) when the dispersion in 1D PC directions is slight [1]. This splay effect has been experimentally examined, especially for a bimodal splay configuration consisting of two parallel CD families at crossing angles θ_i relative to the c-axis [2]. To our knowledge, however, these experiments have been aimed at the enhancement in the J_c for $B \parallel c$-axis for the most part; unexpectedly, the influence of the splayed 1D PCs on the flux pinning at another direction has not been well studied so far. In this work, we investigate in detail the flux pinning properties of splayed CDs not only around $B \parallel c$-axis but also around $B \parallel ab$-plane for GdBCO coated conductors with CDs crossing at smaller angles produced by heavy-ion irradiations.

The samples were cut from a 5 mm-width tape of a PLD-processed GdBCO-coated conductor deposited on an IBAD substrate (Fujikura Ltd.). The thickness of superconducting layer was 2.2 μm. The superconducting layer was patterned in bridge geometry with about 40 μm width and 1 mm length. After that, the samples were irradiated with 270 MeV Xe ions at the tandem accelerator of JAEA in Tokai, Japan. To install the crossed CDs, the incident ion beam was always directed perpendicular to the bridge of sample and was tilted off the c-axis by θ_i in a range from ±15° to ±75°. It is noted that crossed CDs with $\theta_i = \pm60°$ or ±75° relative to c-axis correspond to two parallel families of CDs crossing at ±30° or ±15° relative to the ab-plane, in other words. In all samples, the total fluence is 2.0×10^{11} ions/cm^2 and the samples were irradiated to half the fluence for each irradiation direction. The transport properties were measured using a four-probe method in evaluating the J_c properties. The transport current was always applied in the direction perpendicular to the magnetic field.

Figure 1 shows the angular dependence of J_c at 77.3 K and 4 T for the irradiated samples, where θ is the angle between the magnetic field and the c-axis of GdBCO coated conductors. For $\theta_i = \pm15°$ and ±75°, a single peak remarkably emerges around $B \parallel c$-axis ($\theta = 0°$), which originates from the introduced CDs crossing around the c-axis. As the crossing angle becomes narrow, the height of the peak around $\theta = 0°$

---

[1] Kumamoto University
[2] Japan Atomic Energy Agency (JAEA)

increases and the width of the peak sharpens. These phenomena would be ascribed to the splay effect, in which the motion of flux lines from one CD to another is suppressed by the slight dispersion in the direction of CDs [1]. For $\theta_i = \pm60°$ and $\pm75°$, on the other hand, the introduced CDs produce not a single peak at the mid direction of two irradiation angles $\pm\theta_i$ but two sharp ones just at $\pm\theta_i$ in the $J_c(\theta)$ properties. Note that the value of J_c rapidly declines as the direction of magnetic field approach $\theta = 90°$, so that a dip structure occurs instead of a peak one. At $\theta = 90°$, the $J_c(\theta)$ curve barely have convex curvature and the value of J_c increases with narrowing the crossing angles of CDs. Thus, the CDs in each direction seem to work independently of one another for $\theta_i = \pm60°$ and $\pm75°$, though two parallel families of CDs crossing at $\pm15°$ or $\pm30°$ relative to c-axis cooperate and work as correlated PCs along the c-axis. In general, stacking faults and intrinsic PCs are well-known to be correlated PCs at $B \parallel ab$-plane [3]. By contrast, the CDs crossing at small angles relative to the ab-plane seem to contribute to the flux pinning at $B \parallel ab$-plane somewhat, but not to induce the splay effect at $B \parallel ab$-plane. The reason why the crossed CDs do not work as the correlated PCs along the ab-plane is unknown at present. One possible reason for this phenomenon is that the flux pinning regime is different between flux line states for $B \parallel c$-axis and $B \parallel ab$-plane. In high-T_c superconductors, the Josephson-vortex is created when the magnetic field is applied parallel to the ab-plane [4]. The structure of the Josephson vortex, which does not have a normal core and is a ellipse-like shape, is different from that of the flux lines for $B \parallel c$-axis, so different behaviours from the case of $B \parallel c$-axis are expected in the Josephson-vortex system [5]. When a magnetic field is tilted away from c-axis, flux lines are not merely tilted but a crossing lattices state, where flux lines along c-axis and Josephson vortices along ab-plane coexists, is predicted in theory [4] and confirmed in experiments [6]. Thus, the flux lines might not be localized and entangled on tilted CDs for $B \parallel ab$-plane, in contrast to the case of $B \parallel c$-axis.
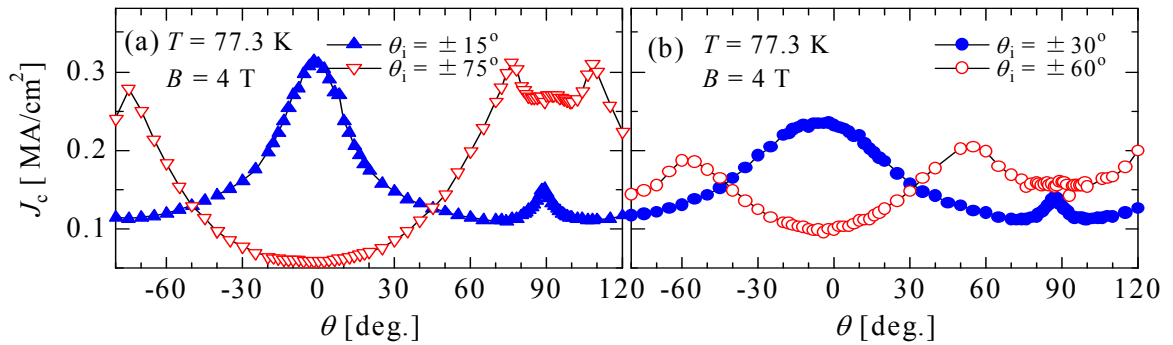
Fig. 1 Angular dependence of J_c at 77.3 K and 4 T in GdBCO coated conductors with columnar defects crossing at various angles.

References

[1] T. Hwa et al., Phys. Rev. Lett. 71 (1993) 3545.

[2] L. Krusin-Elbaum et al., Phys. Rev. Lett. 76 (1996) 2563.

[3] L. Civale et al., IEEE Trans. Appl. Supercond. 15 (2005) 2808.

[4] A.E. Koshelev, Phys. Rev. Lett. 83 (1999) 187.

[5] S. Haraguchi, T. Naito, H. Iwasaki, J. Phys. Soc. Jpn. 74 (2005) 3365.

[6] A. Grigorenko et al., Nature 414 (2001) 728.

7.7　Ion energy dependence of ferromagnetism induced by energetic ion irradiation in CeO$_2$

T. Kishino[1], N. Ishikawa[2] , Y. Saitoh[2] and A. Iwase[1]

We irradiated CeO$_2$ sintered pellets with 200MeV Xe and 10MeV iodine ions. Effects of the irradiation on their magnetic properties and lattice structure were estimated by using a SQUID magnetometer, x-ray diffraction (XRD) and x-ray absorption spectroscopy (EXAFS). In addition to the irradiation experiments, we studied the effect of oxygen vacancies, which was induced by high temperature annealing in a vacuum, on the magnetic property of CeO$_2$. In this report, we show the appearance of ferromagnetism in CeO$_2$ pellets by the energetic heavy ion irradiation or vacuum annealing. Then, we discuss the origin of ion irradiation induced ferromagnetism[1].

Specimens used in the present study were pure CeO$_2$ bulk pellets which were prepared by a conventional ceramic process. They were irradiated with 200MeV Xe ions and 10MeV I ions at room temperature. The lattice structure of the specimens was characterized using a conventional Cu-Kα x-ray diffraction (XRD). The magnetization-external magnetic field (M-H) curves were measured at 300K using a SQUID magnetometer. To analyze the short range order of the atomic arrangement around Ce atoms, we performed the EXAFS (extended x-ray absorption fine structure) measurement at the beamline 27B of High Energy Accelerator Organization (KEK). Some CeO$_2$ specimens were not irradiated but were annealed at 1273 K for 1 hour in a vacuum of 1.0×10^{-4}Pa. We measured the XRD spectra and the M-H curves also for the annealed specimens.

Figure 1 shows the ion-fluence dependence of the magnetic moments per unit area of CeO$_2$ specimen for the two ion irradiations. We have to note here that the unit of the ordinate axis is emu/cm^2 and not emu/cm^3. The magnetic moment for 10MeV I irradiation is much smaller than that for 200MeV Xe irradiation even at the same ion fluence. As the energy deposition into CeO$_2$ target through the electronic excitation process is much larger for 200MeV Xe ions than that for 10 MeV I ions, the experimental result suggests that the electronic excitation process induces the ferromagnetic state in CeO$_2$.

The XRD measurement shows that the lattice parameter increases with increasing ion-fluence. The EXAFS spectra show that the coordination number of oxygen atoms around Ce atoms decreases by the ion irradiation. Moreover, according to the result of our recent molecular dynamics (MD) simulation for the effect of "ultra-high lattice temperature" along the ion beam path in CeO$_2$[2], the arrangements of oxygen atoms and cerium atoms are strongly disordered, but during the subsequent relaxation process, most of cerium disordering recovers, and mainly oxygen vacancies remain along the ion beam path. The XRD and EXAFS results as well as this MD simulation suggest that as a result of electronic excitation, oxygen

---

[1] Osaka Prefecture University
[2] Japan Atomic Energy Agency (JAEA)

vacancies are mainly produced along energetic ion path.

Figure 2 shows the effect of thermal annealing at 1273K on the magnetic property of CeO$_2$. In the case of vacuum annealing, as it is quite difficult to estimate the volume of the reduced region, we can hardly obtain the magnetization value for the reduced (oxygen-deficient) region quantitatively. Therefore, in the figure, we plotted the raw value of the magnetic moment. For comparison, the magnetic moment for the non-reduced specimen is also shown in the figure. The figure clearly shows the appearance of the ferromagnetic state by the vacuum annealing at 1273K. The result of the annealing experiment confirms that oxygen vacancies play an important role in the appearance of the ferromagnetism in CeO$_2$.
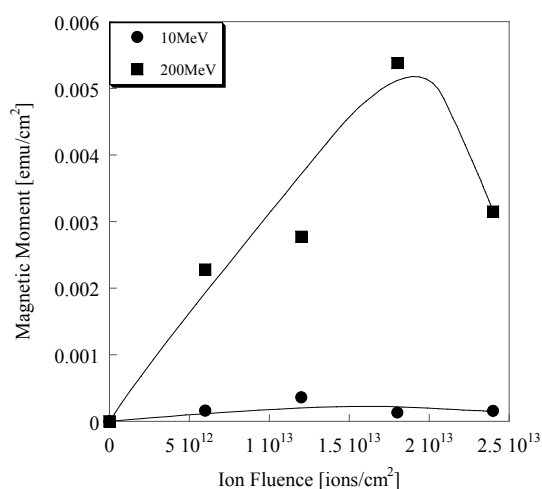
Fig. 1 Magnetic moment per the unit area (1 cm^2) for 200 MeV Xe ion and 10 MeV I ion irradiated CeO$_2$ specimens as a function of the ion fluence.
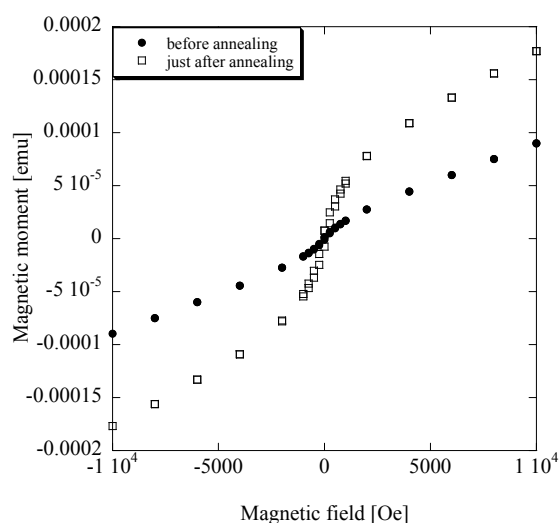
Fig. 2 Magnetic moment for CeO$_2$ specimen before and after annealing in vacuum as a function of external magnetic field.

References

[1] T. Kishino et al., Jpn. J. Appl. Phys., 53 (2014)05FC07.
[2] Y. Sasajima et al., Nucl. Instrum. Methods B, 314 (2013) 202–207.

7.8 Effect of nuclear stopping power on the track formation in amorphous silicon nitride

T. Kitayama[1], Y. Morita[2], K. Nakajima[1], M. Tsujimoto[1], S. Isoda[1], M. Mastuda[2],
M. Sataka[2], K. Narumi[2], Y. Saitoh[2] and K. Kimura[1]

When an energetic ion passes through a material, an ion track may be produced along the ion path if the electronic stopping power is larger than a material dependent threshold value and the diameter of the ion tracks increases with the electronic stopping power. Recently, we have demonstrated that ion tracks in amorphous silicon nitride (a-SiN) thin films produced by 0.36 − 5 MeV C_{60} ion impact can be clearly observed using transmission electron microscopy (TEM) and high-angle annular dark field scanning transmission electron microscopy (HAADF-STEM) [1-2]. Figure 1 shows the diameter of the observed tracks as a function of C_{60} ion energy. The diameter of the observed track is almost constant from 0.36 to 5 MeV while the electronic stopping power (dashed line) increases from 7 to 25 keV/nm. Considering that the nuclear stopping powers of these C_{60} ions (dot-dashed line) are comparable to the electronic stopping power, this indicates that the nuclear stopping power plays an important role in the track formation. In the present study, the ion tracks produced by swift heavy ions are observed in the energy region where the electronic stopping is dominant to estimate the effect of the nuclear stopping power on the track formation.

Self-supporting a-SiN films of 30 nm thickness were irradiated with 200 MeV Au, Kr^{14+} and 415 MeV Au ions to fluences ~ 1×10^{11} ions/cm^2. The Au ions were incident on the sample after passing through a thin carbon foil to achieve an equilibrium charge state. After the ion irradiation, TEM and HAADF-STEM observations were performed using a JEOL JEM-2200FS equipped with a field emission gun operating at 200 kV. The samples were held at the specimen tilting holder with the tilt angle from -30 to 30 degrees. The images were taken by GATAN Ultrascan 1000 CCD camera with a 2k × 2k pixel. In HAADF-STEM mode, a narrow electron beam converged to 0.5 nm diameter and an annular dark detector covering over 120 mrad were used.

The ion tracks were clearly observed by TEM and HAADF-STEM for the a-SiN films irradiated with 200 and 415 MeV Au ions while no ion track was
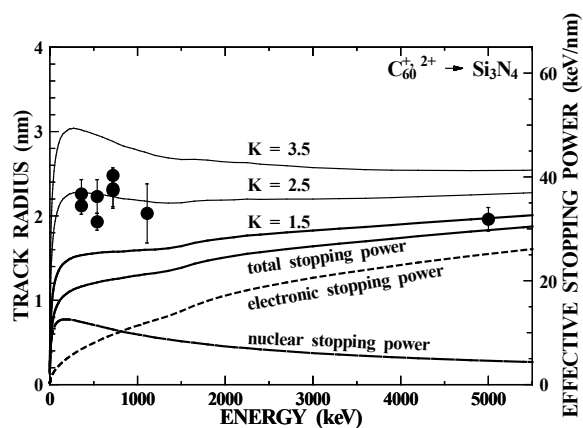
Fig. 1 Observed track radius as a function of C_{60} ion energy. Electronic and nuclear stopping powers together with the effective stopping power are also shown.

[1] Kyoto University
[2] Japan Atomic Energy Agency (JAEA)
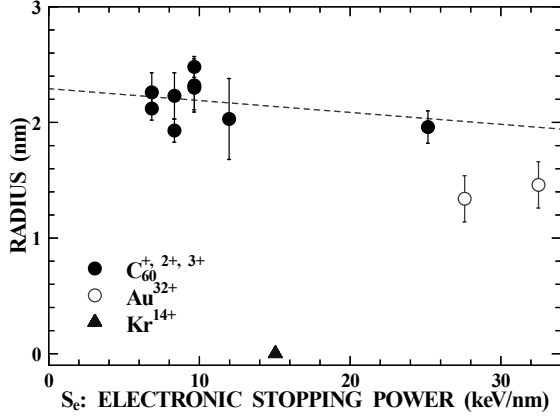
Fig. 2 Observed track radius as a function of the electronic stopping power.
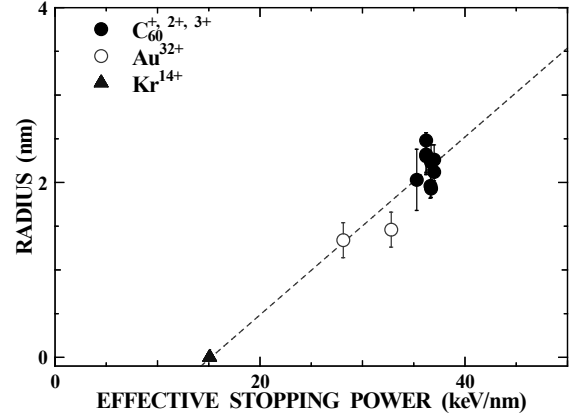
Fig. 3 Observed track radius as a function of the effective stopping power.

observed for the irradiation of 200 MeV Kr^{14+} ions.   The diameters of the tracks were derived from the observed HAADF-STEM images.   Figure 2 shows the observed track radius together with the results of the C_{60} ions as a function of the electronic stopping power. The observed track radius does not depend on the electronic stopping power in a simple manner.   Although the electronic stopping power of the Au ion are larger than those of C_{60} ions, the observed track radius is smaller.   Much larger discrepancy is seen for the result of Kr ions, where no ion track was observed in spite of relatively large stopping power.   These results clearly indicate that the track formation is not governed by the electronic stopping power only. Instead, the nuclear stopping power plays more important role.   Assuming that the nuclear stopping power S_n is a factor of K more efficient than the electronic stopping power S_e, the effective stopping power S_{eff} for the track formation can be written by

$$S_{eff} = S_e + K \times S_n .$$ (1)

The calculated effective stopping powers for various values of K are compared with the observed track radius in Fig. 1.   The energy dependence of the calculated effective stopping power with $K = 2.5$ is very similar to that of the observed track radius, *i.e.* both are almost constant in the present energy region.   This suggests that the nuclear stopping power is 2.5 times more efficient for track formation compared to the nuclear stopping power.   The effective stopping powers were also calculated for Kr and Au ions using eq. (1) with the same K value.   Figure 3 shows the observed track radius as a function of the estimated effective stopping power.   Differently from Fig. 2, all data points align along the same line irrespective of ion species.   This indicates that the concept of the effective stopping power for the track formation can be applicable over a wide range of energy and ion species.

References

[1] K. Nakajima et al., Nucl. Instrum. Methods Phys. Res., B291 (2012) 12-16.
[2] Y. Morita et al., Nucl. Instr. and Methods Phys. Res., B 315 (2013) 142-145.

7.9 Clustering of exchanged cations in Zeolite using high energy heavy ion irradiation

S. Okayasu[1] and Y. Sasaki[2]

High energy heavy ion irradiations on zeolite films causes the structural changes. The crystal structure becomes amorphous along the ion tracks due to high energy transfer from the bombarding ions to the sample. We reported that silver compound clusters are formed 8 - 20 nm in diameter and aligned in the amorphous regions of after the ion bombardments on a zeolite sample including exchanged Ag-cations (Ag-zeolite). Before the ion bombardments, the included cations (typically Na^+) inside zeolite are easily exchangeable to other cations (such as Ag^+, Cs^+, Mn^{2+}) in water solution. After the bombardments, however, the exchanged cations existing in zeolite are clustered along the tracks. The application based on the technique is issued as a patent (Patent number 5505609). Figure 1 shows a cross sectional and a plain view of TEM images for a zeolite sample including exchanged Ag-cations after heavy ion irradiation (200MeV Au ions, fluence 1×10^{12} ions/cm^2).
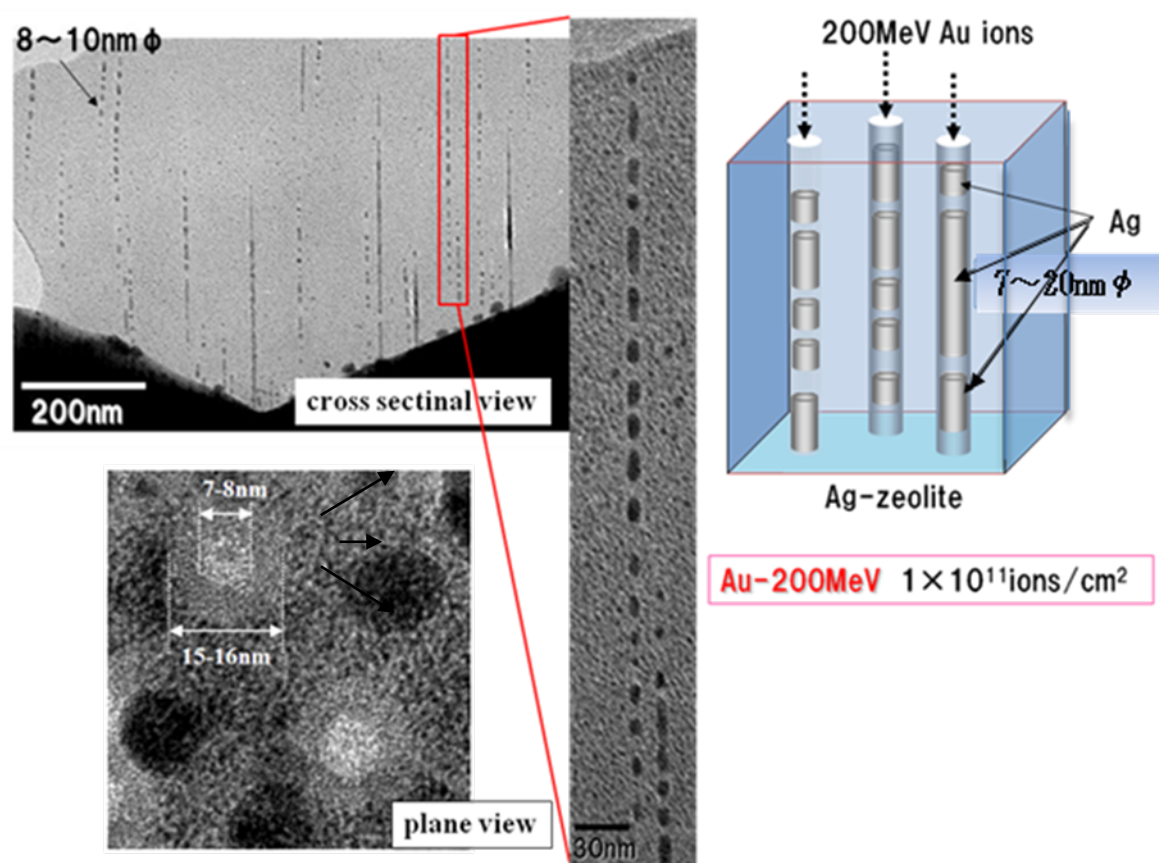
Fig.1 Aligned silver clusters formed along 200MeV-Au ion irradiation tracks.

[1] Japan Atomic Energy Agency (JAEA)
[2] Japan Fine Ceramics Center (JFCC)

Our present interest is to find a way for an actual usage of the patent. For this purpose, we apply the irradiation method to cesium-exchanged zeolite samples. Figure 2 shows temperature dependence of magnetic susceptibility for zeolite-X (a kind of fuajasite, including Na^+ cations, un-exchanged) and cesium-exchanged zeolite-X (Cs-zeolite-X, mostly Na^+ cations are exchanged to Cs^+) measured by a commercial SQUID magnetometer (MPMS-5, Quantum Design Inc.). The applied field is 100Oe. For zeolite-X, the susceptibility mostly obey the Curie-Weiss law from 2K to 300K. On the other hand, the susceptibility of the Cs-zeolite-X shows a ferro-magnetic ordering at 30K. Considering that free cations with magnetic moments in zeolite frameworks show para-magnetic, this magnetic ordering suggests a strong covalent binding between Cesium cations and oxygen atoms constructing the zeolite cages.
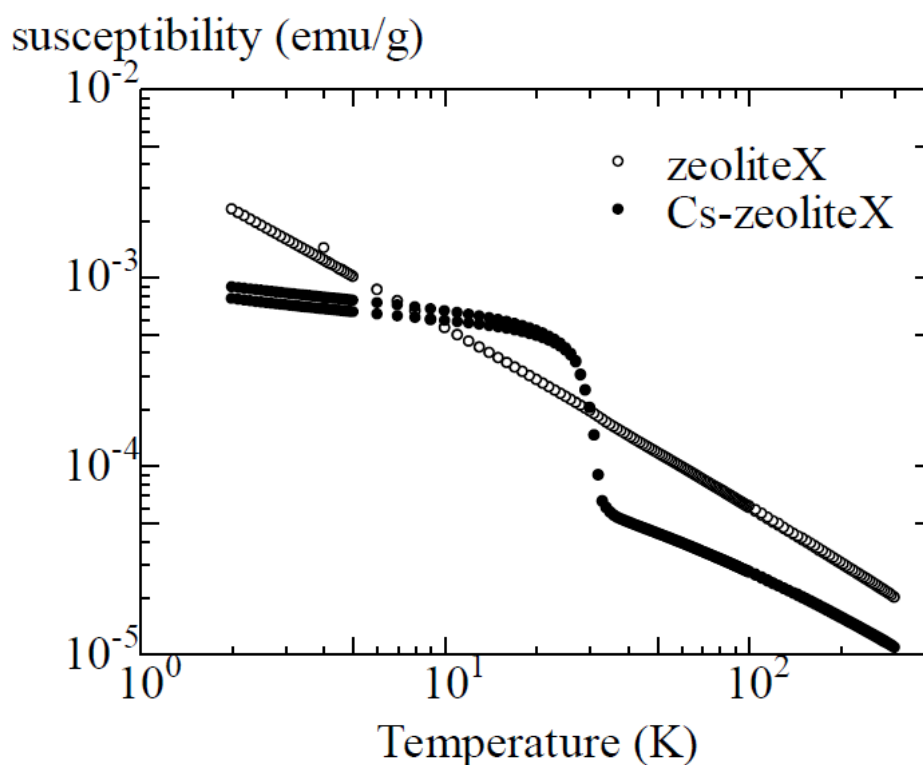
Figure 2 Temperature dependence of magnetic susceptibility for zeolite-X and Cs-zeolite-X.

We will confirm the change of the magnetic properties of Cs-zeolite-X after irradiations.

Reference
[1] S. Okayasu et al., Solid State Comm., 73 (1990) 593-596.

7.10   Quantitative hydrogen analysis for hydrogen-implanted sapphire by NRA method

N. Ishikawa[1], M. Matsuda[1], N. Okubo[1], H. Ogawa[1] and I. Ioka[1]

In general, hydrogen can easily penetrate in a solid material and causes degradation of structural materials. For example, metal hydride is a brittle compound which not only causes hydrogen embrittlement, but also causes unwanted volume change of the material. Formation of zirconium hydride in cladding materials for nuclear fuels in light water reactor is one of the problems to be solved, because absorption of hydrogen may cause unfavorable effect on fuel performance. Therefore, it is important to elucidate the mechanism of hydrogen diffusion and hydride formation by developing nondestructive hydrogen analysis setup.

Nuclear reaction analysis (NRA) is a very useful method to analyze hydrogen contained in a solid materials. Hydrogen can be detected by using the reaction $^{15}N+^{1}H \rightarrow ^{12}C+\alpha+\gamma$ which exhibits nuclear resonance at the ^{15}N beam energy of 6.385MeV.   By measuring the γ-ray from this resonance reaction, concentration of hydrogen can be measured in a precise way. Major advantages of this technique is the following. Absolute concentration of hydrogen atoms can be evaluated. The depth-profile of hydrogen can be measured with high spatial depth resolution by varying the ion energy systematically.   Nondestructive analysis is possible.

Recently NRA setup has been developed recently in the H1 beamline of the tandem accelerator at JAEA-Tokai, our group has started analyzing hydrogen distribution of various materials raging for example cladding materials and oxide materials.   In this report, the result of quantitative hydrogen analysis for hydrogen-implanted sapphire by NRA method will be presented.

The specimen for the present hydrogen analysis is prepared by irradiating sapphire (Al_2O_3 single crystal) with 250 keV H ions up to 1.0×10^{17} H/cm^2 at TIARA facility in JAEA-Takasaki. Depth profile of implanted hydrogen atoms is measured by varying the energy of ^{15}N beam from 9 to 11 MeV which corresponds to the measurement at the depth from 1.0 to 1.8 μm.   The depth where hydrogen concentration is measured corresponds to the depth where the energy of ^{15}N reaches the resonance energy (6.385MeV).   Such calculation of depth is done by using SRIM calculation code[1]. Kapton film is also used as a reference specimen. Kapton is one of the polyimides, and its chemical formula is $(C_{22}H_{10}N_2O_5)_n$.   Its density is assumed to be 1.42 g/cm^3 when its hydrogen concentration is calculated.

Bismuth germanium oxide (BGO) scintillator is used for the γ-ray detector, and its diameter and length are 3 inches and 3 inches, respectively. The scintillator is placed close behind the specimen holder. The relative concentration of hydrogen can be measured in the unit of counts/Coulomb by measuring γ-ray counts divided by the incident charge of $^{15}N^+$ ions in the unit of Coulomb. Figure 1 shows the depth profile of

---

[1] Japan Atomic Energy Agency (JAEA)

hydrogen concentration detected by NRA for hydrogen-implanted sapphire. The figure show that hydrogen atoms are localized around 1.6μm depth. The γ-ray signal averaged over the same volume (1.0 μm thick layer from 1.0 to 2.0 μm depth) is 4.1×10^7 counts/C. According to SRIM calculation, the concentration of hydrogen atoms averaged over the same 1.0 μm thick layer (from 1.0 to 2.0 μm depth) is 9.9×10^{20} H/cm^3. Therefore, the γ-ray signal of 1 counts/C corresponds to hydrogen concentration of 2.4×10^{13} H/cm^3. The summary of the results are shown in Table 1.

In order to test the accuracy of the above measurement, hydrogen concentration is measured also for Kapton film which is known to have hydrogen atoms of 2.2×10^{22} H/cm^3 when assuming 1.42 g/cm^3. The γ-ray signal detected for 7 MeV ^{15}N beam is 1.9×10^9 counts/C. Therefore, in the case of Kapton film, the γ-ray signal of 1 counts/C corresponds to hydrogen concentration of 1.3×10^{13} H/cm^3. Although the ratio of hydrogen concentration to γ-ray counts for hydrogen-implanted sapphire is nearly twofold of that for Kapton film, it can be concluded that order estimate of hydrogen concentration is possible by the present measurement setup.

The next step is to measure spatial distribution of hydrogen absorbed in zircalloy when oxidized in high temperature water steam. Since formation of hydride may results in hydrogen embrittlement of the fuel cladding rod, hydrogen analysis of such oxidized cladding is an important task.
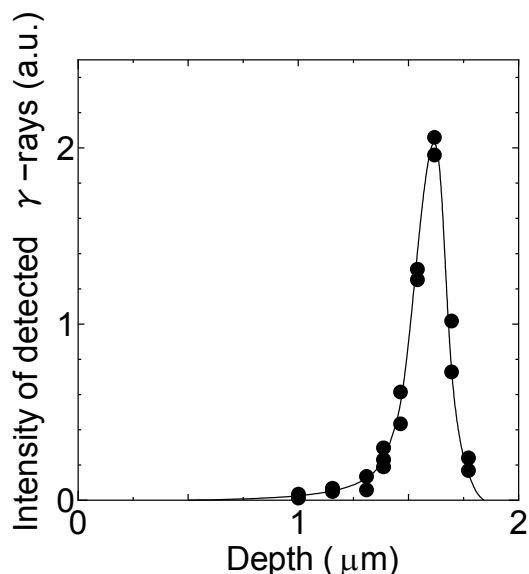
Fig.1 Depth profile of hydrogen concentration detected by NRA method for sapphire which is implanted with hydrogen ions up to 1.0×10^{17} H/cm^2.

Table 1. Detected γ-ray, calculated hydrogen concentration, and the ratio of the two parameters.

Specimens	(a) Averaged γ-ray counts (counts/C)	(b) Averaged H concentration (H/cm^3)	Ratio (b)/(a)
Hydrogen-implanted sapphire	4.1×10^7	9.9×10^{20}	2.4×10^{13}
Kapton film	1.7×10^9	2.2×10^{22}	1.3×10^{13}

References

[1] J.F. Ziegler, Nucl. Instrum. Methods Phys. Res., B 219-220 (2004) 1027.

– 75 –

CHAPTER 8

Publication in Journal and Proceedings, and Contribution to Scientific Meetings

This is a blank page.

8.1 Accelerator Operation and Development

Journal/Proceedings

M. Matsuda, A. Osa, S. Abe, N. Ishizaki, H. Tayama, T. Nakanoya, H. Kabumoto, M. Nakamura,
K. Kutsukake, Y. Otokawa and T. Asozu
Present Status of JAEA-Tokai Tandem Accelerator and Booster
Proc. of the 10th Annual Meeting of Particle Accelerator Society of Japan, Nagoya (Aug. 3-5, 2013) 307-309.

M. Matsuda, T. Asozu, M. Sataka and A. Iwase
Development of Dual-Beam system using an electrostatic accelerator for in-situ observation of swift heavy ion irradiation effects on materials
Nucl. Instrum. Methods Phys. Res., B314 (2013) 43-46.

H. Kabumoto, A. Osa, S. Abe, N. Ishizaki, H. Tayama, M. Matsuda, T. Nakanoya, N. Nakamura,
K. Kutsukake, Y. Otokawa, S. Hanashima, Y. Tsukihashi, M. Sataka and T. Ishii
Present Status of JAEA-Tokai Tandem Accelerator facility
Proc. of the 26th Meeting for Tandem Accelerators and their Associated Technologies, Yamagata, Yamagata univ. (Jul. 5-6, 2013) 54-57.

Meetings

M. Matsuda, A. Osa, S. Abe, N. Ishizaki, H. Tayama, T. Nakanoya, H. Kabumoto, M. Nakamura,
K. Kutsukake, Y. Otokawa and T. Asozu
Present Status of JAEA-Tokai Tandem Accelerator and Booster
Proc. of the 10th Annual Meeting of Particle Accelerator Society of Japan, Nagoya (Aug. 3-5, 2013) .

H. Kabumoto, A. Osa, S. Abe, N. Ishizaki, H. Tayama, M. Matsuda, T. Nakanoya, N. Nakamura,
K. Kutsukake, Y. Otokawa, S. Hanashima, Y. Tsukihashi, M. Sataka and T. Ishii
Present Status of JAEA-Tokai Tandem Accelerator facility
The 26th Meeting for Tandem Accelerators and their Associated Technologies, Yamagata, Yamagata univ. (Jul. 5-6, 2013).

8.2 Nuclear Structure

Journal/Proceedings

C. He, S. Shen, S. Wen, L. Zhu, X. Wu, G. Li, Y. Zhao, Y. Yan, Z. Bai, Y. Wu, Y. Li, G. Li, S. Yan, M. Oshima, Y. Toh, A. Osa, M. Koizumi, Y. Hatsukawa, M. Matsuda and T. Hayakawa,
Signature splitting inversion and backbending in ^{80}Rb,
Phys. Rev. C 87 (2013) 034320 1-10.

G. S. Li, M. L. Liu, X. H. Zhou, Y. H. Zhang, Y. X. Liu, N. T. Zhang, W. Hua, Y. Zheng, Y. D. Fang, S. Guo, J. G. Wang, Y. H. Qiang, B. Ding, L. Ma, M. Oshima, Y. Toh, M. Koizumi, A. Osa, Y. Hatsukawa and M. Sugawara
In-beam γ spectroscopy of the even-even nucleus ^{190}Pt
Phys. Rev. C 89 (2014) 054303 1-9.

M. Koizumi, J. Goto, S. Matsuki, and S. Nakamura,
Dynamic nuclear self-polarization for measurements of nuclear magnetic moments
Nuclear Instrum. Methods Phys. Res. B317 (2013) 689-692.

H. Hayashi, M. Shibata, M. Asai, A. Osa, T. K. Sato, M. Koizumi, A. Kimura and M. Oshima
Performance of a total absorption clover detector for Q_β measurements of neutron-rich nuclei far from the β-stability line
Nucl. Instrum. Methods in Phys. Res. A, 747 (2014) 41.

M. Miyabe, M. Oba, H. Iimura, K. Akaoka, Y. Maruyama, H. Ohba, M. Tampo and I. Wakaida
Laser ablation absorption spectroscopy for remote analysis of uranium
Hyperfine Interact., 216 (2013) 71-77.

T. Sonoda, M. Wada, H. Tomita, C. Sakamoto, T. Takatsukasa, T. Noto, H. Iimura, Y. Matsuo, T. Kubo, T. Shinozuka, T. Wakui, H. Mita, S. Naimi, T. Furukawa, Y. Itou, P. Schury, H. Miyatake, S. Jeong, H. Ishiyama, Y. Watanabe and Y. Hirayama
Development of a gas cell-based laser ion source for RIKEN PALIS
Hyperfine Interact., 216 (2013) 103-107.

H. Tsuchiya, H. Harada, M. Koizumi, F. Kitatani, J. Takamine, M. Kureta and H. Iimura
A Monte Carlo simulation to study a design of a gamma-ray detector for neutron resonance densitometry
Nucl. Instrum. Methods Phys. Res., A729 (2013) 338-345.

Meetings

M. Asai
Nuclear structure of the heaviest elements revealed in α-spectroscopic studies
CHE 8: 8th Workshop on the Chemistry of the Heaviest Elements, Takayama, Japan (Sep. 19-21, 2013).

M. Asai
Alpha-decay spectroscopy of transfermium nuclei at JAEA
16th ASRC International Workshop "Nuclear Fission and Structure of Exotic Nuclei", Tokai, Japan (Mar. 18-20, 2014).

M. Asai, K. Tsukada, Y. Kasamatsu and Y. Okabe
Assingments of the $1/2^+[631]$ states in $N = 151$ nuclei through a-decay spectroscopy of ^{253}Fm and ^{251}Cf
69th Annual Meeting of the Physical Society of Japan, Hiratsuka, Japan (Mar. 27-30, 2014).

H. Iimura
Collinear laser spectroscopy at SLOWRI
7th Nuclear Spectroscopy with Stored or Stopped Radio Isotope Beam, Wako, Japan (Mar. 3-4, 2014).

S. Go, E. Ideguchi, M. Kobayashi, R. Yokoyama, K. Kisamori, S. Michimasa, S. Shimoura, M. Niikura, A. Yagi, H. Nishibata, I. Matea, D. Suzuki, D. Verney, F. Azaiez, M. Sugawara, M. Koizumi, Y. Toh, T. Shizuma, A. Kimura, H. Harada, Y. Furutaka, S. Nakamura, F. Kitatani, Y. Hatsukawa and M. Ohshima
Study of high spin states in $^{35,36}S$
2nd Workshop on the physics at the Tandem-ALTO facility, Orsay, France (May 14-15, 2013).

8.3 Nuclear Reaction

Journal/Proceedings

S. Ota, H. Makii, T. Ishii, C. Angell, D. W. Bardayan, S. Chiba, I. Nishinaka, K. Nishio, M. Matos, S. Mitsuoka and S. Pain
The $^6Li(^{22}Ne,^{26}Mg)d$ α-transfer experiment for the study of low-energy resonances in $^{22}Ne(α,γ)^{26}Mg$
EPJ Web of Conferences 66, 07017 (2014).

S. Rothe, A. N. Andreyev, S. Antalic, A. Borschevsky, L. Capponi, T. E. Cocolios, H. De Witte, E. Eliav, D. V. Fedorov, V. N. Fedosseev, D. A. Fink, S. Fritzsche, L. Ghys, M. Huyse, N. Imai, U. Kaldor, Yuri Kudryavtsev, U. Köster, J. F. W. Lane, J. Lassen, V. Liberati, K. M. Lynch,B. A. Marsh, K. Nishio, D. Pauwels,V. Pershina, L. Popescu, T. J. Procter, D. Radulov, S. Raeder, M. M. Rajabali, E. Rapisarda, R. E. Rossel, K. Sandhu, M. D. Seliverstov, A. M. Sjödin, P. Van den Bergh, P. Van Duppen, M. Venhart, Y. Wakabayashi and K. D. A. Wendt
Measurement of the first ionization potential of astatine by laser ionization spectroscopy
Nature Communications 4, 1835-1-6 (2013).

A. N. Andreyev, M. Huyse, P. Van Duppen, C. Qi, R. J. Liotta, S. Antalic, D. Ackermann, S. Franchoo, F. P. Heßberger, S. Hofmann, I. Kojouharov, B. Kindler, P. Kuusiniemi, S. R. Lesher, B. Lommel, R. Mann, K. Nishio, R. D. Page, B. Streicher, Š. Šáro, B. Sulignano, D. Wiseman and R. A. Wyss
Signatures of the Z = 82 shell closure in α-decay process
Phys. Rev. Lett. 110, 242502-1-5 (2013).

A. N. Andreyev, V. Liberati, S. Antalic, D. Ackermann, A. Barzakh, N. Bree, T. E. Cocolios, J. Diriken, J. Elseviers, D. Fedorov, V. N. Fedosseev, D. Fink, S. Franchoo, S. Heinz, F. P. Heßberger, S. Hofmann, M. Huyse, O. Ivanov, J. Khuyagbaatar, B. Kindler, U. Köster, J. F. W. Lane, B. Lommel, R. Mann, B. Marsh, P. Molkanov, K. Nishio, R. D. Page, N. Patronis, D. Pauwels, D. Radulov, Š. Šáro, M. Seliverstov, M. Sjödin, I. Tsekhanovich, P. Van den Bergh, P. Van Duppen, M. Venhart and M. Veselský
α-decay spectroscopy of the chain $^{179}Tl^g→^{175}Au^g→^{171}Ir^g→^{167}Re^m$
Phys. Rev. C 87, 054311-1-8 (2013).

J. Elseviers, A. N. Andreyev, M. Huyse, P. Van Duppen, S. Antalic, A. Barzakh, N. Bree, T. E. Cocolios, V. F. Comas, J. Diriken, D. Fedorov, V. N. Fedosseev, S. Franchoo, L. Ghys, J. A. Heredia, O. Ivanov, U. Koster, B. A. Marsh, K. Nishio, R. D. Page, N. Patronis, M. D. Seliverstov, I. Tsekhanovich, P. Van den Bergh, J. Van De Walle, M. Venhart, S. Vermote, M. Veselsky and C. Wagemans
β-delayed fission of ^{180}Tl
Phys. Rev. C 88, 044321-1-13 (2013).

V. Liverati, A. N. Andreyev, S. Antalic, A. Barzakh, T. E. Cocolios, J. Elseviers, D. Fedorov, V. N. Fedosseev, M. Huyse, D. T. Joss, Z. Kalaninová, U. Köster, J. F. W. Lane, B. Marsh, D. Mengoni, P.

Molkanvo, K. Nishio, R. D. Page, N. Patronis, D. Pauwels, D. Radulov, M. Seliverstov, M. Sjödin, I. Tsekhanovich, P. Van den Bergh, P. Van Duppen, M. Venhart and M. Veselsky
β-delayed fission and α decay of ^{178}Tl
Phys. Rev. C 88, 044322-1-10 (2013).

K. Nishio
In-beam fission study for heavy element synthesis
EPJ Web of Conferences 62, 03001-1-6 (2013).

H. Haba, M. Huang, D. Kaji, J. Kanaya, Y. Kudou, K. Morimoto, K. Morita, M. Murakami, K. Ozeki, R. Sakai, T. Sumita, Y. Wakabayashi, A. Yoneda, Y. Kasamatsu, Y. Kikutani, Y. Komori, K. Nakamura, A. Shinohara,. H. Kikunaga, H. Kudo, K. Nishio, A. Toyoshima and K. Tsukada
Production of ^{262}Db in the $^{248}Cm(^{19}F,5n)^{262}Db$ reaction and decay properties of ^{262}Db and ^{258}Lr
Phys. Rev. C 89, 024618-1-11 (2014).

K. Nishio, H. Ikezoe, S. Hofmann, F.P. Heßberger, D. Ackermann, S. Antalic, Y. Aritomo, V.F. Comas, Ch.E. Düllman, A. Gorshkov, R. Graeger, S. Heinz, J.A. Heredia, K. Hirose, J. Khuyagbaatar, B. Kindler, I. Kojouharov, B. Lommel, H. Makii, R. Mann, S. Mitsuoka, Y. Nagame, I. Nishinaka, T. Ohtsuki, A.G. Popeko, Š. Šáro, M. Schädel, A. Türler, Y. Wakabayashi, Y. Watanabe, A. Yakushev and A.V. Yeremin
Study of heavy-ion induced fission for heavy-element synthesis
EPJ Web of Conferences 66, 03065-1-4 (2014).

Meetings

S. Ota, H. Makii, T. Ishii, C. Angell, D. W. Bardayan, S. Chiba, I. Nishinaka, K. Nishio, M. Matos, S. Mitsuoka and S. Pain
The $^6Li(^{22}Ne,^{26}Mg)d$ α-transfer experiment for the study of low-energy resonances in $^{22}Ne(α,γ)^{26}Mg$
The 24th International Nuclear Physics Conference (INPC2013), Florence, Italy (Jun. 2-7, 2013).

K. Nishio
In-beam fission study at JAEA
Heavy Ion Accelerator Symposium on Fundamental and Applied Science (HIAS2013), Canberra, Australia (Apr. 8-12, 2013).

K. Nishio
In-beam fission study for heavy element synthesis
Fifth International Workshop on Nuclear Fission and Fission-Products Spectroscopy (FISSION2013), Caen, France (May 28-31, 2013).

K. Nishio

Experimental-study for heavy-ion induced fission

French-Japanese Symposium on Nuclear Structure Problems (LIA2013), Paris, France (Sep. 30-Oct. 3, 2013).

K. Nishio

Fission research at JAEA and opportunity with J-PARC for fission and nuclear data

INT Workshop on Experimental Status and Prospects (part of INT Program INT-13-3 Quantum Large Amplitude Shape and Dynamics), Seattle, USA (Oct. 14-18, 2013).

K. Nishio

Fusion and Fission Study at JAEA

6th International Conference FUSION14, IUAC, New Delhi (Feb. 24-28, 2014).

K. Nishio

Fission study and nuclear data measurement at JAEA

16th ASRC International Workshop "Nuclear Fission and Structure of Exotic Nuclei", Tokai, Japan (Mar. 18-20, 2014).

K. Nishio

Measurement of neutron-induced fission cross sections for actinice nuclei using the ANNRI

2nd ANNRI Symposium, Tokai, Japan (Aug. 23, 2013).

K. Nishio, K. Hirose, I. Nishinaka, H. Makii, S. Ota, T. Nagayama, S. Chiba, K. Tsukada, M. Asai, T. Ishii, T. Otsuki, S. Araki and Y. Watanabe

Study of delayed-neutron yields for acculate evaluation of kinetics of high-burnup reactors(2) : Measurement of fission fragnment mass distributions for actinide nuclei by surrogate method

Fall meeting of the Atomic Energy Societry of Japan, Hachinohe-Aomori (AESJ) (Sep.3-5, 2013).

I. Nishinaka, A. Yokoyama, K. Washiyama, R. Amano, E. Maeda, N. Yamada, H. Makii, A. Toyoshima, S. Watanabe, N. S. Ishioka and K. Hashimoto

Production and separation of radioactive astatine isotopes in the $^7Li + {}^{nat}Pb$ reaction

8th International Symposium on Targeted Alpha Therapy, Oak Ridge, Tennessee, USA (Jun. 4-6, 2013).

I. Nishinaka, A. Yokoyama, K. Washiyama, R. Amano, E. Maeda, T. Taniguchi, N. Yamada, H. Makii, A. Toyoshima, S. Watanabe, N. S. Ishioka and K. Hashimoto

Production and utilization of radioactive astatine isotopes in the $^7Li + {}^{nat}Pb$ reaction

5th Asia Pacific Symposium on Radiochemistry 13, Kanazawa, Japan (Sep. 22-27, 2013).

I. Nishinaka

Production and utilization of α-radioactive isotopes astatine at the JAEA-Tokai tandem accelerator

Meeting of Research Center for Electron Photon Science of Tohoku University "RI production and application using electron accelerator", Sendai, Japan (Mar. 25, 2014).

E. Maeda, A.Yokoyama, T. Taniguchi, K. Washiyama and I. Nishinaka

Extraction of astatine isotopes for development of radiopharmaceuticals

5th Asia Pacific Symposium on Radiochemistry 13, Kanazawa, Japan (Sep. 22-27, 2013).

8.4 Nuclear Chemistry

Journal/Proceedings

N. Sato, T. K. Sato, M. Asai, A. Toyoshima, K. Tsukada, Z. J. Li, K. Nishio, Y. Nagame, M. Schädel, H. Haba, S. Ichikawa and H. Kikunaga
Production of ^{256}Lr in the $^{249,250,251}Cf + ^{11}B$, $^{243}Am + ^{18}O$, and $^{248}Cm + ^{14}N$ reactions
Radiochim. Acta, 102 (2014) 211-219.

A. Toyoshima, Z. J. Li, M. Asai, N. Sato, T. K. Sato, T. Kikuchi, Y. Kaneya, Y. Kitatsuji, K. Tsukada,
Y. Nagame, M. Schädel, K. Ooe, Y. Kasamatsu, A. Shinohara, H. Haba and J. Even
Measurement of the Md^{3+}/Md^{2+} reduction potential studied with flow electrolytic chromatography
Inorg. Chem. 52, 12311-12313 (2013).

Meetings

Y. Hatsukawa, K. Tsukada, K. Hashimoto, T. Sato, M. Asai, T. Kin, A. Toyoshima and Y. Nagai.
Production of ^{95m}Tc, for Compton camera imaging
245th American Chemical Society Meeting, New Orleans, LA USA (Apr. 7-11, 2013).

Y. Hatsukawa, K. Hashimoto, K. Tsukada, T. Sato, M. Asai, A. Toyoshima ,Y. Nagai, T. Tanimori,
S. Sonoda, S. Kabuki, H. Saji and H. Kimura
Production of ^{95m}Tc for Compton camera imaging
5th Asia-Pacific Symposium on Radiochemistry '13(APSORC13) (Sep. 23-27, 2013).

S. Kabuki, S. Sonoda, Y. Hatsukawa, H. Kimura, M. Asai, K. Hashimoto, S. Komura, H. Kubo,
Y. Matsuoka, T. Mizumoto, Y. Nagai, S. Nakamura, T. Sato, T. Sawano, T. Takada, A. Toyoshima,
K. Tsukada, E. Kunieda and T. Tanimori
Imaging Study of An Electron-Tracking Compton Camera for Nuclear Medicine
55th Annual Meeting & Exhibition, the American Association of Physicists in Medicine Chemical Society
Meeting, New Orleans, LA USA (Aug. 4-8, 2013).

A. Toyoshima, S. Miyashita, M. Asai, T. K. Sato, Y. Kaneya, K. Tsukada, Y. Kitatsuji, Y. Nagame,
M. Schädel, H. V. Lerum, J. P. Omtvedt, Y. Oshimi, K. Ooe, Y. Kitayama, A. Yokoyama, A. Wada, Y. Oura,
H. Haba, J. Kanaya, M. Huang, Y. Komori, T. Yokokita, Y. Kasamatsu, A. Shinohara, V. Pershina
and J. V. Kratz
Chemical studies of Mo and W in preparation of a seabogrium (Sg) reduction experiment using MDG, FEC, and SISAK
5th Asia-Pacific Symposium on Radiochemistry (APSORC13), Kanazawa, Japan (Sep. 22-27, 2013).

T. K. Sato, M. Asai, N. Sato, K. Tsukada, A. Toyoshima, K. Ooe, S. Miyashita, M. Schädel, Y. Kaneya, Y. Nagame, A. Osa, S. Ichikawa, T. Stora, J. V. Kratz
The first successful ionization of Lr (Z=103) by a surface ionization technique
9th International Conference on the Chemistry and Physics of the Actinide Elements (ACTINIDES2013), Karlsruhe, Germany (Jul. 21-26, 2013).

T. K. Sato, M. Asai, N. Sato, K. Tsukada, A. Toyoshima, K. Ooe, S. Miyashita, M. Schädel, Y. Kaneya, Y. Nagame, A. Osa, S. Ichikawa, T. Stora, J. V. Kratz, D. Renisch, Ch. E. Düllmann
The first successful ionization of Lr (Z=103) by surface ionization
8th Workshop on the Chemistry of the Heaviest Elements (CHE8), Takayama, Japan (Sep.19-21, 2013).

T. K. Sato, M. Asai, N. Sato, K. Tsukada, A. Toyoshima, K. Ooe, S. Miyashita, M. Schädel, Y. Kaneya, Y. Nagame, A. Osa, S. Ichikawa, T. Stora, J. V. Kratz, D. Renisch, Ch. E. Düllmann
The first successful observation of mass-separated lawrencium (Lr, Z=103) with ISOL technique
The 5th Asia-Pacific Symposium on Radiochemistry '13 (APSORC13).

Y. Hatsukawa, K. Tsukada, K. Hashimoto, T. Sato, M. Asai, T. Kin, A. Toyoshima, Y. Nagai, I. Tanimori, S. Sonoda, S. Kabuki, H. Saji and H. Kimura
Production of ^{95m}Tc for Compton camera
American Chemical Society meeting at New Orleans, LA (Apr. 5, 2013).

8.5 Nuclear Theory

Journal/Proceedings

H. Koura
Three-dimensional nuclear char – understanding of nuclear physics and nucleosynthesis in stars
Physics Education 48 (2014) 215-220.

P. Schury, M. Wada, Y. Ito, S.Naimi, T. Sonada, H. Mita, A. Takamine, K. Okada, H. Wollnik, S. Chon, H. Haba, D. Kaji, H. Koura, H. Miyatake, K. Morimoto, K. Morita and A. Ozawa
A multi-reflection time-of-flight mass spectrograph for short-lived and super-heavy nuclei
Nucl. Instrum. Methods Phys. Res., B 317 (2013) 537-543.

D. Steppenbeck, S. Takeuchi, N. Aoi, P. Doornenbal, M. Matsushita, H. Wang, H. Baba, N. Fukuda, S. Go, M. Honma, J. Lee, K. Matsui, S. Michimasa, T. Motobayashi, D. Nishimura, T. Otsuka, H. Sakurai, Y. Shiga, P.-A. Soderstrom, T. Sumikama, H. Suzuki, R. Taniuchi, Y. Utsuno, J.J. Valiente-Dobon and K. Yoneda
Evidence for a new nuclear 'magic number' from the level structure of ^{54}Ca
Nature, 502 (2013) 207-210.

J. Papuga, M.L. Bissell, K. Kreim, K. Blaum, B.A. Brown, M. De Rydt, R.F. Garcia Ruiz, H. Heylen, M. Kowalska, R. Neugart, G. Neyens, W. Nortershauser, T. Otsuka, M.M. Rajabali, R. Sanchez, Y. Utsuno and D.T. Yordanov
Spins and magnetic moments of ^{49}K and ^{51}K: establishing the $1/2^{+}$ and $3/2^{+}$ level ordering beyond N=28
Phys. Rev. Lett., 110 (2013) 172503-1-5.

F. Flavigny, A. Gillibert, L. Nalpas, A. Obertelli, N. Keeley, C. Barbieri, D. Beaumel, S. Boissinot, G. Burgunder, A. Cipollone, A. Corsi, J. Gibelin, S. Giron, J. Guillot, F. Hammache, V. Lapoux, A. Matta, E.C. Pollacco, R. Raabe, M. Rejmund, N. de Sereville, A. Shrivastava, A. Signoracci and Y. Utsuno
Limited asymmetry dependence of correlations from single nucleon transfer
Phys. Rev. Lett., 110 (2013) 122503-1-5.

Y. Utsuno
Towards unified description of shell evolution - Takaharu Otsuka's achievements
J. Phys.: Conf. Ser., 445 (2013) 012008-1-6.

S. Suchyta, S. N. Liddick, Y. Tsunoda, T. Otsuka, M. B. Bennett, A. Chemey, M. Honma, N. Larson, C. J. Prokop, S. J. Quinn, N. Shimizu, A. Simon, A. Spyrou, V. Tripathi, Y. Utsuno and J. M. VonMoss
Shape coexistence in ^{68}Ni
Phys. Rev. C, 89 (2014) 021301-1-5.

Y. Tsunoda, T. Otsuka, N. Shimizu, M. Honma and Y. Utsuno
Novel shape evolution in exotic Ni isotopes and configuration-dependent shell structure
Phys. Rev. C, 89 (2014) 031301-1-5.

Y. Utsuno, T. Otsuka, N. Shimizu, M. Honma, T. Mizusaki, Y. Tsunoda and T. Abe
Recent shell-model results for exotic nuclei
EPJ Web of Conferences, 66 (2014) 02106-1-8.

Meetings

H. Koura
Properties of nuclear masses for heavy and superheavy nuclei
The 6th RIBF discussion meeting, 'Nuclear mass', Wako, Japan (May 24, 2013).

H. Koura
Extension of calculation of fission barriers to asymmetric shapes on the spherical-basis method
Fall Meeting of the Physical Society of Japan, Kochi, Japan (Sep. 20-23, 2013).

H. Koura and S. Chiba
Improvement of strength function of beta decay for delayed neutron probability
Spring Meeting of the Atomic Energy Society of Japan, Tokyo, Japan (Mar. 26-28, 2014).

H. Koura and S. Chiba
Comprehensive study of delayed-neutron yields for accurate evaluation of kinetics of high-burn up reactors (4) Theoretical study of delayed neutron and decay heat accompanied with beta-decay from fission fragments
Fall Meeting of the Atomic Energy Society of Japan, Hachinohe, Japan (Sep. 3-5, 2013).

H. Koura and S. Chiba
Theoretical study of beta decay for delayed neutron and decay heat
2013 Symposium on Nuclear Data, Fukui, Japan (Nov. 14-15, 2013).

H. Koura
Theoretical study of beta decay for delayed neutron
The 4th International Symposium on Innovative Nuclear Energy Systems　(INES-4), Ookayama, Tokyo, Japan (Nov. 6-8, 2013).

Y. Utsuno
Shell-model approach to shape coexistence in light nuclei
IOP Workshop "Shape Coexistence Across the Chart of Nuclides," York, UK (Apr. 15-16, 2013).

Y. Utsuno

Basics and current issues of the nuclear shell model

A lecture for graduate students (informal), York, UK (Apr. 17, 2013).

Y. Utsuno

Recent shell-model results for exotic nuclei

25th International Nuclear Physics Conference (INPC 2013), Firenze, Italy (Jun. 3-7, 2013).

Y. Utsuno

Tensor-force driven shell evolution studied with large-scale shell-model calculations

RCNP Workshop on the Importance of Tensor Interactions in Nuclei and Hadron Structure (Jul. 11-12, 2013).

Y. Utsuno

Large-scale shell-model calculations for exotic nuclei

The 12th CNS International Summer School (CNSSS13), Wako, Japan (Aug. 28-Sep. 3, 2013).

Y. Utsuno, N. Shimizu, T. Otsuka, T. Yoshida and Y. Tsunoda

Structure of neutron-rich S isotopes

2013 Fall Meeting of the Physical Society of Japan, Kochi, Japan (Sep. 20-23, 2013).

Y. Utsuno, N. Shimizu, T. Otsuka, S. Ebata and M. Honma

Photonuclear reactions of calcium isotopes calculated with the nuclear shell model

The Fourth International Symposium on Innovative Nuclear Energy Systems (INES-4), Tokyo, Japan (Nov. 6-8, 2013).

Y. Utsuno

Large-scale shell-model calculations and evolution of shell structure in exotic nuclei

The 26th Hokkaido Nuclear-Theory Group Workshop—Understanding of Nuclear Forces including Three-Body Forces and Its Effect on Nuclear Structure, Sapporo, Japan (Feb. 20-22, 2014).

Y. Utsuno, T. Otsuka, N. Shimizu, M. Honma, T. Mizusaki and T. Togashi

Evolution of the N=32 and 34 magic numbers in proton sd-shell nuclei

69th Annual Meeting of the Physical Society of Japan, Hiratsuka, Japan (Mar. 27-30, 2014).

8.6   Radiation Effects in Materials

Journal/Proceedings

Y. Sasaki and S. Okayasu
Zeolite and the manufacturing method
(patent number 5505609, 2016/03/28).

Y. Sasajima, N. Ajima, T. Osada, N. Ishikawa and A. Iwase
Molecular dynamics simulation of fast particle irradiation on single crystal CeO$_2$
Nucl. Instrum. Methods Phys. Res., B314 (2013) 202-207.

T. Kishino, K. Shimizu, Y. Saitoh, N. Ishikawa, F. Hori and A. Iwase
Effects of high-energy heavy ion irradiation on the crystal structure in CeO$_2$ thin films
Nucl. Instrum. Methods Phys. Res., B314 (2013) 191-194.

Y. Sasajima, N. Ajima, T. Osada, N. Ishikawa and A. Iwase
Molecular dynamics simulation of fast particle irradiation to the Gd$_2$O$_3$-doped CeO$_2$
Nucl. Instrum. Methods Phys. Res., B316 (2013) 176-182.

Y. Sasajima, T. Osada, N. Ishikawa and A. Iwase
Computer simulation of structural modifications induced by highly energetic ions in uranium dioxide
Nucl. Instrum. Methods Phys. Res., B314 (2013) 195-201.

N. Matsunami, Y. Sakuma, M. Sataka, S. Okayasu and H. Kakiuchida
Electronic sputtering of CuO films by high-energy ions
Nucl. Instrum Methods Phys. Res., B314 (2013) 55.

H. Amekura, N. Okubo, N. Ishikawa, D. Tsuya, K. Mitsuishi, Y. Nakayama, U.B. Singh, S.A. Khan, S. Mohapatra and D.K. Avasthi
Swift heavy ion irradiation of ZnO nanoparticles embedded in silica: Radiation-induced deoxidation and shape elongation,
Appl. Phys. Lett. 103 (2013) 203106.

K. Yasuda, M. Etoh, K. Sawada, T. Yamamoto, K. Yasunaga, S. Matsumura and N. Ishikawa
Defect formation and accumulation in CeO$_2$ irradiated with swift heavy ions
Nucl. Instrum. Methods Phys. Res., B314 (2013) 185.

K. Yasuda, T. Yamamoto, S. Takaki, S. Matsumura and N. Ishikawa
Atomic structure of ion tracks and microstructure evolution in oxides irradiated with swift heavy ions
Proceedings on Eleventh International Topical Meetings on Nuclear Applications of Accelerators (AccApp'13).

S.Takaki, K. Yasuda, T. Yamamoto, S. Matsumura and N. Ishikawa
Atomic structure of ion tracks in Ceria
Nucl. Instrum. Methods Phys. Res., B326 (2014) 140-144.

N. Ishikawa, T. Sonoda, T. Sawabe, H. Sugai, M. Sataka
Electronic stopping power dependence of ion-track size in UO_2 irradiated with heavy ions in the energy range of ~1 MeV/u
Nucl. Instrum. Methods Phys. Res., B314 (2013) 180-184.

N. Okubo , N. Ishikawa, M. Sataka and S. Jitsukawa
Surface amorphization in Al_2O_3 induced by swift heavy ion irradiation
Nucl. Instrum. Methods Phys. Res., B314 (2013) 208-210.

T. Sueyoshi, Y. Furuki, T. Fujiyoshi, F. Mitsugi, T. Ikegami and N. Ishikawa
Influence of anisotropically splayed columnar defects on angular dependence of critical current density in YBCO thin films
TEION KOGAKU (J. Cryo. Super. Soc. Jpn.) Vol. 49 (2014) 139.

T. Sueyoshi, T. Koutaki, T. Fujiyoshi, F. Mitsugi, T. Ikegami and N. Ishikawa
Angular dependence of critical current density in $BaZrO_3$ / $YBa_2Cu_3O_y$ quasi-multilayered films with columnar defects
Physica C494 (2013) 153-157.

T. Sueyoshi, Y. Furuki, E. Tanaka, T. Fujiyoshi, F. Mitsugi, T. Ikegami and N. Ishikawa
Angular dependence of critical current density in YBCO films with columnar defects crossing at widespread angles
IEEE. Trans. Appl. Supercond. 23 (2013) 8002404.

Meetings

Y. Sasaki, M. Kobayashi, S. Okayasu and H. Kita
Formation of Ag-clusters in Ag-exchanged zeolites by ion irradiation
Autumn Symposium , The Ceramic Society of Japan, Ehime Univ. (Sep. 16-18, 2009).

Y. Sasaki, M. Kobayashi, H. Kita and S. Okayasu
Formation of metal microstructures induced by heavy ion irradiation in Ag-zeolite
AMTC2 "The 2nd International Symposium on Advanced Microscopy and Theoretical Calculations".

T.Kishino, R.Shinoda, K.Shimizu, Y.Saitoh, N.Ishikawa, Y.Okamoto, F.Hori, T.Matsui and A.Iwase
Effect of 10MeV iodine ion irradiation on the magnetic properties and lattice structure of CeO₂.
The 2013 JSAP-MRS Joint Symposium, Kyoto (Sep. 16-20, 2013).

A.Iwase, K.Shimizu, T.Kishino, N.Ishikawa, Y.Saitoh and T.Matsui,
Ferromagnetism of CeO₂ induced by high energy heavy ion irradiation and its thermal stability
European MRS 2013 Spring Meeting, Strasburgm, France (May 27-31, 2013).

T.Kishino, K.Shimizu, Y.Saitoh, N.Ishikawa, F.Hori, T.Matsui and A.Iwase
Effects of energetic ion irradiation on CeO₂ bulk pellets and thin films
International Conference on Radiation Effects in Insulators (REI2013), Helsinki, Finland (Jun. 30-Jul. 5, 2013).

H. Amekura, S. Mohapatra, U.B. Singh, S.A. Khan, D.K. Avasthi, N. Okubo and N. Ishikawa
Elongation of metal nanoparticles by swift heavy ion irradiation: an approximated scaling rule
The 17th International Conference on Radiation Effects in Insulators (REI-2013), Helsinki, Finland (Jun. 30-Jul. 5, 2013).

H. Amekura
Shape elongation of nanoparticles induced by swift heavy ion irradiation
E-MRS 2013 Spring Meeting, Strasbourg (May 27-31, 2013).

H. Amekura, N. Okubo, and N. Ishikawa, S. Mohapatra, U.B. Singh, S.A. Khan, P.K. Kulriya, P. Kluth and D.K. Avasthi
Electronic stopping power dependence on shape elongation of Zn nanoparticles under swift heavy ion irradiation
23rd Annual Meeting of MRS-J (2013), Yokohama, Japan (Dec. 9-11, 2013).

H. Amekura, N. Okubo and N. Ishikawa
Elongation of metal nanoparticles in SiO₂ induced by swift heavy ion irradiation (II)
The 74th Autumn Meeting 2013, Kyoto, Japan (Sep. 16-20, 2013).

K. Yasuda, M. Etoh, K. Yasunaga, T. Yamamoto, S. Matsumura and N. Ishikawa
Synergistic effects of electronic and displacement irradiation in CeO₂ induced by with swift heavy ions
Japan Institute of Metals and Materials 2013 Spring Meeting (2013).

S. Takaki, T. Yamamoto, K. Ando, K. Kuwahara, M. Kutsuwada, K. Yasuda, S. Matsumura and N. Ishikawa
Structure of ion tracks in CeO₂ induced by high density electronic excitation
The 69th Annual Meeting of the Japan Society of Microscopy, Suita, Osaka.

S. Takaki, K. Yasuda, T. Yamamoto, S. Matsumura and N. Ishikawa
Atomic structure of ion tracks in ceria
17th International Conference on Radiation Effects in Insulators, Helsinki, Finland (Jun. 30-Jul, 5, 2013).

K. Yasuda, T. Yamamoto, S. Takaki, S. Matsumura and N. Ishikawa
Atomic structure of ion tracks and microstructure evolution in oxide ceramics irradiated with swift heavy ions
Eleventh International Topical Meeting on Nuclear Applications of Accelerators (AccApp'13), Bruges, Belgiuam (Aug. 5-8, 2013).

S. Takaki, T. Yamamoto, M. Kutsuwada, K. Yasuda, S. Matsumura and N. Ishikawa
Atomic-level observation of the structure of ion tracks in CeO₂ irradiated with swift heavy ions
Japan Institute of Metals and Materials 2013 Fall Meeting (2013).

H. Kanei, Y. Chiba, Y. Saito, H. Okada and T. Kameda
Mission and technology of University of Tsukuba ITF-1 "YUI" small satellite – World wide opportunity to feel the space –
The Robotics and Mechatronics Conference 2013 (ROBOMEC2013), Tsukuba, Japan (May 22-25, 2013).

T. Sueyoshi, Y. Furuki, T. Kai, T. Fujiyoshi and N. Ishikawa
Flux pinning properties of splayed columnar defects ranging from B || c-axis to B || ab-plane in GdBCO coated conductors
26rd International symposium on superconductivity (ISS2013), Tokyo, Japan (Nov. 18-20, 2013).

N. Ishikawa
Defect creation due to high-density electronic energy deposition in ion-irradiated oxides
Materials Research Society of Japan (MRS-J), Yokohama, Japan (Dec.9, 2013).

CHAPTER 9

Personnel and Committee

This is a blank page.

9.1   Personnel

Department of Research Reactor and Tandem Accelerator

Takeshi	Maruo	Director	
Tetsuro	Ishii	Deputy Director	(to Sep. 30)
Yoji	Murayama	Deputy Director	
Yoshiya	Torii	Deputy Director	(from Oct. 1)
Noriyuki	Shinoda	Manager of Administration Section	

Department of Research Reactor and Tandem Accelerator

Tandem Accelerator Section (*General Manager)

Scientific Staff

Akihiko	Osa*
Makoto	Matsuda

Technical Staff

Shin-ichi	Abe	
Nobuhiro	Ishizaki	
Hidekazu	Tayama	
Takamitsu	Nakanoya	
Hiroshi	Kabumoto	
Masahiko	Nakamura	
Ken-ichi	Kutsukake	
Yoshinori	Otokawa	
Takuhiro	Asozu	
Susumu	Hanashima	(Temporary Staff)

Department of Radiation Protection

Facility Radiation Control Section I

Tsutomu	Sekita
Teruhiko	Takahashi
Yumi	Ueno
Susumu	Kinase
Akira	Iwasa

Advanced Science Research Center

Sadamichi	Maekawa	Director
Yuichiro	Nagame	Deputy Director
Tomotsugu	Sawai	General Manager of Research Coordination and Promotion Office
Hiroshi	Ikezoe	(Temporary Staff)

Advanced Science Research Center

*Research Group for Reactions involving Heavy Nuclei (* Group Leader)*

Andrei	Andreyev[*]	
Katsuhisa	Nishio	
Ichiro	Nishinaka	
Hiroyuki	Koura	
Yutaka	Utsuno	
Hiroyuki	Makii	
Kentaro	Hirose	
Riccardo	Orlandi	(from Nov. 1)
Romain	Leguillon	(Senior Post Doc., from Dec. 1)
Ryotaro	Tatsuzawa	(Student)
Eita	Maeda	(Student)

Advanced Science Research Center

*Research Group for Superheavy Elements (* Group Leader)*

Matthias	Schädel[*]	
Kazuaki	Tsukada	
Masato	Asai	
Tetsuya K.	Sato	
Atsushi	Toyoshima	
Kazuhiro	Ooe	(Post Doc.)
Sunao	Miyashita	(Post Doc.)
Yusuke	Kaneya	(Student)

Advanced Science Research Center

Research Group for Mechanical Control of Materials and Spin Systems

Satoru   Okayasu   (Deputy Group Leader)

Nuclear Science and Engineering Directorate

*Innovative Nuclear Science Research Group (* Group Leader)*

Hideo   Harada*

Hideki   Iimura

Mitsuo   Koizumi

Kazuyoshi Furutaka

Fumito   Kitatani

Shoji   Nakamura

Yosuke   Toh

Atsushi   Kimura

Kaoru   Hara   (Senior Post Doc.)

Masumi   Oshima   (Temporary Staff)

Nuclear Science and Engineering Directorate

Research Group for Radiation Materials Engineering

Noito   Ishikawa

Nariaki   Okubo

Quantum Beam Science Directorate

Neutron Imaging and Activation Analysis Group

Yuichi   Hatsukawa

9.2 Research Planning and Assessment Committee

Chairman	Kouichiro	Asahi	(Professor, Tokyo Institute of Technology)
Member	Tadashi	Kambara	(Senior Scientist, RIKEN)
	Kenji	Kimura	(Professor, Kyoto University)
	Shigeo	Tomita	(Associate Professor, University of Tsukuba)
	Toshiaki	Kaneko	(Professor, Okayama University of Science)
	Hisaaki	Kudo	(Professor, Niigata University)
	Eiji	Ideguchi	(Associate Professor, Osaka University)
	Hitoshi	Nakada	(Professor, Chiba University)
	Koichi	Hagino	(Associate Professor, Tohoku University)
	Tomotsugu	Sawai	(Advanced Science Research Center, JAEA)
	Hideo	Harada	(Nuclear Science and Engineering Directorate, JAEA)
	Yuichi	Hatsukawa	(Quantum Beam Science Directorate, JAEA)
	Tetsuro	Ishii	(Dep. Research Reactor and Tandem Accelerator, JAEA)
	Makoto	Matsuda	(Dep. Research Reactor and Tandem Accelerator, JAEA)
	Kazumasa	Narumi	(Dep. Advanced Radiation Technology, JAEA)
Organizer Secretary			
	Shin-ichi	Mitsuoka	(Advanced Science Research Center, JAEA)
	Norito	Ishikawa	(Nuclear Science and Engineering Directorate, JAEA)
	Masato	Asai	(Advanced Science Research Center, JAEA)
	Hiroshi	Ikezoe	(Advanced Science Research Center, JAEA)

CHAPTER 10

New Research Programs

10.1 New Research Programs Approved in the FY2013

This is a blank page.

10.1   New Research Programs Approved in the FY2013

Title	Spokesperson & Affiliation
1. Shape and property control of nanoparticles by swift heavy ions *	Hiroshi Amekura National Institute for Materials Science (NIMS)
2. Nanostructure formation induced by swift heavy ion irradiations	Satoru Okayasu JAEA
3. Direct observation of ion tracks in amorphous thin films using TEM	Kenji Kimura Kyoto University
4. Zero-degree electron spectroscopy with 16 MeV C_2^+	Shigeo Tomita University of Tsukuba
5. Nuclear structure studies in the A~100 region using JAEA Recoil Mass Separator – Test run for the asymmetric fusion reaction –	Andrei Andreyev University of York
6. Production of fission isomers by heavy-ion transfer reactions in the sub-barrier energy region	Tetsuro Ishii JAEA
7. Proton configuration of ^{261}Db (2)	Masato Asai JAEA
8. Development for nano-scale diffusion measurements using radioactive ^{8}Li tracer *	Hironobu Ishiyama High Energy Accelerator Research Organization (KEK)
9. Atomistic structure of ion tracks in ceramic compounds irradiated with swift heavy ions *	Kazuhiro Yasuda Kyushu University
10. Searching the superallowed alpha transition in the A~100 nuclei at RMS@JAEA – JAEA-RMS commissioning (2) –	Andrei Andreyev University of York
11. Decay data measurements for an LLFP nuclide ^{93}Zr	Masato Asai JAEA
12. Development of ^{211}Rn/^{211}At generator	Ichiro Nishinaka JAEA
13. Production of ^{90}Y and ^{64,67}Cu by fast neutrons for nuclear diagnostics	Kazuaki Tsukada JAEA
14. Study of delayed-neutron yields for accurate evaluation of kinetics of high-burnup reactors **	Katsuhisa Nishio JAEA

* Approved as a Common Use Program of JAEA.

** Approved as a JST Innovative Nuclear Research and Development Program entrusted to JAEA.

This is a blank page.

国際単位系（SI）

表1．SI 基本単位

基本量	SI 基本単位 名称	記号
長　　さ	メートル	m
質　　量	キログラム	kg
時　　間	秒	s
電　　流	アンペア	A
熱力学温度	ケルビン	K
物　質　量	モル	mol
光　　度	カンデラ	cd

表2．基本単位を用いて表されるSI組立単位の例

組立量	SI 組立単位 名称	記号
面　　　　　積	平方メートル	m²
体　　　　　積	立方メートル	m³
速　さ　，　速　度	メートル毎秒	m/s
加　　速　　度	メートル毎秒毎秒	m/s²
波　　　　　数	毎メートル	m⁻¹
密度，質量密度	キログラム毎立方メートル	kg/m³
面　積　密　度	キログラム毎平方メートル	kg/m²
比　　体　　積	立方メートル毎キログラム	m³/kg
電　流　密　度	アンペア毎平方メートル	A/m²
磁　界　の　強　さ	アンペア毎メートル	A/m
量濃度 (a)，濃度	モル毎立方メートル	mol/m³
質　量　濃　度	キログラム毎立方メートル	kg/m³
輝　　　　　度	カンデラ毎平方メートル	cd/m²
屈　　折　　率 (b)	（数字の）1	1
比　透　磁　率 (b)	（数字の）1	1

(a) 量濃度（amount concentration）は臨床化学の分野では物質濃度（substance concentration）ともよばれる。
(b) これらは無次元量あるいは次元1をもつ量であるが、そのことを表す単位記号である数字の1は通常は表記しない。

表3．固有の名称と記号で表されるSI組立単位

組立量	SI 組立単位 名称	記号	他のSI単位による表し方	SI基本単位による表し方
平　面　角	ラジアン (b)	rad	1 (b)	m/m
立　体　角	ステラジアン (b)	sr (c)	1 (b)	m²/m²
周　波　数	ヘルツ (d)	Hz		s⁻¹
力	ニュートン	N		m kg s⁻²
圧　力　，　応　力	パスカル	Pa	N/m²	m⁻¹ kg s⁻²
エネルギー，仕事，熱量	ジュール	J	N m	m² kg s⁻²
仕事率，工率，放射束	ワット	W	J/s	m² kg s⁻³
電　荷　，　電　気　量	クーロン	C		s A
電位差（電圧），起電力	ボルト	V	W/A	m² kg s⁻³ A⁻¹
静　電　容　量	ファラド	F	C/V	m⁻² kg⁻¹ s⁴ A²
電　気　抵　抗	オーム	Ω	V/A	m² kg s⁻³ A⁻²
コンダクタンス	ジーメンス	S	A/V	m⁻² kg⁻¹ s³ A²
磁　　　　　束	ウエーバ	Wb	Vs	m² kg s⁻² A⁻¹
磁　束　密　度	テスラ	T	Wb/m²	kg s⁻² A⁻¹
インダクタンス	ヘンリー	H	Wb/A	m² kg s⁻² A⁻²
セルシウス温度	セルシウス度 (e)	℃		K
光　　　　　束	ルーメン	lm	cd sr (c)	cd
照　　　　　度	ルクス	lx	lm/m²	m⁻² cd
放射性核種の放射能 (f)	ベクレル (d)	Bq		s⁻¹
吸収線量，比エネルギー分与，カーマ	グレイ	Gy	J/kg	m² s⁻²
線量当量，周辺線量当量，方向性線量当量，個人線量当量	シーベルト (g)	Sv	J/kg	m² s⁻²
酸　素　活　性	カタール	kat		s⁻¹ mol

(a) SI接頭語は固有の名称と記号を持つ組立単位と組み合わせても使用できる。しかし接頭語を付けた単位はもはやコヒーレントではない。
(b) ラジアンとステラジアンは数字の1に対する単位の特別な名称で、量についての情報をつたえるために使われる。実際には、使用する時には記号rad及びsrが用いられるが、習慣として組立単位としての記号である数字の1は明示されない。
(c) 測光学ではステラジアンという名称と記号srを単位の表し方の中に、そのまま維持している。
(d) ヘルツは周期現象についてのみ、ベクレルは放射性核種の統計的過程についてのみ使用される。
(e) セルシウス度はケルビンの特別な名称で、セルシウス温度を表すために使用される。セルシウス度とケルビンの単位の大きさは同一である。したがって、温度差あるいは温度間隔を表す数値はどちらの単位で表しても同じである。
(f) 放射性核種の放射能（activity referred to a radionuclide）は、しばしば誤った用語で"radioactivity"と記される。
(g) 単位シーベルト（PV,2002,70,205）についてはCIPM勧告2（CI-2002）を参照。

表4．単位の中に固有の名称と記号を含むSI組立単位の例

組立量	SI 組立単位 名称	記号	SI 基本単位による表し方
粘　　　　　　度	パスカル秒	Pa s	m⁻¹ kg s⁻¹
力のモーメント	ニュートンメートル	N m	m² kg s⁻²
表　面　張　力	ニュートン毎メートル	N/m	kg s⁻²
角　　速　　度	ラジアン毎秒	rad/s	m m⁻¹ s⁻¹=s⁻¹
角　加　速　度	ラジアン毎秒毎秒	rad/s²	m m⁻¹ s⁻²=s⁻²
熱流密度，放射照度	ワット毎平方メートル	W/m²	kg s⁻³
熱容量，エントロピー	ジュール毎ケルビン	J/K	m² kg s⁻² K⁻¹
比熱容量，比エントロピー	ジュール毎キログラム毎ケルビン	J/(kg K)	m² s⁻² K⁻¹
比　エ　ネ　ル　ギー	ジュール毎キログラム	J/kg	m² s⁻²
熱　伝　導　率	ワット毎メートル毎ケルビン	W/(m K)	m kg s⁻³ K⁻¹
体　積　エネルギー	ジュール毎立方メートル	J/m³	m⁻¹ kg s⁻²
電　界　の　強　さ	ボルト毎メートル	V/m	m kg s⁻³ A⁻¹
電　荷　密　度	クーロン毎立方メートル	C/m³	m⁻³ s A
表　面　電　荷	クーロン毎平方メートル	C/m²	m⁻² s A
電束密度，電気変位	クーロン毎平方メートル	C/m²	m⁻² s A
誘　　電　　率	ファラド毎メートル	F/m	m⁻³ kg⁻¹ s⁴ A²
透　　磁　　率	ヘンリー毎メートル	H/m	m kg s⁻² A⁻²
モルエネルギー	ジュール毎モル	J/mol	m² kg s⁻² mol⁻¹
モルエントロピー，モル熱容量	ジュール毎モル毎ケルビン	J/(mol K)	m² kg s⁻² K⁻¹ mol⁻¹
照射線量（X線及びγ線）	クーロン毎キログラム	C/kg	kg⁻¹ s A
吸　収　線　量　率	グレイ毎秒	Gy/s	m² s⁻³
放　射　強　度	ワット毎ステラジアン	W/sr	m⁴ m⁻² kg s⁻³=m² kg s⁻³
放　射　輝　度	ワット毎平方メートル毎ステラジアン	W/(m² sr)	m² m⁻² kg s⁻³=kg s⁻³
酵　素　活　性　濃　度	カタール毎立方メートル	kat/m³	m⁻³ s⁻¹ mol

表5．SI 接頭語

乗数	名称	記号	乗数	名称	記号
10²⁴	ヨ　タ	Y	10⁻¹	デ　シ	d
10²¹	ゼ　タ	Z	10⁻²	センチ	c
10¹⁸	エクサ	E	10⁻³	ミ　リ	m
10¹⁵	ペ　タ	P	10⁻⁶	マイクロ	μ
10¹²	テ　ラ	T	10⁻⁹	ナ　ノ	n
10⁹	ギ　ガ	G	10⁻¹²	ピ　コ	p
10⁶	メ　ガ	M	10⁻¹⁵	フェムト	f
10³	キ　ロ	k	10⁻¹⁸	ア　ト	a
10²	ヘクト	h	10⁻²¹	ゼプト	z
10¹	デ　カ	da	10⁻²⁴	ヨクト	y

表6．SIに属さないが、SIと併用される単位

名称	記号	SI 単位による値
分	min	1 min=60 s
時	h	1 h =60 min=3600 s
日	d	1 d=24 h=86 400 s
度	°	1°=(π/180) rad
分	'	1'=(1/60)°=(π/10 800) rad
秒	"	1"=(1/60)'=(π/648 000) rad
ヘクタール	ha	1 ha=1 hm²=10⁴m²
リットル	L, l	1 L=1 l=1 dm³=10³cm³=10⁻³m³
トン	t	1 t=10³ kg

表7．SIに属さないが、SIと併用される単位で、SI単位で表される数値が実験的に得られるもの

名称	記号	SI 単位で表される数値
電　子　ボ　ル　ト	eV	1 eV=1.602 176 53(14)×10⁻¹⁹J
ダ　ル　ト　ン	Da	1 Da=1.660 538 86(28)×10⁻²⁷kg
統一原子質量単位	u	1 u=1 Da
天　文　単　位	ua	1 ua=1.495 978 706 91(6)×10¹¹m

表8．SIに属さないが、SIと併用されるその他の単位

名称	記号	SI 単位で表される数値
バ　ー　ル	bar	1 bar=0.1MPa=100 kPa=10⁵Pa
水銀柱ミリメートル	mmHg	1 mmHg≈133.322Pa
オングストローム	Å	1 Å=0.1nm=100pm=10⁻¹⁰m
海　里	M	1 M=1852m
バ　ー　ン	b	1 b=100fm²=(10⁻¹²cm)²=10⁻²⁸m²
ノ　ッ　ト	kn	1 kn=(1852/3600)m/s
ネ　ー　パ	Np	SI単位との数値的な関係は、対数量の定義に依存。
ベ　ル	B	
デ　シ　ベ　ル	dB	

表9．固有の名称をもつCGS組立単位

名称	記号	SI 単位で表される数値
エ　ル　グ	erg	1 erg=10⁻⁷ J
ダ　イ　ン	dyn	1 dyn=10⁻⁵N
ポ　ア　ズ	P	1 P=1 dyn s cm⁻²=0.1Pa s
ストークス	St	1 St =1cm² s⁻¹=10⁻⁴m² s⁻¹
スチルブ	sb	1 sb =1cd cm⁻²=10⁴cd m⁻²
フォト	ph	1 ph=1cd sr cm⁻²=10⁴lx
ガ　ル	Gal	1 Gal =1cm s⁻²=10⁻²ms⁻²
マクスウエル	Mx	1 Mx = 1G cm²=10⁻⁸Wb
ガ　ウ　ス	G	1 G =1Mx cm⁻²=10⁻⁴T
エルステッド (a)	Oe	1 Oe ≙ (10³/4π)A m⁻¹

(a) 3元系のCGS単位系とSIでは直接比較できないため、等号「 ≙ 」は対応関係を示すものである。

表10．SIに属さないその他の単位の例

名称	記号	SI 単位で表される数値
キ　ュ　リ　ー	Ci	1 Ci=3.7×10¹⁰Bq
レ　ン　ト　ゲ　ン	R	1 R = 2.58×10⁻⁴C/kg
ラ　ド	rad	1 rad=1cGy=10⁻²Gy
レ　ム	rem	1 rem=1 cSv=10⁻²Sv
ガ　ン　マ	γ	1 γ =1 nT=10⁻⁹T
フェルミ		1 フェルミ=1 fm=10⁻¹⁵m
メートル系カラット		1 メートル系カラット = 0.2 g = 2×10⁻⁴kg
ト　ル	Torr	1 Torr = (101 325/760) Pa
標　準　大　気　圧	atm	1 atm = 101 325 Pa
カ　ロ　リ　ー	cal	1 cal=4.1858J（「15℃」カロリー），4.1868J（「IT」カロリー），4.184J（「熱化学」カロリー）
ミ　ク　ロ　ン	μ	1 μ =1μm=10⁻⁶m